

U.S. DEPARTMENT OF COMMERCE
National Technical Information Service

TECH LIBRARY KAFB, NM

0062740



LOAN COPY: RETURN
AFWL TECHNICAL LIBRARY
KIRTLAND AFB, NM

N76-21592

THREE-DIMENSIONAL FINITE ELEMENT ANALYSIS FOR
HIGH VELOCITY IMPACT

S. T. K. CHAN, ET AL

LOCKHEED MISSILES AND SPACE COMPANY, INCORPORATED
HUNTSVILLE, ALABAMA

AUGUST 1975



(NASA-CR-134933) THREE-DIMENSIONAL FINITE
ELEMENT ANALYSIS FOR HIGH VELOCITY IMPACT
Interim Report, Jun. 1974 - Jun. 1975
(Lockheed Missiles and Space Co.) 164 p

CSC 13M

N76-21592
TECH LIBRARY KAFB, NM



NASA CR 134933

LMSC-HREC TR D390900



THREE-DIMENSIONAL FINITE ELEMENT ANALYSIS FOR HIGH VELOCITY IMPACT INTERIM REPORT

by S. T. K. Chan, C. H. Lee and M. R. Brashears

**LOCKHEED MISSILES & SPACE COMPANY, INC.
HUNTSVILLE RESEARCH & ENGINEERING CENTER**

REPRODUCED BY
**NATIONAL TECHNICAL
INFORMATION SERVICE**
U. S. DEPARTMENT OF COMMERCE
SPRINGFIELD, VA. 22161

prepared for

NATIONAL AERONAUTICS AND SPACE ADMINISTRATION

**NASA Lewis Research Center
Contract NAS3-18908**

1. Report No. NASA CR 134933	2. Government Accession No.	3. Recipient's Catalog No.
4. Title and Subtitle Three-Dimensional Finite Element Analysis for High Velocity Impact	5. Report Date August 1975	6. Performing Organization Code
	7. Author(s) S. T. K. Chan, C. H. Lee, M. R. Brashears	8. Performing Organization Report No. TR D390900
9. Performing Organization Name and Address Lockheed Missiles & Space Company, Inc. Huntsville Research and Engineering Center P.O. Box 1103 Huntsville, AL 35807	10. Work Unit No.	11. Contract or Grant No. NAS3-18908
	12. Sponsoring Agency Name and Address National Aeronautics and Space Administration Washington, DC 20546	13. Type of Report and Period Covered Interim 6-74 to 6-75
15. Supplementary Notes Project Manager, C. C. Chamis Materials & Structures Division NASA-Lewis Research Center Cleveland, OH 44135		
16. Abstract <p>A finite element algorithm for solving unsteady, three-dimensional high velocity impact problems is presented. The computer program is based on the Eulerian hydroelasto-viscoplastic formulation and the utilization of the theorem of weak solutions so that the entropy condition is satisfied automatically. The equations to be solved consist of conservation of mass, momentum, and energy, equation of state, and appropriate constitutive equations. The solution technique is a time-dependent finite element analysis utilizing three-dimensional isoparametric elements, in conjunction with a generalized two-step time integration scheme. The developed code is demonstrated by solving one-dimensional as well as three-dimensional impact problems for both the inviscid hydrodynamic model and the hydroelasto-viscoplastic model.</p> <p style="text-align: center;">ORIGINAL PAGE IS OF POOR QUALITY</p> <p style="text-align: right;">PRICES SUBJECT TO CHANGE</p>		
17. Key Words (Suggested by Author(s)) Finite Element, High-Velocity-Impact, 3-D Stress Analysis, Inviscid Hydrodynamic, Hydroelasto-Viscoplastic, Isoparametric Anisotropic Material, Eulerian Description, Galerkin, Wave Propagation		18. Distribution Statement Unclassified, Unlimited
19. Security Classif. (of this report) Unclassified	20. Security Classif. (of this page) Unclassified	

* For sale by the National Technical Information Service, Springfield, Virginia 22151

FOREWORD

This interim report summarizes the efforts and accomplishments of the subject contract during the period 28 June 1974 through June 1975. The study was conducted for the NASA-Lewis Research Center, Cleveland, Ohio, by personnel in the Computational Mechanics Section, Lockheed-Huntsville Research & Engineering Center, Huntsville, Alabama. The NASA-LeRC Project Engineer is Dr. C.C. Chamis, Mail Stop 49-3.

S. T. K. Chan and C. H. Lee were the principal investigators for the study. During the early stage of this investigation, J. N. Reddy was also involved and contributed to the mechanics of high velocity impact. The study was supervised initially by M. R. Brashears and later by B. H. Shirley.

Work was begun on this contract on 28 June 1974 and all technical work is to be completed by April 1976. Efforts on this contract are being directed to the numerical solution of the three-dimensional high velocity impact problem based on the hydroelasto-viscoplastic formulation. Provisions will also be made to hook up the developed program with existing elements in the NASTRAN program through a coupling of Eulerian and Lagrangian modes.

ABSTRACT

A finite element algorithm for solving unsteady, three-dimensional high velocity impact problems is presented. The computer program is based on the Eulerian hydroelasto-viscoplastic formulation and the utilization of the theorem of weak solutions so that the entropy condition is satisfied automatically. The equations to be solved consist of conservation of mass, momentum, and energy, equation of state, and appropriate constitutive equations. The solution technique is a time-dependent finite element analysis utilizing three-dimensional isoparametric elements, in conjunction with a generalized two-step time integration scheme. The developed code is demonstrated by solving one-dimensional as well as three-dimensional impact problems for both the inviscid hydrodynamic model and the hydroelasto-viscoplastic model.

LIST OF TABLES

Table		Page
3-1	Values of the Parameters in Tillotson's Equation	3-14
3-2	Values of the Los Alamos Equation of State for Various Materials	3-15
6-1	Propagation Velocity of Pressure Waves in Target at Various Times After Impact (with 30 Linear Elements)	6-50

LIST OF FIGURES

Figure		Page
2-1	A Three-Dimensional Region at $t = 0$	2-1
2-2	A Typical Configuration to be Analyzed Using Various Descriptions	2-4
2-3	Coupling of Eulerian Mode with NASTRAN	2-6
3-1	High Velocity Impact Process	3-2
4-1	Location of Nodal Points in Three-Dimensional Elements	4-12
5-1	Target-Projectile Configuration with Target Free Surface Defined by $h(x, y, t)$	5-14
5-2	Motion of Points on Free Surface	5-14
5-3	Free Surface Passing Through a Typical Element	5-16
6-1	Finite Element Representations by Isoparametric Elements	6-5
6-2	Comparison of Predicted Temperature Distribution in a Cube	6-6
6-3	Comparison of Predicted Temperature Distribution in the Radial Direction of a Hollow Sphere	6-8

CONTENTS

Section		Page
	FOREWORD	ii
	ABSTRACT	iii
	LIST OF TABLES	vi
	LIST OF FIGURES	vi
	LIST OF SYMBOLS	xi
1	INTRODUCTION	1-1
2	VARIOUS DESCRIPTIONS AND FORMULATIONS	2-1
	2.1 Euler and Lagrange Descriptions	2-2
	2.2 Coupled Eulerian-Lagrangian Description	2-3
	2.3 Local Representation of Dynamical Systems Under an Arbitrary Frame	2-6
3	MECHANICS OF HIGH VELOCITY IMPACT	3-1
	3.1 Impact Process	3-1
	3.2 Rankine-Hugoniot Relations	3-3
	3.3 Basic Equations	3-4
	3.4 Initial and Boundary Conditions	3-17
4	BASIC FINITE ELEMENT PROCEDURES	4-1
	4.1 Governing Equations	4-1
	4.2 Finite Element Analogue by Methods of Weighted Residuals	4-4
	4.3 Isoparametric Elements and Numerical Integration	4-10
	4.4 Time Marching Schemes	4-18
5	IMPROVED FINITE ELEMENT CODE BASED ON EULERIAN DESCRIPTION	5-1

LIST OF FIGURES (Continued)

Figure		Page
6-4	Predicted Temperature History of a Typical Point ($r = 1.5$) of the Hollow Sphere with Various Time Step Sizes (Two linear elements, Crank-Nicholson in time with $\theta = 0.5$)	6-11
6-5	Predicted Temperature History at Typical Point ($r = 1.5$) of the Hollow Sphere with Various Time Step Size (two linear elements, Galerkin in Time)	6-12
6-6	Predicted Temperature History of a Typical Point ($r = 1.5$) of the Hollow Sphere with Various Number of Quadratic Elements ($\Delta t = 0.2$, Galerkin in Time)	6-13
6-7	Predicted Temperature History of a Typical Point ($r = 1.5$) of the Hollow Sphere with Various Number of Cubic Elements ($\Delta t = 0.2$, Galerkin in Time)	6-14
6-8	Predicted Temperature History at a Typical Point ($r = 1.5$) of the Hollow Sphere with Non-Zero Boundary Conditions Applied at $t = 0$ (linear elements, Galerkin in Time)	6-15
6-9	Comparison of Predicted Temperature Distribution for a Hollow Sphere Subject to Radiation Boundary Conditions	6-17
6-10	Predicted Temperature History of a Typical Point ($r = 1.5$) of the Hollow Sphere with Radiation Boundary Conditions ($\Delta t = 0.2$, Galerkin in Time)	6-18
6-11	Impact of a Cube on Semi-Infinite Target	6-21
6-12	A Typical Finite Element Mesh of the Projectile-Target Configuration.	6-22
6-13	Boundary Conditions	6-25
6-14	Variation of Pressure with Internal Energy (Aluminum $\rho_0 = 2.702 \text{ gm/cm}^3$, $p_c = 0$ to 1.5 Mb)	6-26
6-15	Variation of Pressure with Internal Energy (Aluminum $\rho_0 = 2.702 \text{ gm/cm}^3$, $p_c = 2.7$ to 7.5 Mb)	6-26
6-16	Variation of Pressure with Internal Energy (Aluminum $\rho_0 = 2.702 \text{ gm/cm}^3$, $p_c = 40.5$ to 43 Mb)	6-27

CONTENTS (Continued)

Section		Page
5	5.1 On the Theorem of Weak Solutions	5-2
	5.2 Finite Element Analogue of Weak Solutions	5-6
	5.3 Generalized Two-Step, Time Splitting Scheme	5-10
	5.4 Free Surface Considerations	5-12
	5.5 Scheme for Solving a Large System of Equations	5-17
6	TEST PROBLEMS AND NUMERICAL RESULTS	6-1
	6.1 Heat Conduction in Solids	6-1
	6.2 Impact Problems with Hydrodynamic Model	6-19
	6.3 Impact Problem with Hydroelasto-Viscoplastic Model	6-63
7	SUMMARY AND DISCUSSION	7-1
8	REFERENCES	8-1
	DISTRIBUTION LIST	

LIST OF FIGURES (Continued)

Figure		Page
6-4	Predicted Temperature History of a Typical Point ($r = 1.5$) of the Hollow Sphere with Various Time Step Sizes (Two linear elements, Crank-Nicholson in time with $\theta = 0.5$)	6-11
6-5	Predicted Temperature History at Typical Point ($r = 1.5$) of the Hollow Sphere with Various Time Step Size (two linear elements, Galerkin in Time)	6-12
6-6	Predicted Temperature History of a Typical Point ($r = 1.5$) of the Hollow Sphere with Various Number of Quadratic Elements ($\Delta t = 0.2$, Galerkin in Time)	6-13
6-7	Predicted Temperature History of a Typical Point ($r = 1.5$) of the Hollow Sphere with Various Number of Cubic Elements ($\Delta t = 0.2$, Galerkin in Time)	6-14
6-8	Predicted Temperature History at a Typical Point ($r = 1.5$) of the Hollow Sphere with Non-Zero Boundary Conditions Applied at $t = 0$ (linear elements, Galerkin in Time)	6-15
6-9	Comparison of Predicted Temperature Distribution for a Hollow Sphere Subject to Radiation Boundary Conditions	6-17
6-10	Predicted Temperature History of a Typical Point ($r = 1.5$) of the Hollow Sphere with Radiation Boundary Conditions ($\Delta t = 0.2$, Galerkin in Time)	6-18
6-11	Impact of a Cube on Semi-Infinite Target	6-21
6-12	A Typical Finite Element Mesh of the Projectile-Target Configuration.	6-22
6-13	Boundary Conditions	6-25
6-14	Variation of Pressure with Internal Energy (Aluminum $\rho_0 = 2.702 \text{ gm/cm}^3$, $\rho\epsilon = 0$ to 1.5 Mb)	6-26
6-15	Variation of Pressure with Internal Energy (Aluminum $\rho_0 = 2.702 \text{ gm/cm}^3$, $\rho\epsilon = 2.7$ to 7.5 Mb)	6-26
6-16	Variation of Pressure with Internal Energy (Aluminum $\rho_0 = 2.702 \text{ gm/cm}^3$, $\rho\epsilon = 40.5$ to 43 Mb)	6-27

LIST OF FIGURES (Continued)

Figures		Page
6-17a	Configuration of Plates at Time of Impact	6-29
6-17b	Numbering of Nodes in the Finite Element Representation (16 Linear Elements)	6-30
6-18	Time History of Pressure at Interface for 1-D Impact Problem Using Least Squares Scheme with 16 Linear Elements ($v_0 = 0.008 \text{ cm}/\mu\text{sec}$, $\rho_0 = 2.77 \text{ gm}/\text{cm}^3$)	6-31
6-19	Pressure Distributions at Various Time for 1-D Impact Problem Using Least Squares Scheme with 16 Linear Elements ($v_0 = 0.008 \text{ cm}/\mu\text{sec}$, $\rho_0 = 2.77 \text{ gm}/\text{cm}^3$)	6-33
6-20	Pressure Development at the Interface with 16 Linear Elements ($a = 0.5$, $\alpha = 0.0$)	6-34
6-21	Pressure Distributions at Various Times with 16 Linear Elements ($a = 0.5$, $\alpha = 0.0$)	6-35
6-22	Pressure Development at the Interface with 16 Linear Elements ($a = 2.0$)	6-36
6-23	Pressure Development at the Interface with 16 Linear Elements ($a = 4.0$)	6-37
6-24	Pressure Distributions at Various Times with 16 Linear Elements ($a = 2.0$)	6-38
6-25	Pressure Distributions at Various Times with 16 Linear Elements ($a = 4.0$)	6-39
6-26	Pressure Development at the Interface Using 30 Linear Elements ($a = 2.0$, $\alpha = 0.0$ and 0.25)	6-40
6-27	Pressure Development at the Interface Using 30 Linear Elements ($a = 4.0$, $\alpha = 0.0$)	6-41
6-28	Pressure Distributions at Various Times Using 30 Linear Elements ($a = 2.0$, $\alpha = 0.0$)	6-42
6-29	Pressure Distributions at Various Time Using 30 Linear Elements ($a = 4.0$, $\alpha = 0.0$)	6-43

LIST OF FIGURES (Continued)

Figures		Page
6-30	Pressure Development at the Interface Using 16 Quadratic Elements ($a = 2.0$, $\alpha = 0.0$ and 0.25)	6-45
6-31	Pressure Development at the Interface Using 16 Quadratic Elements ($a = 4.0$, $\alpha = 0.0$ and 0.25)	6-46
6-32	Pressure Distributions at Various Times Using 16 Quadratic Elements ($a = 2.0$, $\alpha = 0.0$)	6-47
6-33	Pressure Distributions at Various Times Using 16 Quadratic Elements ($a = 4.0$, $\alpha = 0.0$)	6-48
6-34	Momentum and Total Energy Distributions at $t = 20.0$ μsec (16 Linear Elements; $a = 2.0$, $\alpha = 0.0$)	6-52
6-35	Momentum and Total Energy Distributions at $t = 30.0$ μsec (16 Linear Elements; $a = 2.0$, $\alpha = 0.0$)	6-53
6-36	Momentum and Total Energy Distributions at $t = 20.0$ μsec (30 Linear Elements; $a = 2.0$, $\alpha = 0.0$)	6-54
6-37	Momentum and Total Energy Distributions at $t = 30.0$ μsec (30 Linear Elements; $a = 2.0$, $\alpha = 0.0$)	6-55
6-38	Momentum and Total Energy Distributions at $t = 20.0$ μsec (16 Quadratic Elements, $a = 2.0$, $\alpha = 0.0$)	6-56
6-39	Momentum and Total Energy Distributions at $t = 30.0$ μsec (16 Quadratic Elements; $a = 2.0$, $\alpha = 0.0$)	6-57
6-40	Momentum and Total Energy Distributions at $t = 20.0$ μsec (16 Linear Elements, $a = 4.0$, $\alpha = 0.0$)	6-58
6-41	Momentum and Total Energy Distributions at $t = 20.0$ μsec (30 Linear Elements; $a = 4.0$, $\alpha = 0.0$)	6-59
6-42	Momentum and Total Energy Distributions at $t = 20.0$ μsec (16 Quadratic Elements; $a = 4.0$, $\alpha = 0.0$)	6-60
6-43	Numbering of Nodes in the Finite Element Mesh	6-61
6-44	Pressure vs Distance into the Target ($\rho_0 = 2.702$ gm/cm ³ , $v_0 = 2.6$ cm/ μsec)	6-63
6-45	Pressure vs Time at Various Nodes on the Interface ($\rho_0 = 2.702$ gm/cm ³ , $v_0 = 2.6$ cm/ μsec , $\Delta t = 0.02$)	6-64

LIST OF FIGURES (Continued)

Figures		Page
6-46	Axial Stress and Pressure Developments at the Interface Using Galerkin's Method (16 Linear Elements)	6-66
6-47	Normal Stress Distributions at Various Times Using Galerkin's Method (16 Linear Elements)	6-67
6-48	Momentum and Total Energy Distributions Using Galerkin's Method ($t = 20.0 \mu\text{sec}$, 16 Linear Elements)	6-68
6-49	Axial Stress and Pressure Developments at the Interface (16 Linear Elements; $a = 4.0$, $\alpha = 0.0$)	6-70
6-50	Normal Stresses Distributions at $t = 10.0 \mu\text{sec}$ (16 Linear Elements; $a = 4.0$, $\alpha = 0.0$)	6-71
6-51	Normal Stresses Distributions at $t = 20.0 \mu\text{sec}$ (16 Linear Elements; $a = 4.0$, $\alpha = 0.0$)	6-72
6-52	Normal Stresses Distributions at $t = 34.2 \mu\text{sec}$ (16 Linear Elements; $a = 4.0$, $\alpha = 0.0$)	6-73
6-53	Momentum and Total Energy Distributions at $t = 20.0 \mu\text{sec}$ (16 Linear Elements; $a = 4.0$, $\alpha = 0.0$)	6-74

LIST OF SYMBOLS

a	The multiplier in multi-step time marching scheme defined in Eq. (5.15)
C_{ijkl}	Stiffness coefficients
C_s	Speed of sound
d_{ij}	Strain rate tensor
d'_{ij}	Deviatoric strain rate tensor
e	Total specific energy
E	Total energy
E_{ijkl}	Elastic constants
$F(\phi)$	Function of plastic potential
F, G, H, \dots	Arbitrary functions
h	Elevation of free surface
J	Jacobian
\dot{J}	Time rate change of J
J_2	Second invariance of stress tensor
n_j	The j th component of unit normal vector
N_j	Shape function
P	Pressure function
q	Heat transfer rate
Q	Dynamic Pressure
R	An open set in (x, t) space
S	Surface of a volume
S_{ij}	Deviatoric stress tensor

LIST OF SYMBOLS (Continued)

\hat{S}_{ij}	Deviatoric stress flux
t	Time
Δt	Time increment
T	Temperature function
T_j	The j th component of surface traction
v_j	The j th component of velocity
v_o	Impact velocity
v_p	Particle velocity
v_s	Shock velocity
V_j	The j th component of momentum
$x, y, z, \text{ or } x_j$	Cartesian Coordinates
Y	Yield stress
α	Relaxation factor in multi-step scheme
γ	Material parameters
δ	Pressure ratio in equations of state
δ_{ij}	Kronecker delta
Δ	Increment of certain quantity
ϵ	Specific internal energy
ϵ_p	Generalized plastic strain
ϕ	Primary variables in governing equations
Φ	Plastic potential
θ	Relaxation factor in Glaerkin's procedure
Θ	Divergence of velocity field
κ	Hardening (or softening) parameter

LIST OF SYMBOLS (Continued)

Λ	$= j/J$
λ	Lamé's constant
μ	Viscosity
ν	Poisson ratio
ξ, η, ζ or ξ_j	Local coordinates in finite elements
$\zeta(x, t)$	C^∞ function with compact support on a subset of (x, t) space
π	Dissipative component of pressure function
ρ	Density
σ_{ij}	Stress tensor
$\hat{\sigma}_{ij}$	Stress flux
T	An interval in time
ψ	Arbitrary function
Ψ	Plastic potential
ω_{ij}	Rigid body rotation tensor
Ω	Open subset in Euclidean space

Notations

$[A]$	Matrix A
$[A]$	Column matrix A
\underline{A}	Vector A
$\underline{\underline{A}}$	Tensor A
$[[A]]$	Jump value of function A across a shock
∂A	Boundary of a set A
\forall	Volume
\cup	Union

LIST OF SYMBOLS (Continued)

∇A	Gradient of scalar function A
∇^2	Laplacian operator
\dot{A}	Time rate of change of A

Sub- and Superscripts

i, j, k	Pertaining to the coordinate axis i,j,k
o	Pertaining to the initial value
p	Pertaining to plastic materials
s	Pertaining to the shock propagation
El	Pertaining to elastic materials
R-H	Pertaining to the Rankine-Hugoniot relation
vp	Pertaining to the viscoplastic materials
(n)	The n^{th} time step

1. INTRODUCTION

Over the last two decades considerable interest has been shown in the study of high velocity impact problems. This is primarily due to the need for the development of faster projectiles and the information concerning the meteoroid hazard to these projectiles. Current interest in high velocity impact studies is largely due to the concern over the impact of interplanetary debris on space vehicles. However, these research results have other industrial applications; for instance, in the high velocity impact of objects on turbine blades, i.e., rocks, birds or metals.

Motivated by military applications, seven symposiums were held on the subject during 1955-65 [1-7] under the sponsorship of the Army, Air Force and Navy. The bulk of the material presented at these symposiums consisted of experimental results and very little appeared on the theories explaining the high velocity impact phenomena. During the late 1960s efforts were expended toward formulating realistic theories to explain the complex dynamic and mechanical response of materials in hypervelocity impact [8-12].

The term "hypervelocity" (or high velocity) refers to the impact velocity regime in which the maximum stress developed by the primary shock wave greatly exceeds the material strengths of both the target and the projectile. During the early stages of the impact process, the target and the projectile behave essentially as compressible fluids and, consequently, several researchers [13-16] have employed pure hydrodynamic models to analyze the hypervelocity impact problems. However, these shock stresses decay very rapidly as the wave propagates away from the impact point and reach values comparable to the material yield strengths. From this point onward the material strengths become important in determining the stress and velocity fields in the target material and, consequently, due to more

involved material response to these rapidly applied stresses, the process gets more complicated. Hence, the purely hydrodynamic model cannot adequately describe the complex physical phenomena [17] and a more realistic model must be employed to account for all aspects of the high velocity impact phenomena. Several researchers have included the strength effects (e.g., see [18]) and there appeared many computer codes using more realistic hydrodynamic-elastic-viscoplastic models, [10] and [19-23]. The numerical techniques were largely based on the finite difference method, and they appear to be suited for relatively simple (and in particular to hydrodynamic) problems.

Since a hydrodynamic-elastic-viscoplastic model is basically a structural model, it would be appropriate to use structural techniques to solve the problem. Also, during the impact process, the geometry involved is generally very complicated, which would necessarily require a versatile and flexible technique in order to treat it accurately and realistically. The finite element method, which has proved to be highly successful in analyzing structural problems, is considered such a candidate. Leimbach and Prozan [24] have shown the superiority of the finite element method over the finite difference method for a simple impact problem, although their model is rather simple and unable to predict the actual dynamical response of materials in the impact region.

The general objective of the present study is to develop a three-dimensional finite element code to analyze structural components subjected to high velocity impact, using governing equations based on Eulerian and Lagrangian formulations. In particular, the impact point with its vicinity is to be represented by an Eulerian hydrodynamic-elasto-viscoplastic model, while the remaining structural components are to be analyzed with existing computer programs for structural analysis such as NASTRAN. To bridge the gap between the Eulerian mode used for the impact region and the Lagrangian mode generally employed in structural analysis, a finite element code based on coupled Eulerian and Lagrangian formulation is being developed to match the two solutions. The computer program will, at the end, be capable of handling static and dynamic response of large deformations, anisotropic material behavior, plastic yielding and material fracture.

This report contains mainly the development of a finite element computer program for the numerical solution of three-dimensional high velocity impact problems, based on the Eulerian hydroelasto-viscoplastic formulation. The equations to be solved consist of conservation of mass, momentum, and energy, equation of state, and appropriate constitutive equations. The primitive variables, i.e., density, momentum, total energy, and stresses, are used as primary unknowns in the computations. The solution technique developed in this study is a time-dependent finite element analysis utilizing three-dimensional isoparametric elements. The finite element analog of the governing equations is constructed as a consequence of the theorem of weak solutions, so that the entropy condition can be satisfied automatically in the formulation. As an integrated part of the algorithm, a generalized two-step, time-splitting finite element scheme is proposed to remedy the numerical instabilities during time marching.

Following this introduction, a description of the Eulerian, Lagrangian, and coupled Eulerian-Lagrangian formulations are presented in Section 2. The latter formulation is believed to be useful in the latter stages of development. In Section 3, the mechanics of high velocity impact are discussed and the governing equations are presented in the conservative (divergence) form, along with the specific form of the equation of state for metals. A general discussion of initial and boundary conditions is also presented. Section 4 is devoted to the finite element formulations investigated earlier, utilizing conventional methods of weighted residuals, for governing equations with Eulerian description. In addition to problem formulation, element description and numerical integrations are also discussed. Two time integration schemes, namely, the implicit finite difference and the Galerkin in time, are described at the end of this section. Presented in Section 5 is an improved finite element algorithm based on the Eulerian hydroelasto-viscoplastic formulation, using the theorem of weak solutions, together with a generalized two-step time-splitting scheme. Free surface considerations and large system equation solver are also discussed and will be integrated into the final version of

the computer code. Section 6 summarizes numerical results and findings on a number of test problems. They include the heat conduction problem in solids, impact problems computed with an inviscid hydrodynamic model, and a problem computed with the hydroelasto-viscoplastic model. Summarized in Section 7 are the findings up-to-date together with further investigations to be conducted during the remaining period.

2. VARIOUS DESCRIPTIONS AND FORMULATIONS

Consider an open (i.e., not including its boundary) bounded region Ω_0 at a time $t = 0$ in three-dimensional Euclidean space with its boundary $\partial\Omega_0$ (see Fig. 2-1). The union of Ω_0 and its boundary $\partial\Omega_0$ is the complete region (occupied by a body at time $t=0$) and is denoted by

$$\bar{\Omega}_0 = \Omega_0 \cup \partial\Omega_0$$

where \cup denotes the union of two sets. Thus, in Fig. 2-1, $\bar{\Omega}_1$ denotes the union of Ω_1 and its boundary $\partial\Omega_1$. Note that the region Ω_2 has two boundaries: one external boundary $\partial\Omega_0$ and one internal (the interface) boundary $\partial\Omega_1$.

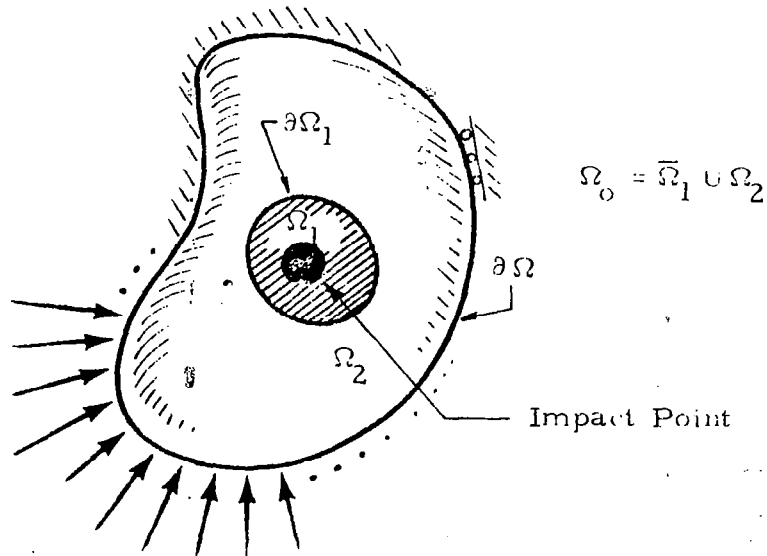


Fig. 2-1 - A Three-Dimensional Region at $t = 0$.

Suppose that we are given, at time $t = 0$, the state of the fluid (or solid) occupying the region Ω_0 , the external forces acting on the boundary, and the boundary conditions. We are then required to determine the state of the fluid and the shape of the region at a subsequent time, $t = T$. Since we plan to analyze the impact point and the surrounding region, Ω_1 , separated from the remaining region, it is convenient to consider two different fluids (or materials) occupying two different portions, Ω_1 and Ω_2 , of Ω_0 ; that is

$$\Omega_0 = \bar{\Omega}_1 \cup \Omega_2, \bar{\Omega}_1 = \Omega_1 \cup \partial\Omega_1$$

The surface $\partial\Omega_1$ is the material interface of the two regions, and it moves, as time advances, in such a manner that the pressure (or stresses) and velocity components are continuous.

2.1 EULER AND LAGRANGE DESCRIPTIONS

There are two basic descriptions well known in continuum mechanics with respect to which the governing equations can be derived and computations can be carried out. In the Lagrange description, mostly used in solid and structural problems, a coordinate system is fixed in the body or configuration Ω_0 to be studied. The deformation of the projectile-target configuration is then measured with respect to this deformed configuration. Consequently, the positions of the boundary $\partial\Omega$ and of the material interface $\partial\Omega_1$ are automatically determined. The description also permits the use of constitutive relations for the material in which the stress history of each portion of the body is taken into account. However, the Lagrange description is totally unsatisfactory for calculating a flow in which turbulence develops or in which new material interfaces develop. In this case the nodal points of the mesh will attempt to follow the motion and the material particles which were initially adjacent to each other in Ω_0 no longer remain so as the turbulence develops.

In Eulerian description, mostly used in fluid mechanic problems, the coordinate system is fixed in the space rather than in the body or configuration, and the calculations follow the material point that happens to be in a

given location at that particular time. In this case the large distortions do not cause any problems, however, more than one material cannot be treated accurately. The curves approximating $\partial\Omega$ and $\partial\Omega_1$ move with the body and therefore create irregular, time-dependent boundary zones in the fixed Eulerian mesh.

2.2 COUPLED EULERIAN-LAGRANGIAN DESCRIPTION

Obviously, neither Lagrange description nor Eulerian description alone is ideally suited for the analysis of impact problems. It is both natural and desirable to combine the use of Eulerian and Lagrangian modes depending on whether the material is in a fluid state (Eulerian mode) or solid state (Lagrangian mode). In doing so, there will be a great deal of flexibility in approximating the problem, thus enhancing the solution process regarding accuracy and computational efficiency. The idea is very similar to the well known substructuring technique, but now with different descriptions (or modes) used in various regions. More specifically, in analyzing the impact problem of structural components, the existing NASTRAN program (in Lagrangian mode) can be used to advantage for the structure part, while an Eulerian description is necessary for the impact point and its vicinity. In the following, we discuss how to couple an Eulerian mode with a Lagrangian mode, in particular, the NASTRAN program.

Conceptually, the coupling of Eulerian and Lagrangian modes can be accomplished through the use of a Coupled Eulerian-Lagrangian Code (CEL), both involving velocities, v , as unknowns [25]. Furthermore, if it is desirable to use also the NASTRAN program with displacement, u , as unknowns, another coupling of the Lagrange mode with the NASTRAN program (CLN) must also be considered. Figure 2-2 shows a configuration consisting of these different descriptions. In the figure, the dotted lines represent the interfaces between different modes. The interfaces belong to the Lagrangian mode and are to be adjusted as time advances. Therefore, the coupling of an Eulerian mode with the NASTRAN mode is to be accomplished through two steps, i.e., the CEL and CLN codes.

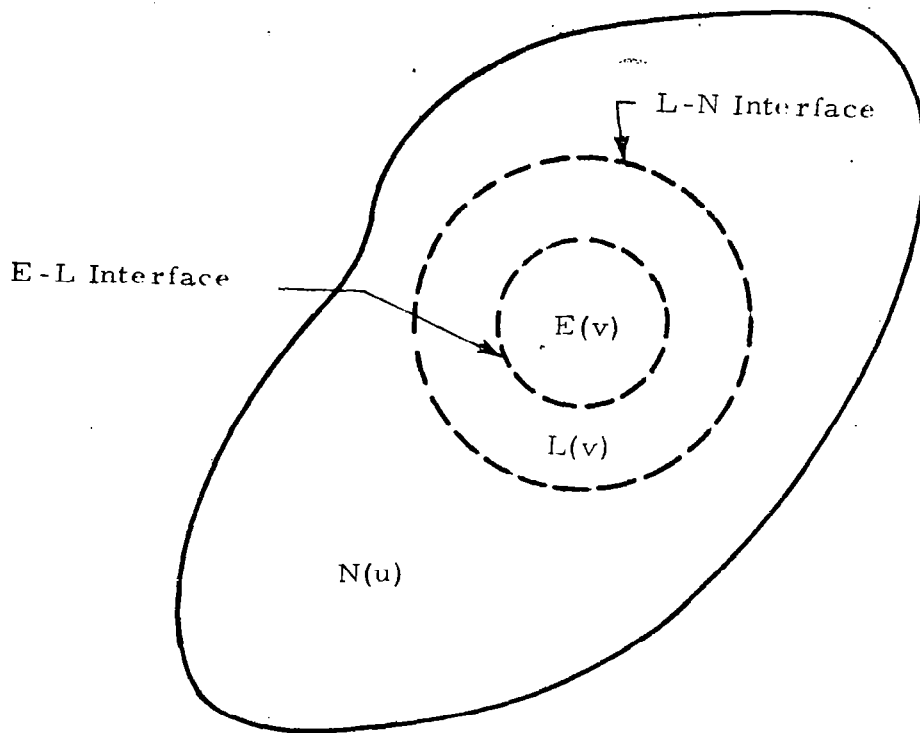


Fig. 2-2 - A Typical Configuration to be Analyzed Using Various Descriptions

The basic idea of the CEL formulation is to approximate a configuration by the combination of Eulerian and Lagrangian subregions, with the boundary and interfaces described by Lagrangian lines. The Eulerian mode will consequently have its boundary prescribed by the Lagrangian calculations. Thus the Eulerian calculation reduces to one based on a fixed mesh but having a prescribed moving boundary to reflect the coupling effects.

Consequently, the calculations that are made at each time step will involve three parts: Lagrangian calculations, Eulerian calculations, and a calculation which couples the Eulerian and Lagrangian modes by keeping track of the moving interfaces and the matching of pressure, velocities, etc., along this interface. Suppose that we know the solution of field variables (energy, density, velocities, etc.) at the n^{th} time step, t^n , and wish to compute the solution at the next time step, t^{n+1} . Since we know the position of the Lagrangian mesh, L^n , and the Eulerian mesh, E^n , with its boundary subject to move, the calculations for the next time step can proceed in the following way.

The first calculation uses the known ($t = t^n$) state of the Lagrangian region and the pressure acting on its boundary to solve the equations in Lagrangian description. The solution gives us the $t = t^{n+1}$ state in this region and also a new mesh position, L^{n+1} .

The boundary of the Eulerian region is then updated, using results from L^{n+1} , and computation is performed to seek for the t^{n+1} state of the fluid in the region E. This is considered as the Eulerian phase of the CEL calculation.

Having determined the t^{n+1} state of the Eulerian region, the second phase of coupling is to determine the pressure to act on the boundary of the Lagrange region L^{n+1} . We have thus advanced all of the field variables and grid positions to their values at the next time step, which completes one basic cycle of the CEL calculations.

Similar logic and procedures can be followed for the coupling of $L(v)$ with NASTRAN. Herein, the conversion between velocities and displacements can be done through integration in time. Another consideration is the generation or suppression of nodal unknowns on the interface, which can be accomplished using the approximating polynomials.

Another possible way is to couple the Eulerian mode with NASTRAN directly (CEN) as shown in Fig.2-3 on the following page. In this case, no formulation for

the $L(v)$ region is necessary, but the coupling must be done through the E-N interface. This is probably somewhat more complicated because the coupling involves simultaneously two kinds of descriptions in terms of different field variables. However, in light of the possible savings in computational aspect, this approach is also worth investigating.

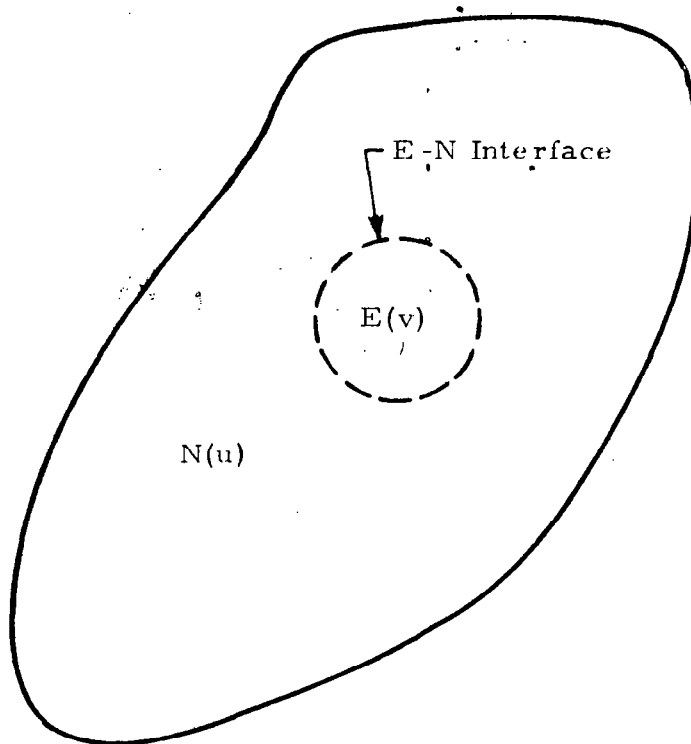


Fig. 2-3 - Coupling of Eulerian Mode with NASTRAN

2.3 LOCAL REPRESENTATION OF DYNAMICAL SYSTEMS UNDER AN ARBITRARY FRAME

In order to construct a code coupling the Eulerian-Lagrangian modes, it would be more convenient if the field equations are presented in their local

form under an arbitrary frame of reference. More specifically, let $\underline{x} = (x_1, x_2, x_3)$ be a Cartesian coordinate system moving with a certain velocity relative to the motion of the physical field, and let $\underline{X} = (X_1, X_2, X_3)$ be the reference system. Then, the two coordinate systems can be related as

$$\underline{x} = \underline{x}(\underline{X}, t) \quad (2.1)$$

When we know such a relation for every material particle in the medium, we say that the history of the motion is known at time t . We assume that the motion is continuous, single valued and that (2.1) can be inverted to give the initial position or material coordinates, \underline{X} . A necessary and sufficient condition for the inverse to exist is that the Jacobian should not vanish:

$$J = \left| \frac{\partial x_i}{\partial X_j} \right| \neq 0, \quad 0 < J < \infty \quad \forall t \geq 0 \quad (2.2)$$

Let $\underline{\Omega}$ denotes the velocity of a material element relative to the \underline{x} system, i.e.,

$$\underline{\Omega} \equiv \frac{d\underline{x}}{dt} = \underline{v} - \dot{\underline{x}} \quad (2.3)$$

where \underline{v} is the velocity of the material element, and $\dot{\underline{x}} = \partial \underline{x} / \partial t$ is the local time rate of change of the \underline{x} system. If F represents a certain physical quantity satisfying a dynamical system, then the total time derivative follows the equality

$$\frac{dF}{dt} = \frac{\partial F}{\partial t} + (\underline{\Omega} \cdot \nabla) F \quad (2.4)$$

Clearly, when $\dot{\underline{x}} = 0$, the systems \underline{x} and \underline{X} are identical, and \underline{x} represents the Eulerian system; when $\dot{\underline{x}} \equiv \underline{v}$, on the other hand, it represents the Lagrangian system.

Following the implicit differentiation rule, the divergence of the local rate of change of \underline{x} system can be related to the Jacobian as

$$\nabla \cdot \dot{\underline{x}} = \dot{J}/J \quad (2.5)$$

thus, (2.3) yields

$$\nabla \cdot \underline{\Omega} = \nabla \cdot \underline{x} - \dot{J}/J \quad (2.6)$$

Suppose now that there is a dynamic system with physical quantity F satisfying the equation

$$\frac{dF}{dt} = G(\underline{x}, t) \quad (2.7)$$

In particular, the continuity equation in \underline{x} system is readily obtained as

$$\frac{d\rho}{dt} + \rho \nabla \cdot \underline{x} = 0 \quad (2.8)$$

Then, the dynamic system (2.7) can be deduced by applying (2.3), (2.6) and (2.8) into the following form:

$$\frac{\partial (\rho F)}{\partial t} + \rho F \Lambda + \nabla \cdot (\underline{\Omega} \rho F) = \rho G \quad (2.9)$$

where

$$\Lambda = \dot{J}/J$$

It is clear that the dynamic system (2.9) would reduce to the Eulerian form when $\dot{\underline{x}} = 0$; and to the Lagrangian form when $\underline{\Omega} = 0$.

3. MECHANICS OF HIGH VELOCITY IMPACT

The high velocity impact of a projectile with a solid target results in an extremely complex phenomenon. A complete description of this problem would involve considerations of all phases in the theory of continuum mechanics. This includes not only the compressible fluid flow, dynamics of elasticity and plasticity, but also other behaviors such as melting and solidification, vaporization and condensation, and the kinetics of phase change.

Several models have been proposed for the various stages of the high velocity impact problems (see, e.g., [10], [13-16], [19-23]). Two models corresponding to different stages, namely, the inviscid hydrodynamic model and a hydroelasto-viscoplastic model, are proposed and analyzed in this study. The following discusses the mechanics of high velocity impact.

3.1 IMPACT PROCESS

The analysis of high velocity projectile mechanics can be divided into two parts: (1) dynamic behavior of the projectile and target during the penetration process, and (2) structural response of the target after the penetration process is completed.

During the short period of time in which the projectile contacts the target, a plane shock wave is generated in the projectile as well as in the target. The pressure behind these shock fronts is the largest pressure that exists throughout the entire impact process. Due to the high pressure the material strength of the target can be ignored, and the material can be assumed to behave essentially as an inviscid, compressible fluid. The shock waves generated in the projectile and target travel away from the interface (see Fig. 3-1). If the projectile is finite (in diameter), rarefaction waves will be generated and transmitted toward the axis of symmetry.

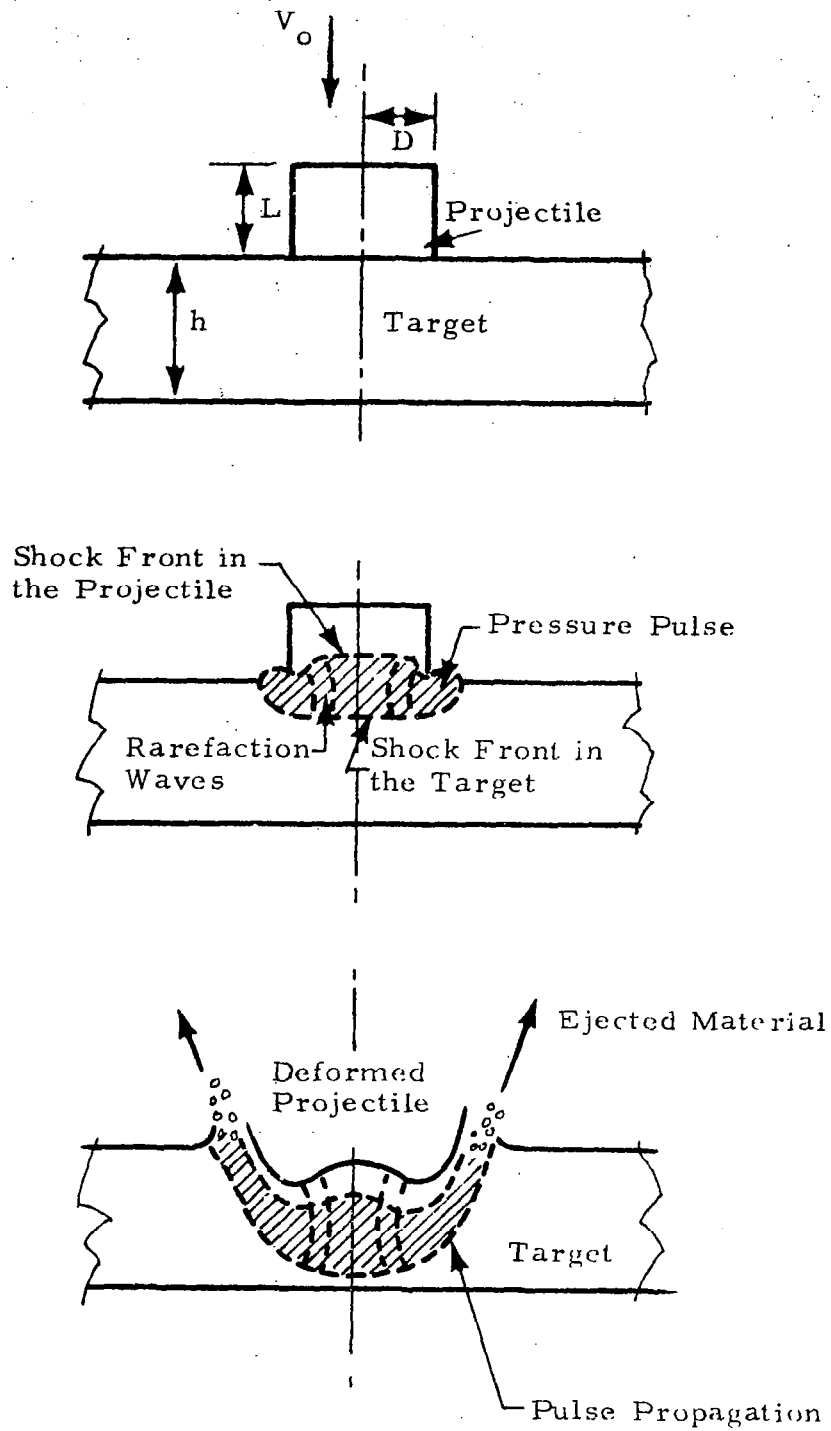


Fig. 3-1 - High Velocity Impact Process

Formulation of rarefaction waves results in the ejection of target and projectile material particles. Moreover, the rarefaction waves weaken the shock waves and change its plane shape to approximately spherical. The strength of the shock continues to decrease due to the spherical attenuation and additional rarefaction waves, and the influence of the material strength and the strain rate effects must be taken into account.

3.2 RANKINE-HUGONOT RELATIONS

As aforementioned, the material can be considered as an inviscid, compressible fluid in the short period right after the impact. The problem, including the geometric development of the impact shock, can then be treated as an unsteady, supersonic flow resembling a moving shock.

Assuming that the hemispherical shockwave profile is steady in time, the Rankine-Hugoniot relations relating the pressure, P , internal energy, ϵ , and the density, ρ , behind the shock to the same quantities in front of the shock are applied. These equations express the conservation of mass, momentum, and energy in terms of the shock velocity, v_s , and particle velocity, v_p :

$$\rho_o v_s = \rho (v_s - v_p) \quad (3.1)$$

$$P - P_o = \rho_o v_s v_p \quad (3.2)$$

$$\left[(\epsilon - \epsilon_o) - \frac{v_p^2}{2} \right] \rho_o v_s = P_o v_s \quad (3.3)$$

where the subscript o refers to the initial (or undisturbed) values. The product $\rho_o v_s$ is called the shock impedance. Using (3.1) and (3.2), (3.3) can be written as

$$\epsilon - \epsilon_o = \frac{1}{2} (P + P_o) \left(\frac{1}{\rho_o} - \frac{1}{\rho} \right) \quad (3.4)$$

Solving for v_s and v_p from (3.1) and (3.2), we obtain

$$v_s = \sqrt{\frac{1}{\rho_o} \frac{(P_o - P)}{(\rho_o/\rho - 1)}}, \quad v_p = \sqrt{\frac{1}{\rho} (P - P_o) (\rho/\rho_o - 1)} \quad (3.5)$$

The initial pressure, P_o , is generally very small and can be neglected in comparison with P . If shock velocity and particle velocity are known at a point on the shock front, the pressure can be computed using (3.2). One more relation is needed to solve the flow across a shock, namely, the equation of state; a specific form of the equation of state is given in Subsection 3.4.

3.3 BASIC EQUATIONS

As pointed out previously, an inviscid hydrodynamic model is a good approximation in the early stages of the high velocity impact when the pressures developed are much larger than the shear strength of the material. It ceases to describe the phenomenon adequately in the later stages of the impact when the influence of the shearing strength cannot be neglected. Therefore, the elastic, viscous and plastic effects of the material must be included. The equations governing the dynamic behavior of elasto-viscoplastic materials are described below.

3.3.1 Conservation Equations

The conservation of mass, momentum and energy leads to the following equations by letting $\Lambda = 0$ and $\underline{\Omega} = \underline{v}$ in Eq. (2.9):

$$\frac{\partial \rho}{\partial t} + \frac{\partial}{\partial x_i} (\rho v_i) = 0 \quad (3.6)$$

$$\frac{\partial}{\partial t} (\rho v_i) + \frac{\partial}{\partial x_j} (\rho v_j v_i) = \frac{\partial}{\partial x_j} (\sigma_{ij}) + \rho f_i \quad (3.7)$$

$$\frac{\partial}{\partial t} (\rho e) + \frac{\partial}{\partial x_j} (\rho e v_j) = \frac{\partial}{\partial x_j} (\sigma_{ij} v_i) + \rho f_i v_i + \rho \dot{S} - \frac{\partial q_i}{\partial x_i} \quad (3.8)$$

where ρ is the density, v_i is the velocity in the x_i -direction, σ_{ij} is the stress tensor, f_i is the body force per unit mass, e is the specific total energy defined as

$$e = \epsilon + \frac{1}{2} v_i v_i \quad (3.9)$$

ϵ being the internal energy per unit mass, \dot{S} is the rate of internal specific heat generation per unit mass, and q_i is the heat flux or the rate of heat flow per unit area across the surface in the direction of its unit outward normal, n_i .

3.3.2 Hydrodynamic-Elasto-Viscoplastic Constitutive Relations

When the medium under consideration is inviscid, there are no shearing stresses. The stress tensor then becomes

$$\sigma_{ij} = -P \delta_{ij} \quad (3.10)$$

where P is the hydrostatic pressure that is independent of orientation, and δ_{ij} is the Kronecker delta. In general, the stress tensor and the corresponding strain rate tensor are related to their respective deviatoric tensors by the following forms:

$$S_{ij} = \sigma_{ij} - \frac{1}{3} \sigma_{kk} \delta_{ij} \quad (3.11)$$

$$d'_{ij} = d_{ij} - \frac{1}{3} d_{kk} \delta_{ij} \quad (3.12)$$

where S_{ij} is the deviatoric stress tensor, d'_{ij} is the strain rate tensor defined by

$$d_{ij} = \frac{1}{2} \left(\frac{\partial v_i}{\partial x_j} + \frac{\partial v_j}{\partial x_i} \right) \quad (3.13)$$

and d'_{ij} is the deviatoric tensor of strain rate. The deviatoric stress tensor, S_{ij} , in turn, is related to the strain rate tensor d_{ij} through another constitutive equation. For linear elastic materials, the constitutive equation for stress and deformation rate is given by

$$S_{ij} = E_{ijkl} d_{kl} \quad (3.14)$$

where E_{ijkl} is a fourth-order tensor of material parameters. If the stress components σ_{ij} are symmetric, E_{ijkl} is also symmetric, i.e., $E_{ijkl} = E_{ijlk} = E_{jilk}$, etc. In general, there are 21 independent elastic constants. For orthotropic materials, the number of independent constants reduces to 9, and for isotropic materials it reduces to 2. The isotropic constitutive relation is given by

$$S_{ij} = 2\mu d_{ij} + \lambda d_{kk} \delta_{ij} \quad (3.15)$$

where λ and μ are the Lamé's (or viscous) constants.

Let us denote the mean of the principal components of stress by

$$Q \equiv - \frac{1}{3} \sigma_{kk} \quad (3.16)$$

The quantity Q is called the dynamic pressure. The rate of dynamic pressure dQ/dt may, in general, be decomposed into a thermodynamical reversible component dP/dt and a dissipative component $d\pi/dt$, i.e.,

$$\frac{dQ}{dt} = \frac{dP}{dt} + \frac{d\pi}{dt} \quad (3.17)$$

In general, the rate at which the local thermodynamic equilibrium is attained is much greater than the rate at which a disturbance can be propagated. It is then reasonably accurate to assume that the local thermodynamic equilibrium exists at each instant. Hence, the reversible rate of pressure, dP/dt , is not path-dependent, and its integral P follows the equation of state which can be expressed as a function of density ρ and internal energy ϵ , i.e.,

$$P = P(\rho, \epsilon) \quad (3.18)$$

The dissipative component $d\pi/dt$, on the other hand, is generally a path-dependent function related to the bulk viscosity and the rate of the change of volume. It characterizes the physical dissipative rate of dilatation. For isotropic materials,

$$\pi = -(\lambda + \frac{2}{3} \mu) d_{kk} \quad (3.19)$$

The coefficient of bulk viscosity is defined by

$$\mu' = (\lambda + \frac{2}{3} \mu) = (P - Q)/d_{kk} \quad (3.20)$$

If the volumetric changes of the materials are elastic, the changes of dynamic pressure is reversible which implies that $dQ/dt \equiv dP/dt$. Then the path-independent nature of P yields

$$Q = P = P(\rho, \epsilon) \quad (3.21)$$

Noting that for incompressible materials ($d_{kk} = 0$), Eq.(3.21) follows immediately. Equation (3.21) is also true for compressible fluids for which

$$(\lambda + \frac{2}{3} \mu) = 0 \quad (3.22)$$

Condition (3.22), known as Stoke's hypothesis, is a reasonable assumption for flow of monatomic gases; however, it is not valid for polyatomic gases or liquids, and distinction must be made between the mean stress Q and the thermodynamic pressure P .

For high velocity impact problems, the thermodynamic pressure is very high, and as aforementioned, the dynamic response in the material can thus be considered as an isentropic process. This implies that the material under high velocity impact can be assumed to possess the elastic changes in volume, and (3.21) follows.

Unfortunately, there does not exist a constitutive relation that describes all aspects (elastic, viscous and plastic) of mechanical behavior in a single expression. Constitutive relations of plasticity and viscoelasticity are essentially dynamical in nature. The constitutive relation in classical plasticity involves tensors of stress and rate of deformation, and describes rigid, perfectly plastic behavior. When elastic effects are to be considered in the analysis, this relation applies to the plastic part of the rate of deformation tensor. Similarly, the constitutive equation for viscoelastic material involves stress, elastic rate of deformation and the rate of deformation of a viscous fluid. In both cases, the elastic component of the rate of deformation tensor is usually written as a function of stress rate. Although the stress tensor is objective (axiom of objectivity requires that if a stressed continuum performs a rigid body motion and the stress field is independent of time when referred to a coordinate system attached to and moving with the material, the stress rate must vanish identically), the stress-rate tensor is not. Therefore, the stress rate $d\sigma_{ij}/dt$ should not occur in this form in the constitutive relation. An objective tensor containing the stress rate must be defined. Several objective tensors containing the stress rate can be constructed. One such tensor is due to Jaumann (see [25]) and is given by

$$\hat{\sigma}_{kl} \equiv \frac{d\sigma_{kl}}{dt} + \sigma_{km} \omega_{ml} - \sigma_{ml} \omega_{km} \quad (3.23)$$

where

$$\omega_{ij} = \frac{1}{2} \left(\frac{\partial v_i}{\partial x_j} - \frac{\partial v_j}{\partial x_i} \right) \quad (3.24)$$

The tensor $\hat{\sigma}_{kl}$ is called a stress flux. Other stress fluxes may be obtained by adding objective tensors such as $\pm \sigma_{km} d_{ml}$ to the right-hand side of (3.23):

$$\begin{aligned} \hat{\sigma}_{kl} &= \frac{d\sigma_{kl}}{dt} + \sigma_{ml} v_{m,k} + \sigma_{km} v_{m,l} \\ \hat{\sigma}_{kl} &= \frac{d\sigma_{kl}}{dt} - \sigma_{ml} v_{k,m} - \sigma_{km} v_{l,m} \\ \hat{\sigma}_{kl} &= \frac{d\sigma_{kl}}{dt} - \sigma_{ml} v_{k,m} - \sigma_{km} v_{l,m} + \sigma_{kl} v_{m,m} \end{aligned} \quad (3.25)$$

The stress flux $\hat{\sigma}_{kl}$ measures the rate of change of the stress components with respect to a rectangular Cartesian system that participates in the rotation of the material, and $\hat{\sigma}_{ij} = 0$ implies that the invariants of stress tensor are stationary.

In general, the rate of deformation tensor d_{ij} can be split into two parts, i.e.,

$$d_{ij} = d_{ij}^e + d_{ij}^{vp} \quad (3.26)$$

where d_{ij}^e is the elastic component and d_{ij}^{vp} is the viscoplastic component of the deformation rate tensor. Here it is assumed that the medium is initially unstressed. For linear elastic material, the elastic part d_{ij}^e is related to S_{ij} by Eq. (3.14), and for linear elastic-viscoplastic material $d_{ij}^{e'}$ is related to the stress flux \hat{S}_{ij} as

$$\hat{S}_{ij} = C_{ijkl} d_{kl}^{e'} \quad (3.27)$$

in the elastic region. Here the coefficient matrix C_{ijkl} depends on E_{ijkl} of Eq. (3.14). For isotropic material satisfying constitutive relation (3.15), Eq. (3.27) can be deduced further as

$$\begin{aligned} \hat{S}_{ij} &= \frac{d S_{ij}}{dt} + S_{im} \omega_{mj} - S_{mj} \omega_{im} \\ &= 2\mu d_{ij}^{e'} \end{aligned} \quad (3.28)$$

Plastic behavior is assumed to take place when a certain function of deviatoric stresses vanishes. This function is called the yield function. The yield function is constructed based on the following assumptions:

1. The yield surface is convex (or smooth).
2. The plastic component of the deformation rate tensor is normal to the yield surface at a smooth point.

If a yield condition is given by

$$\hat{F}(\sigma_{ij}, \kappa) = f(\sigma_{ij}, \kappa) - Y(\kappa) = 0 \quad (3.29)$$

with $\hat{F} < 0$ denoting the purely elastic region, then the deformation rate tensor will be a function of positive values of f . Here Y is a yield stress and κ is a history dependent hardening (or softening) parameter. We now introduce the notion of "plastic potential" $\psi(\sigma_{ij})$ defined as

$$d_{ij}^{vp} = \gamma < \phi(f/f_0) > \frac{\partial \psi}{\partial \sigma_{ij}} \quad (3.30)$$

where γ is a fluidity parameter which may depend on time, invariants of the rate of deformation, etc., and f_0 denotes a reference value of f that makes the expression non-dimensional. To ensure no viscoplastic flow below the yield limit we write

$$< \phi(f/f_0) > = \begin{cases} 0 & \hat{F} \leq 0 \\ \phi(f/f_0), & \hat{F} > 0 \end{cases} \quad (3.31)$$

A sufficiently general expression for $\phi(f/f_0)$ is given by a power law

$$\phi(f/f_0) = (f/f_0)^n \quad (3.32)$$

Various yield criteria and plastic potentials can be introduced depending on the material under study. For isotropic materials, for example, there are two well-known yield criteria: the Tresca yield criterion assumes that the yielding occurs when the greatest difference between any pair of the principal stresses σ_1 , σ_2 and σ_3 , reaches a specific value, Y . Usually, Y is taken to be the yield stress in uniaxial tension. The von Mises yield criterion for plastic yield is

$$(\sigma_1 - \sigma_2)^2 + (\sigma_2 - \sigma_3)^2 + (\sigma_3 - \sigma_1)^2 = 2 Y^2$$

or expressing in terms of σ_{ij} , we have

$$(\sigma_{11} - \sigma_{22})^2 + (\sigma_{22} - \sigma_{33})^2 + (\sigma_{33} - \sigma_{11})^2 + 6(\sigma_{12}^2 + \sigma_{13}^2 + \sigma_{23}^2) = 2 Y^2 \quad (3.33)$$

In what follows we shall take a more general yield function that is defined in terms of stress invariants as

$$f(\sigma_{ij}) = f(J_1, J_2, J_3) \quad (3.34)$$

where J_1 , J_2 and J_3 are the stress invariants,

$$J_1 = \sigma_{ii}, \quad J_2 = \frac{1}{2} S_{ij} S_{ji}, \quad J_3 = \frac{1}{3} S_{ij} S_{jk} S_{ki}$$

Clearly, von Mises yield criterion, Eq. (3.33), is a special case of Eq. (3.29), where \hat{F} is given by

$$\hat{F}(\sigma_{ij}) = \sqrt{3 J_2} - Y \equiv \hat{F}(S_{ij}) \quad (3.35)$$

where Y is the uniaxial yield stress.

For a special case in which $\psi = \hat{F}$ and Y is independent of σ_{ij} , we have from Eq. (3.30)

$$d_{ij}^{vp} = \gamma(f/f_0)^n \partial \hat{F} / \partial \sigma_{ij} = \gamma(f/f_0)^n \partial f / \partial S_{ij}$$

and for $n = 1$, and f given by Eq. (3.35), this reduces to

$$d_{ij}^{vp} = \frac{3}{2} (\gamma/f_0) S_{ij} \quad (3.36)$$

After normalizing the yield surface by the von Mises yield stress, i.e., letting $F = \hat{F}/Y$, a more general form analogous to (3.36) follows from (3.35), namely

$$d_{ij}^{vp} = \gamma \phi(F) S_{ij} / \sqrt{J_2} \quad (3.37)$$

where

$$F = \hat{F}/Y = \sqrt{\frac{S_{mn} S_{mn}}{\frac{2}{3} Y^2}} - 1$$

and the plastic potential

$$\phi(F) = \begin{cases} 0 & \text{for } F \leq 0 \\ \phi(S_{ij}) & \text{for } F > 0 \end{cases}$$

Thus, the stress flux for this case becomes upon substituting (3.37) into (3.28), while noting $d_{kk}^{vp} = 0$,

$$\hat{S}_{ij} = 2\mu(d'_{ij} - \gamma \phi(F) S_{ij} / \sqrt{J_2}) \quad (3.38)$$

Here, the material parameter γ and the plastic potential ϕ have to be found from experiments. For example, γ and $\phi(F)$ of 2024-T3 aluminum are readily obtained as

$$\phi = e^{F/\theta} - 1 \quad \text{for } \phi < \phi_0$$

$$\phi = \phi_0 + \frac{\phi_0 + 1}{\theta} (F - F_0) \quad \text{for } \phi > \phi_0$$

and $\gamma = 0.15 \sqrt{3} \text{ sec}^{-1}$, where $\phi_0 = 10^6$, $F_0 = \theta \log(\phi_0 + 1)$, and θ is a new material function which depends on the generalized plastic strain ϵ_p as

$$\begin{aligned} \theta(\epsilon_p) &= 0.0003 + 0.0214 \epsilon_p - 0.0243 \epsilon_p^2 \quad \text{for } \epsilon_p \leq 0.4 \\ &= 0.005 \quad \text{for } \epsilon_p > 0.4 \end{aligned}$$

Here, the generalized plastic strain is

$$\epsilon_p = \int_0^t \sqrt{\frac{2}{3} d_{mn}^p d_{nm}^p} dt$$

3.3.3 Equation of State

Since the governing equations contain the pressure (implicitly, in σ_{ij}), a constitutive relation must be used relating the pressure to the density and the specific internal energy. This particular constitutive relation is well known as the equation of state. For high velocity impact of solid bodies, two equations of state are well known. One of these is developed by Tillotson [27] and the other is developed by Osborne and his associates at Los Alamos Scientific Laboratory.

Tillotson's Equation of State: Tillotson's equation of state (for either compression or expansion regions) is given by

$$P = \pi(\epsilon, \rho) + A\mu + B\mu^2 \quad (3.39a)$$

for $\rho > \rho_0$ with $0 < \epsilon < \epsilon_s$, and

$$P = a\epsilon\rho + \left[\frac{b\epsilon\rho}{(1 + \epsilon/\epsilon_0\eta)^2} + A\mu e^{-\beta(1/\eta-1)} \right] e^{-\alpha(1/\eta-1)^2} \quad (3.39b)$$

for $\rho < \rho_0$ with $\epsilon > \epsilon_s$, where

$$\mu = \eta - 1, \quad \eta = \rho/\rho_0, \quad \rho_0 = \text{initial density}$$

$$\pi(\epsilon, \rho) = \epsilon\rho \left[a + \frac{b}{\epsilon/\epsilon_0\eta^2 + 1} \right]$$

and a, b, A, B and ϵ_0 are parameters (constant) which depend on the material, and ϵ_s is the sublimation energy. Values of these parameters for some materials are given in Table 3-1.

Table 3-1
VALUES OF THE PARAMETERS IN TILLOTSON'S EQUATION

Parameter	Aluminum	Iron	Copper	Lead
ρ_0 (gm/cm ³)	2.702	7.86	8.9	11.34
a	0.5	0.5	0.5	0.4
b	1.63	1.5	1.5	2.4
A (mb)	0.752	1.28	1.39	0.466
B (mb)	0.65	1.05	1.1	0.0026
α	5.0	5.0	5.0	10.0
β	5.0	5.0	5.0	2.0
ϵ_0 (mb-cm ³ /gm)	0.05	0.095	0.325	0.02
ϵ_s (mb-cm ³ /gm)	0.03	0.0244	0.0138	0.0026

Note that (3.39) is not defined for certain states, for example when $\rho < \rho_0$ with $\epsilon < \epsilon_s$, and $\rho > \rho_0$ with $\epsilon > \epsilon_s$. Some investigators have used some kind of average of the pressures given by (3.39a) and (3.39b) for these states. At this writing Tillotson's equation is not used in the calculations.

Los Alamos Equation of State: Another equation of state that is widely employed in high velocity impact calculations was derived at Los Alamos Scientific Laboratory. The equation is given by

$$P(\epsilon, \rho) = \begin{cases} [A\mu + \delta \hat{E} (B + \delta \hat{E} C)] / (\delta \hat{E} + \varphi_0), & \mu \geq 0 \\ [\mu A_1 + \delta \hat{E} (B_0 + \mu B_1 + \delta \hat{E} C)] / (\delta \hat{E} + \varphi_0), & \mu \leq 0 \end{cases} \quad (3.40)$$

where

$$\delta = \rho_0 / \rho, \quad \mu = \rho / \rho_0 - 1$$

$$A = A_1 + \mu A_2, \quad B = B_0 + \mu (B_1 + \mu B_2)$$

$$C = C_0 + \mu C_1, \quad \hat{E} = \rho \epsilon$$

and $A_1, A_2, B_0, B_1, B_2, C_0, C_1$ and ρ_0 are constants that depend on the material. Values of these parameters for plexiglas, graphite, aluminum, iron, copper and lead are given in Table 3-2.

Table 3-2
VALUES OF THE PARAMETERS IN THE LOS ALAMOS EQUATION
OF STATE FOR VARIOUS MATERIALS

Parameter	Plexiglas	Graphite	Aluminum	Iron	Copper	Lead
ρ_0	1.18	2.25	2.702	7.86	8.9	11.34
A_1	0.006199	0.1608	1.1867	7.78	4.9578	1.4844
A_2	0.015491	0.1619	0.763	31.18	3.6884	1.6765
B_0	0.14756	0.8866	3.4448	9.591	7.4727	8.7317
B_1	0.05619	0.5140	1.5451	15.676	11.519	0.96473
B_2	0.50504	1.4377	0.9643	4.634	5.5251	2.6695
C_0	0.5575	0.5398	0.43382	0.3984	0.39493	0.27732
C_1	0.6151	0.5960	0.54873	0.5306	0.52883	0.43079
φ_0	0.100	0.500	1.5	9.00	3.60	3.300

The parameters are fitted for gram-centimeter-microsecond system of units.

A comparison of the pressures computed from Tillotson's equation of state and Los Alamos equation of state is made for aluminum ($\rho_0 = 2.702 \text{ gm/cm}^3$) at $\epsilon = 0.5 \text{ mb-cm}^3/\text{gm}$ (see Fig. 3-2). The equation of state which closely agrees with the experimental data for a given material will be used.

Hugoniot Equation of State: As mentioned earlier, we need to add an equation of state to the Rankine-Hugoniot equations (3.1) through (3.3). For instance, Eq. (3.40) may be used and with the internal energy ϵ eliminated using the Rankine-Hugoniot jump relation (3.4) to obtain

$$P = \begin{cases} 2 \left[F_2(\delta) - \sqrt{F_2^2(\delta) - F_1(\delta) F_3(\delta)} \right] / F_1(\delta), & \delta \leq 1 \\ 2 \left[E_2(\delta) - \sqrt{E_2^2(\delta) - E_1(\delta) E_3(\delta)} \right] / E_1(\delta), & \delta \geq 1 \end{cases} \quad (3.41)$$

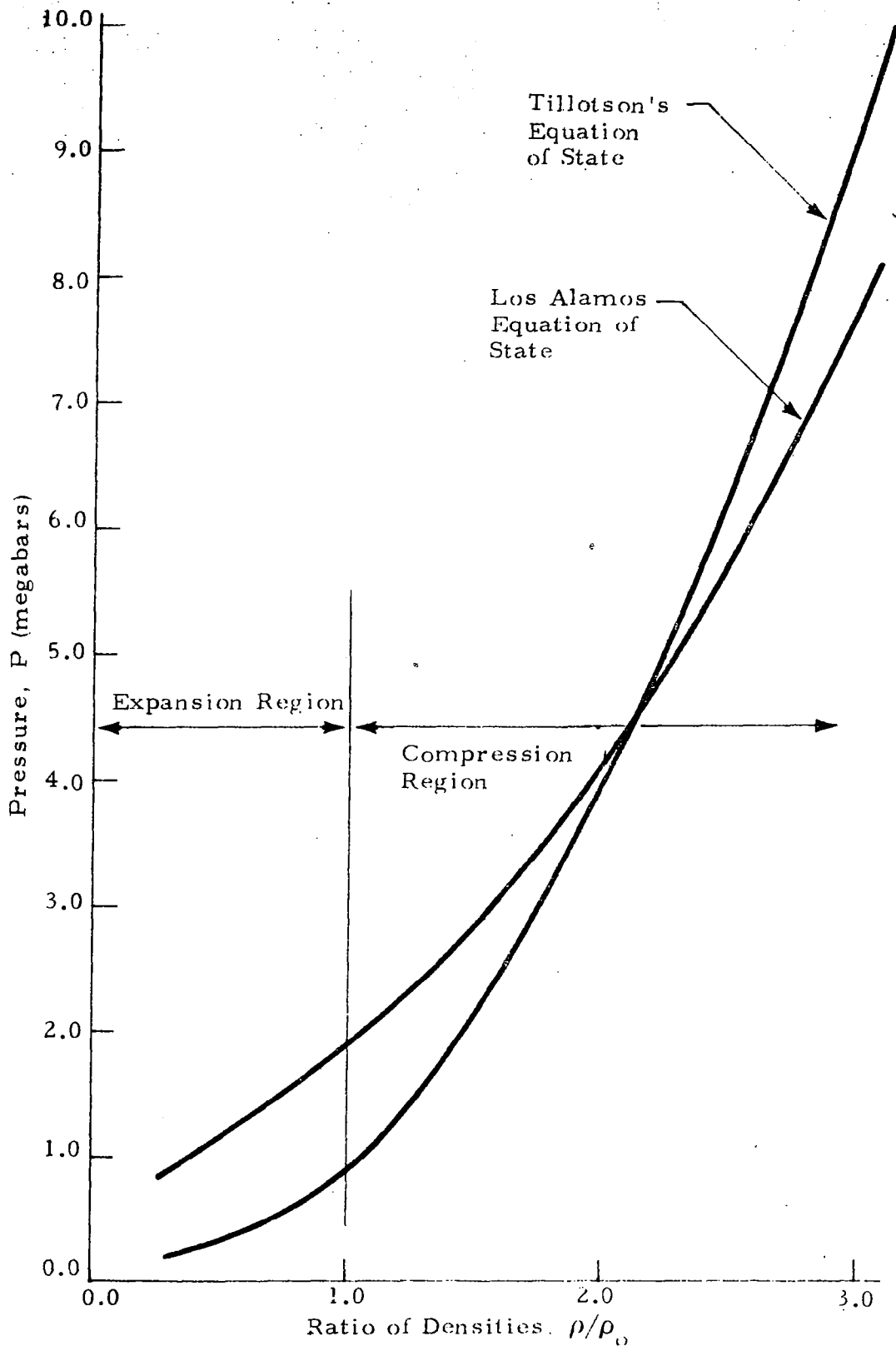


Fig. 3-2 - Variation of Pressure vs Ratio of Densities for Aluminum
($\rho_0 = 2.702$, $c = 0.5$)

where $\delta = \rho_0/\rho$, and

$$E_1(\delta) = (1 - \delta) [(1 - \delta) \{(C_0 - C_1) \delta + C_1\} - 2\delta]$$

$$E_2(\delta) = -\frac{1 - \delta}{2} [(B_0 - B_1) \delta + B_1] + \varphi_0 \delta$$

$$E_3(\delta) = A_1 (1 - \delta),$$

$$F_1 = E_1 \delta, \quad F_2 = E_2 \delta - B_2 (1 - \delta)^{3/2}$$

$$F_3 = E_3 \delta + A_2 (1 - \delta)^2$$

and the constants A_1, A_2, \dots , are the same as those appearing in (3.40).

3.4 INITIAL AND BOUNDARY CONDITIONS

To complete the description of the high velocity impact problem, we must include the initial and boundary conditions, which, in general, are time dependent.

Initial Conditions: At time $t = 0$ values of all the dependent variables $(\rho, v, \epsilon, P, S)$ must be specified at the nodal points of the mesh. It is not essential to specify all these quantities at the same set of nodal points. For instance, in the analysis of target alone, the velocities, density and specific internal energy are specified at one set of points, and pressure is specified at a different set of points.

Boundary Conditions: Depending on the type of the boundary (e.g., rigid boundary, free surface, interface, plane of symmetry, etc.), there are different kinds of boundary conditions in a problem. At a rigid boundary the normal component of the particle velocity must coincide with the normal component of the velocity of the rigid boundary. For a fixed (in time) boundary, the normal component of the particle velocity must be zero at that boundary. A plane of symmetry can be interpreted as a fixed boundary.

On a free surface, the total stress must vanish. At an interface (and at a contact discontinuity) the total stress and the normal component of particle velocity must be continuous, and the density, internal energy and the tangential component of particle velocity may be discontinuous (jumps). Across moving shock fronts the Rankine-Hugoniot relations (3.1) through (3.3) must be satisfied.

4. BASIC FINITE ELEMENT PROCEDURES

In this section, we summarize the basic finite element procedures as applied to solve the impact problem as governed by a set of hydrodynamic and constitutive equations. The formulations are based on the conventional methods of weighted residuals, i.e., the Galerkin and least squares approaches. First, the governing equations to be solved are presented. Finite element analogues for these equations are then constructed via the Galerkin and least squares approaches. In numerical aspects, the isoparametric elements together with numerical integration are described, and finally, two time-marching schemes are presented. The procedures discussed here serve as a reference for the development of an improved model described in the next section. Also, the numerical results so computed provide data for comparison purposes. These methods have been found to be quite effective for solving problems governed by elliptic and parabolic equations. However, for hyperbolic system of equations, numerical instabilities were encountered, indicating conventional methods of weighted residuals cannot be directly applied to solve the impact problem. For these reasons, an improved scheme based on the theorem of weak solution was developed, which is described in the next section.

4.1 GOVERNING EQUATIONS

With the internal heat generation and heat flux set equal to zero, the set of equations conserving mass, momentum, and energy becomes

$$\frac{\partial}{\partial t} (\rho) + \frac{\partial}{\partial x_i} (\rho v_i) = 0 \quad (4.1)$$

$$\frac{\partial}{\partial t} (\rho v_i) + \frac{\partial}{\partial x_j} (\rho v_j v_i) = \frac{\partial}{\partial x_j} (\sigma_{ij}) + \rho f_i \quad (4.2)$$

$$\frac{\partial}{\partial t} (\rho e) + \frac{\partial}{\partial x_i} (\rho v_i e) = \frac{\partial}{\partial x_i} (\sigma_{ji} v_j) + \rho f_i v_i \quad (4.3)$$

For the purpose of numerical computations, we denote

$$\rho v_i \equiv V_i, \quad \rho e \equiv E, \quad \rho f_i \equiv F_i$$

$$\Theta \equiv \frac{\partial v_k}{\partial x_k} = \frac{\partial v_1}{\partial x_1} + \frac{\partial v_2}{\partial x_2} + \frac{\partial v_3}{\partial x_3} \quad (4.4)$$

and rewrite (4.1) through (4.3) in an alternate form

$$\frac{\partial \rho}{\partial t} + v_i \frac{\partial}{\partial x_i} (\rho) + \Theta \rho = 0 \quad (4.5)$$

$$\frac{\partial}{\partial t} (V_j) + v_i \frac{\partial}{\partial x_i} (V_j) + \Theta V_j = \frac{\partial}{\partial x_i} (\sigma_{ji}) + F_j \quad (4.6)$$

$$\frac{\partial}{\partial t} (E) + v_i \frac{\partial}{\partial x_i} (E) + \Theta E = \frac{\partial}{\partial x_i} (\sigma_{ji} v_j) + F_i v_i \quad (4.7)$$

The stress tensor, σ_{ij} , can be expressed as the sum of a deviatoric stress and a dynamic pressure, namely,

$$\sigma_{ij} = S_{ij} + \frac{1}{3} \sigma_{kk} \delta_{ij} \quad (4.8)$$

For high velocity impact problems, the first invariant of stress tensor is expressed by

$$\sigma_{kk} = -3P$$

The deviatoric stress is, in turn, governed by a constitutive equation in the form

$$\frac{\partial S_{ij}}{\partial t} + v_k \frac{\partial S_{ij}}{\partial x_k} = C_{ijkl} d_{kl}^{e'} - S_{im} \omega_{mj} + S_{mj} \omega_{im} \quad (4.9a)$$

For isotropic materials satisfying von Mises criterion, the above equation reduces to

$$\frac{\partial S_{ij}}{\partial t} + v_k \frac{\partial S_{ij}}{\partial x_k} = 2\mu \left[d'_{ij} - \gamma \phi(F) \frac{S_{ij}}{\sqrt{J_2}} \right] - S_{im} \omega_{mj} + S_{mj} \omega_{im} \quad (4.9b)$$

where

$$d'_{ij} = d_{ij} - \frac{1}{3} d_{kk} \delta_{ij}$$

$$\omega_{ij} = \frac{1}{2} \left(\frac{\partial v_i}{\partial x_j} - \frac{\partial v_j}{\partial x_i} \right)$$

$$F = \sqrt{\frac{S_{mn} S_{nm}}{\frac{2}{3} Y^2}} - 1$$

$\phi(F)$ = Plastic potential with $\phi(F) = 0$ for $F \leq 0$ and

$$J_2 = \frac{1}{2} S_{mn} S_{nm}$$

To include the elastic-viscoplastic effects the constitutive equations and conservation equations must be solved simultaneously with the aid of an equation of state

$$P = P(\rho, \epsilon) \quad (4.10)$$

4.2 FINITE ELEMENT ANALOGUE BY METHODS OF WEIGHTED RESIDUALS

The finite element formulation posed herein is based on the conservation equations (4.5) through (4.7), the constitutive equations (4.9) and the Los Alamos equation of state. In principle, five conservation equations and nine constitutive equations must be solved simultaneously by the proposed finite element method. This approach, however, is not practical because it requires an extremely large storage space and possibly a large amount of computation time. Therefore, an alternative approach is introduced to solve each set of equations separately but with certain iteration procedures to couple the two systems of equations. •

In this subsection, we discuss two finite element models constructed with methods of weighted residuals, i.e., the Galerkin approach and the least squares approach. The investigations were conducted to determine whether the finite element concept with conventional methods of weighted residuals can be applied to solve the high velocity impact problem, which is governed by a system of hyperbolic equations. Also they serve the purposes of program debugging and the development of a number of subprograms which are subsequently used in an improved finite element model. The developed procedures have been applied to solve a number of heat transfer problems, and impact problems as well. The findings from these numerical computations are presented and discussed in Section 6.

4.2.1 The Galerkin Approach

Consider a nonlinear boundary value problem of the form

$$\mathcal{N}(\underline{\Lambda}) = \underline{\Gamma} \quad (4.11)$$

where \mathcal{N} is a nonlinear (differential) matrix operator, $\underline{\Lambda}$ is the column vector of unknowns, and $\underline{\Gamma}$ is a column vector of the known quantities. Writing the conservation equations in this form, we have

$$\mathcal{N}(\underline{\Lambda}) = \begin{bmatrix} \frac{\partial}{\partial t} + v_i \frac{\partial}{\partial x_i} + \Theta & 0 & 0 \\ 0 & \frac{\partial}{\partial t} + v_i \frac{\partial}{\partial x_i} + \Theta & 0 \\ 0 & 0 & \frac{\partial}{\partial t} + v_i \frac{\partial}{\partial x_i} + \Theta \end{bmatrix} \begin{Bmatrix} \rho \\ v_j \\ E \end{Bmatrix} \quad (4.12)$$

and

$$\underline{\Gamma} = \begin{Bmatrix} 0 \\ \frac{\partial}{\partial x_i} (\sigma_{ij}) + F_j \\ \frac{\partial}{\partial x_i} (\sigma_{ij} v_j) + F_i v_i \end{Bmatrix} \quad (4.13)$$

Similarly, the constitutive Eq. (4.9a) can be written in the same form as

$$\mathcal{N}(\underline{\Lambda}_{ij}) = \left[\frac{\partial}{\partial t} + v_k \frac{\partial}{\partial x_k} \right] S_{ij} \quad (4.14)$$

and

$$\Gamma_{ij} = C_{ijkl} d_{kl}^{e'} - S_{im} \omega_{jm} + S_{im} \omega_{im} \quad (4.15)$$

In the finite element/Galerkin method, approximations to ρ , V_i , E , and S_{ij} are sought in the form

$$\begin{aligned}\rho &= N_s \rho_s \\ \underline{V} &= N_s \underline{V}_s \\ E &= N_s E_s \\ \underline{\underline{S}} &= N_s \underline{\underline{S}}_s\end{aligned}, \quad s = 1, 2, \dots, n \quad (4.16)$$

wherein n is the total number of unknowns, N_s are the shape (or trail)*functions in space, ρ_s , \underline{V}_s , E_s , and $\underline{\underline{S}}_s$ are the unknown time-dependent parameters to be determined; here \underline{V} (tilda number) represents the vector $\underline{V} = \{V_i\}$, $i = 1, 2, 3$ and $\underline{\underline{S}}$ represents the deviatoric stress tensor $\underline{\underline{S}} = [S_{ij}]$, $i, j = 1, 2, 3$. (Note: The stress tensor is computed using the algebraic equation 4.8). In (4.16), we have assumed for simplicity and for computational convenience, the same type (linear, quadratic, or cubic) of approximation for all the variables.

Upon substitution and applying the Galerkin technique, we obtain for the conservation equations

$$[A_{rs}] \{ \dot{\rho}_s \} + [B_{rs}] \{ \rho_s \} = \{ 0 \} \quad (4.17)$$

$$[A_{rs}] \{ \dot{\underline{V}}_s \} + [B_{rs}] \{ \underline{V}_s \} = \{ \underline{C}_r \} \quad (4.18)$$

$$[A_{rs}] \{ \dot{E}_s \} + [B_{rs}] \{ E_s \} = \{ D_r \} \quad (4.19)$$

for $r, s = 1, 2, \dots, n$, where the superposed dot indicates partial differentiation with respect to time, t , and

$$A_{rs} = \int_V N_r N_s dV, \quad B_{rs} = \int_V \left[\Theta N_r N_s + v_i N_r \frac{\partial N_s}{\partial x_i} \right] dV$$

$$[C_r] = [C_{rj}]; \quad C_{rj} = \int_V N_r \left\{ \frac{\partial}{\partial x_i} \sigma_{ji} + F_j \right\} dV$$

and

$$D_r = \int_{\Psi} N_r \left\{ \frac{\partial}{\partial x_i} (\sigma_{ji} v_j) + F_i v_i \right\} d\Psi$$

for $i, j = 1, 2$ and 3 . The last two expressions in alternate forms can be re-written using Green's theorem,

$$C_{rj} = \oint_{S'} (N_r T_j) dS + \int_{\Psi} \left\{ - \frac{\partial N_r}{\partial x_i} \sigma_{ji} + F_j N_r \right\} d\Psi$$

$$D_r = \oint_S (N_r T_j v_j) dS + \int_{\Psi} \left(N_r F_j - \frac{\partial N_r}{\partial x_i} \sigma_{ji} \right) v_j d\Psi$$

Equations (4.17) through (4.19) are the finite element analog of the conservation equations.

The finite element analog for the deviatoric stresses can be obtained in the similar way. For instance, with Eq. (4.9b), we have

$$[A_{rs}] \{\dot{\underline{S}}_s\} + [B_{rs}] \{\underline{S}_s\} = \{\underline{Q}_r\}, \quad (4.20)$$

for $r, s = 1, 2, \dots, n$. Here

$$A_{rs} = \int_{\Psi} N_r N_s d\Psi$$

$$B_{rs} = \int_V \left[2\mu \gamma \frac{\phi(F)}{\sqrt{J_2}} N_r N_s + v_i N_r \frac{\partial N_s}{\partial x_i} \right] dV, \quad i = 1, 2, 3,$$

$$Q_{kl}^r = \int_V N_r \left\{ 2\mu d_{kl}' - S_{km} \omega_{ml} + S_{ml} \omega_{km} \right\} dV, \quad k, l, m = 1, 2, 3$$

If the viscoplastic term is retained on the right hand side, then

$$B_{rs} = \int_V v_i N_r \frac{\partial N_s}{\partial x_i} dV,$$

and

$$Q_{kl}^r = \int_V N_r \left\{ 2\mu \left[d_{kl}' - \gamma \phi(F) \frac{S_{kl}}{\sqrt{J_2}} \right] - S_{km} \omega_{ml} + S_{ml} \omega_{km} \right\} dV$$

The conservation equations and constitutive equations thus formulated will be solved iteratively. The iterative procedures start with solution at previous time step and proceed as follows:

1. Solve the conservation equations, Eqs. (4.17) through (4.19), to predict the field variables (ρ , ϵ , u , v , and w) for next time step.
2. Compute pressure using appropriate equation of state.
3. Solve the constitutive equations (4.20) to predict the deviatoric stresses for the same time step.
4. Use results obtained in Steps 2 and 3 and update the stress field.
5. The above steps are to be repeated until a prescribed convergence criterion is met. If so, proceed to next time step.

4.2.2 The Least Squares Approach

The possibility of utilizing the concept of least squares to both space and time has also been explored. To do this we write the equations to be solved in a symbolic form

$$\dot{Q} + \Lambda Q = L \quad (4.21)$$

in which Q represents the unknown function considered, L denotes the corresponding terms on the right-hand side, and Λ is defined as

$$\Lambda = \Theta + v_k \frac{\partial}{\partial x_k} \quad (4.22)$$

For a one-step scheme, the solution can be assumed in the following form

$$Q = N_i \left[(\Delta t - t) Q_i^{(n)} + t Q_i^{(n+1)} \right] / \Delta t \quad (4.23)$$

Again, N_i 's represent the space dependent shape functions, $Q_i^{(n)}$ and $Q_i^{(n+1)}$ are the unknown at nodal points for time equal to $t^{(n)}$ and $t^{(n+1)}$, respectively, with $0 \leq t \leq \Delta t$.

Upon substituting Eq. (4.23) into (4.21) with Λ_i denoting $\Lambda(N_i)$, the residual is obtained as

$$R = \frac{1}{\Delta t} \left[-N_i + (\Delta t - t) \Lambda_i \right] Q_i^{(n)} + \frac{1}{\Delta t} (N_i + t \Lambda_i) Q_i^{(n+1)} - L$$

from which the weighting function can be obtained by evaluating the partial derivatives of R with respect to each $Q_i^{(n+1)}$. Finally, the system of algebraic equations is obtained by setting

$$\iint_t \frac{\partial R}{\partial Q_i^{(n+1)}} R \, dV \, dt = 0 \quad (4.24)$$

from which a recurrence formula can be derived by carrying out the integration with respect to time explicitly.

For instance, if Λ_i and L are both assumed to be constant in the time interval and independent of the unknowns $Q_i^{(n+1)}$. Then the weighting function is

$$\frac{\partial R}{\partial Q_i^{(n+1)}} = \frac{1}{\Delta t} (N_i + t \Lambda_i)$$

The corresponding system of algebraic equations, with the time integration carried out, finally becomes

$$K_{ij} Q_j = L_i + K_{ik} Q_k^{(n)} \quad (4.25)$$

where

$$K_{ij} = \int_{\Psi} \left[N_i N_j + \frac{(\Lambda_i N_j + \Lambda_j N_i) \Delta t}{2} + \frac{(\Lambda_i \Lambda_j) \Delta t^2}{3} \right] d\Psi$$

$$L_i = \Delta t \int_{\Psi} \left(N_i + \frac{\Lambda_i \Delta t}{2} \right) \left(L - \Lambda_k Q_k^{(n)} \right) d\Psi$$

or, equivalently,

$$K_{ij} \Delta Q_j = L_i \quad (4.25a)$$

in which ΔQ_j is the increment of the unknown function at node j ,

$$\Delta Q_j = Q_j^{(n+1)} - Q_j^{(n)} \quad (2.24)$$

4.3 ISOPARAMETRIC ELEMENTS AND NUMERICAL INTEGRATION

As is seen, the use of finite elements discretizes a continuum problem and establishes a system of algebraic equations, whose coefficients are expressed in terms of the products of element shape functions. The choice of

element type in finite element analysis is usually dictated by considerations of accuracy, computational efficiency, and the specific problem under study. Clough [28] has shown that for three-dimensional finite element analysis, the "serendipity" elements with isoparametric formulation are superior to other solid elements with respect to the above considerations especially in the present problem where an adequate representation of the geometry is essential. The term "isoparametric" means that the same shape functions are used to define both the geometry and the unknown function. In the present study, use will be made of the linear, quadratic, and cubic elements of the "serendipity" family. After performing certain transformation (mapping), these brick-type elements will deform to yield curved surfaces. The following is a description of these elements.

In the "serendipity" brick element, most of the nodes are located on external edges. In fact, the linear, quadratic, and cubic elements contain no internal nodes at all. The corresponding shape functions are listed below using the notation of Zienkiewicz [29].

Let

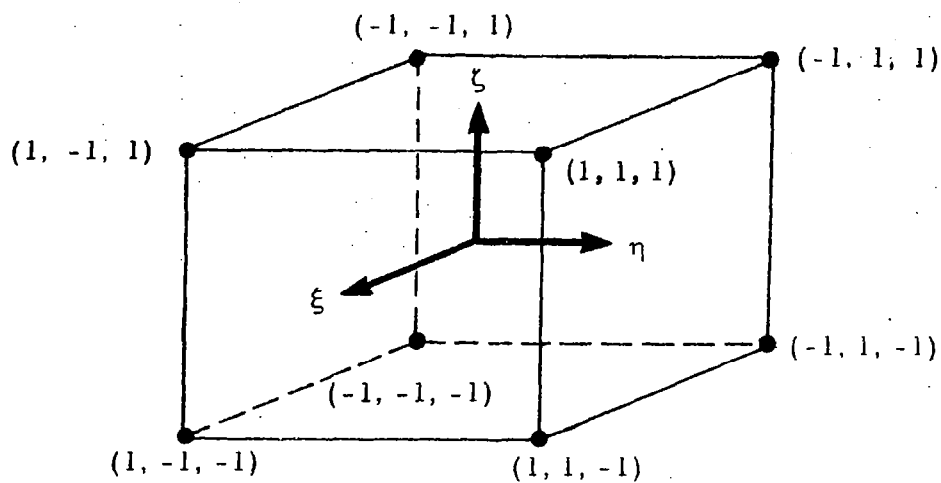
$$\xi_0 = \xi \xi_i, \eta_0 = \eta \eta_i \text{ and } \zeta_0 = \zeta \zeta_i$$

where (ξ, η, ζ) are the local coordinates and (ξ_i, η_i, ζ_i) denote the coordinates of nodal points of the cube (see Fig. 4-1).

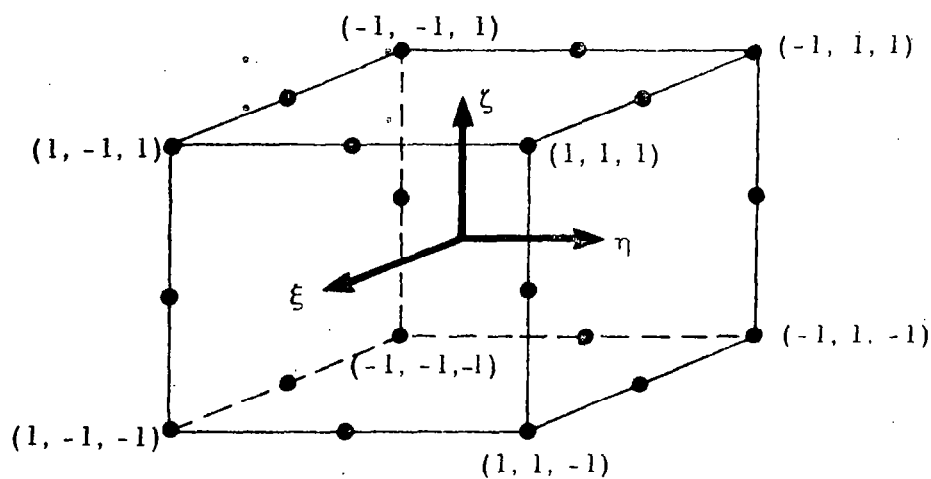
Linear Element (8 nodes)

The shape functions in this case are defined by

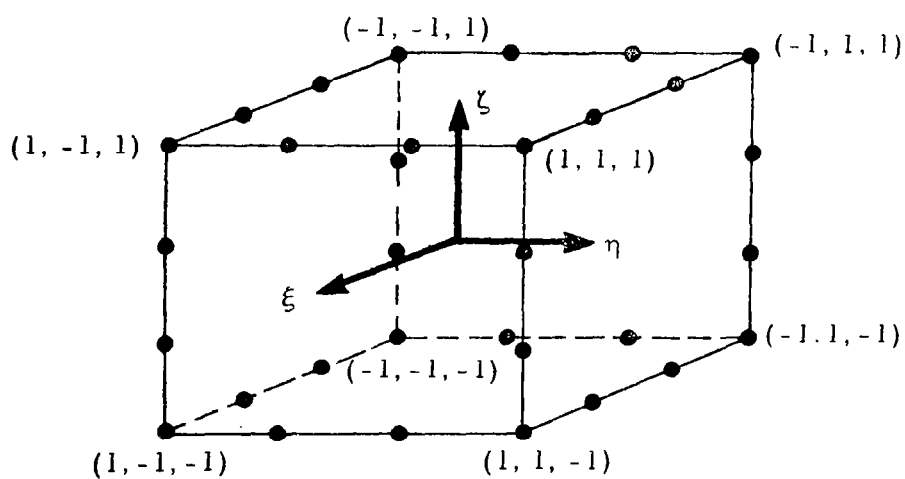
$$N_i = \frac{1}{8} (1 + \xi_0)(1 + \eta_0)(1 + \zeta_0), \quad i = 1, 2, \dots, 8$$



a. Linear Element



b. Quadratic Element



c. Cubic Element

Fig.4-1 - Location of Nodal Points in Three-Dimensional Elements

Quadratic Element (20 nodes)

For corner nodes

$$N_i = \frac{1}{8} (1 + \xi_o)(1 + \eta_o)(1 + \zeta_o)(\xi_o + \eta_o + \zeta_o - 2)$$

Typical mid-side node

$$\xi_i = 0, \eta_i = \pm 1, \zeta_i = \pm 1$$

$$N_i = \frac{1}{4} (1 - \xi^2) (1 + \eta_o) (1 + \zeta_o)$$

Cubic Element (32 nodes)

For corner nodes

$$N_i = \frac{1}{64} (1 + \xi_o)(1 + \eta_o)(1 + \zeta_o) \left[9(\xi^2 + \eta^2 + \zeta^2) - 19 \right]$$

Typical side node

$$\xi_i = \pm \frac{1}{3}, \eta_i = \pm 1, \zeta_i = \pm 1$$

$$N_i = \frac{9}{64} (1 - \xi^2)(1 + 9\xi_o)(1 + \eta_o)(1 + \zeta_o)$$

Numerical Integration

In finite element analysis, the matrices defining element properties, e.g., stiffness, etc., must be found. These will be of the form

$$I = \iiint [G(x, y, z)] dx dy dz \quad (4.26)$$

in which the expression G depends on the equation being solved and the shape functions N_i and/or their derivatives with respect to the global coordinate

system (x, y, z) . As is seen earlier, the shape functions are written in the local coordinates (ξ, η, ζ) , therefore certain transformations must be performed so that Eq. (4.26) can be evaluated in the local coordinate system.

First, the expression $G(x, y, z)$, which involves shape functions N_i and their derivatives in the global coordinate system (x, y, z) must be transformed into those in the local coordinate system (ξ, η, ζ) . When isoparametric formulation is used, the relationship between global coordinates and local coordinates is defined by

$$\begin{aligned} x &= N_i(\xi, \eta, \zeta) x_i \\ y &= N_i(\xi, \eta, \zeta) y_i \quad (\text{sum on } i) \\ z &= N_i(\xi, \eta, \zeta) z_i \end{aligned} \quad (4.27)$$

and

$$z = N_i(\xi, \eta, \zeta) z_i$$

in which N_i are the shape functions as defined before and x_i, y_i, z_i represent the global nodal coordinates. By this transformation, the originally right prism in the (ξ, η, ζ) space will become distorted in the (x, y, z) space. Now, since the shape functions are defined locally in finite element analysis, no transformation is necessary. However, the derivatives of shape functions with respect to (x, y, z) must be transformed into the local coordinate system. This can be done as follows.

Using the chain rule, one has

$$\begin{pmatrix} \frac{\partial N_i}{\partial \xi} \\ \frac{\partial N_i}{\partial \eta} \\ \frac{\partial N_i}{\partial \zeta} \end{pmatrix} = \begin{bmatrix} \frac{\partial x}{\partial \xi} & \frac{\partial y}{\partial \xi} & \frac{\partial z}{\partial \xi} \\ \frac{\partial x}{\partial \eta} & \frac{\partial y}{\partial \eta} & \frac{\partial z}{\partial \eta} \\ \frac{\partial x}{\partial \zeta} & \frac{\partial y}{\partial \zeta} & \frac{\partial z}{\partial \zeta} \end{bmatrix} \begin{pmatrix} \frac{\partial N_i}{\partial x} \\ \frac{\partial N_i}{\partial y} \\ \frac{\partial N_i}{\partial z} \end{pmatrix} = [J] \begin{pmatrix} \frac{\partial N_i}{\partial x} \\ \frac{\partial N_i}{\partial y} \\ \frac{\partial N_i}{\partial z} \end{pmatrix}$$

where $[J]$ is the Jacobian matrix. Therefore, one obtains

$$\begin{pmatrix} \frac{\partial N_i}{\partial x} \\ \frac{\partial N_i}{\partial y} \\ \frac{\partial N_i}{\partial z} \end{pmatrix} = [J]^{-1} \begin{pmatrix} \frac{\partial N_i}{\partial \xi} \\ \frac{\partial N_i}{\partial \eta} \\ \frac{\partial N_i}{\partial \zeta} \end{pmatrix}$$

The Jacobian matrix $[J]$ and its inverse, in turn, can be determined from (4.28). More explicitly, the Jacobian matrix becomes

$$[J] = \begin{bmatrix} \frac{\partial N_1}{\partial \xi} & \frac{\partial N_2}{\partial \xi} & \dots \\ \frac{\partial N_1}{\partial \eta} & \frac{\partial N_2}{\partial \eta} & \dots \\ \frac{\partial N_1}{\partial \zeta} & \frac{\partial N_2}{\partial \zeta} & \dots \end{bmatrix} \begin{pmatrix} x_1 & y_1 & z_1 \\ x_2 & y_2 & z_2 \\ \vdots & \vdots & \vdots \end{pmatrix} \quad (4.28)$$

and its inverse can be determined subsequently.

Secondly, a transformation for the volume element must also be done, that is

$$dx dy dz = \det [J] d\xi d\eta d\zeta \quad (4.29)$$

By combining (4.28) and (4.29), one finally obtains, in place of (4.26), the following integral form

$$I = \int_{-1}^1 \int_{-1}^1 \int_{-1}^1 \left[\tilde{G}(\xi, \eta, \zeta) \right] d\xi d\eta d\zeta \quad (4.30)$$

Thus the integration is carried out within the right prism and not in the complicated distorted shape.

While the limits of the integration are simple in (4.30), unfortunately the explicit form of (\tilde{G}) is not. Therefore numerical integration usually has to be resorted to. Essentially, (4.30) is approximated by the following form:

$$I = \sum_{i=1}^n \sum_{j=1}^n \sum_{m=1}^n w_i w_j w_m \left[\tilde{G}(\xi_i, \eta_j, \zeta_m) \right] \quad (4.30a)$$

In the above, w_i , w_j and w_m are the weighting coefficients with \tilde{G} evaluated at the point (ξ_i, η_j, ζ_m) . Herein, for simplicity, the number of integrating points in each direction was assumed to be the same. The numerical scheme presently used is the Gaussian quadrature, of which the points for evaluating \tilde{G} and hence the corresponding weights, are preselected to yield higher accuracy with a fixed number of integration points (see Conte, [30]). Of course, within the isoparametric family, exact numerical Gaussian quadratures can be obtained if a sufficient number of points is used.

The surface integrals can be expressed in a similar form

$$I = \iint_S [H(x, y, z)] dS \quad (4.31)$$

in which $H(x, y, z)$ is obtained from the shape functions and/or their derivatives with respect to the global coordinate system (x, y, z) and S is a curved surface in space. Since the integrand is usually very complicated, expression (4.31) will be evaluated by numerical integration.

First, the expression $H(x, y, z)$ must be expressed in terms of the local coordinates (ξ, η, ζ) , analogous to the volume integrals, and to be evaluated on the appropriate surface. Second, a transformation for the area element

must be done so that the integration is performed on the surface defined by two of the local coordinates. For instance, the area element on a surface where ξ is constant can be written as

$$dS = \det[\tilde{J}] d\xi d\eta \quad (4.32)$$

in which $[\tilde{J}]$ is the modified Jacobian matrix evaluated on the surface considered. The matrix, in turn, is defined as

$$[\tilde{J}] = \begin{bmatrix} \frac{\partial x}{\partial \xi} & \frac{\partial y}{\partial \xi} & \frac{\partial z}{\partial \xi} \\ \frac{\partial x}{\partial \eta} & \frac{\partial y}{\partial \eta} & \frac{\partial z}{\partial \eta} \\ \frac{\partial x}{\partial \xi}/\ell & \frac{\partial y}{\partial \xi}/\ell & \frac{\partial z}{\partial \xi}/\ell \end{bmatrix} \quad (4.33)$$

with

$$\ell = \sqrt{\left(\frac{\partial x}{\partial \xi}\right)^2 + \left(\frac{\partial y}{\partial \xi}\right)^2 + \left(\frac{\partial z}{\partial \xi}\right)^2}$$

The corresponding surface integral, through the above transformations, thus becomes

$$I = \int_{-1}^1 \int_{-1}^1 [\tilde{H}(\xi, \eta)] d\xi d\eta \quad (4.34)$$

Finally by using Gaussian quadrature, the surface integral is approximated by the following summation

$$I = \sum_{i=1}^n \sum_{j=1}^n w_i w_j [\tilde{H}(\xi_i, \eta_j)] \quad (4.34a)$$

in which H is evaluated at the Gaussian points (ξ_i, η_j) , w_i, w_j are the corresponding weighting coefficients, and n denotes the total number of Gaussian points to be used in each direction.

4.4 TIME MARCHING SCHEMES

As is seen previously, the Galerkin approach results in a system of ordinary differential equations with respect to time (see Eqs. (4.17) through (4.20)). These equations involve time derivatives of the primary conservative variables, ρ , V_i , E and S_{ij} , thus certain scheme must be chosen to integrate the system of equations in time to obtain the time history of the solution.

As is seen, the equations being considered are all in the same form as

$$\alpha_{ij} \dot{\phi}_j + \beta_{ij} \phi_j = \gamma_i \quad (4.35)$$

One crucial point for the success of the present study is the choice of suitable time integration scheme to solve (4.35). There are numerous schemes available; however, for the present problem, it is highly desirable to adopt some technique which is simple to apply, needs less storage locations, and should be numerically stable. We have investigated two such schemes as described in the following.

Implicit Finite Difference Scheme: In this scheme, use is made of the two consecutive time step solutions, $\phi_j^{(n)}$ and $\phi_j^{(n+1)}$, for time at $n\Delta t$ and $(n+1)\Delta t$. In particular, we assume

$$\dot{\phi}_n = \left(\phi_j^{(n+1)} - \phi_j^{(n)} \right) / \Delta t \quad (4.36)$$

and

$$\phi_j = \theta \phi_j^{(n+1)} + (1 - \theta) \phi_j^{(n)} \quad (4.37)$$

$$0 \leq \theta \leq 1$$

Upon substituting (4.36) and (4.37) into (4.35) and rearranging, we finally obtain

$$\left(\frac{\alpha_{ij}}{\Delta t} + \theta \beta_{ij} \right) \phi_j^{(n+1)} = \gamma_i + \left[\frac{\alpha_{ij}}{\Delta t} - (1 - \theta) \beta_{ij} \right] \phi_j^{(n)} \quad (4.38)$$

Equation (4.38) is simple to apply and needs only one previous time step solution. Also, it can be shown for linear problems that the scheme is unconditionally stable for $1/2 \leq \theta \leq 1$ (see [31]), thus one can avoid all stability worries and choose a value of Δt based solely on such considerations as desired accuracy. The above scheme, however, is only conditionally stable for $0 \leq \theta < 1/2$ and hence is not recommended for the problem presently studied.

Galerkin Process in Time: Alternatively, the Galerkin weighted residual process in time can also be applied to matrix equation (4.35) to obtain a recurrence relationship similar to (4.38). This approach allows a more comprehensive treatment and indeed possesses all the possible merits of the different variational processes suggested by Wilson and Nickell [32]. The recurrence could be written for several intervals simultaneously thus necessitating more equations to be solved at each step but resulting in an improved accuracy and stability, thus allowing a larger time step to be used.

Generally, within the interval we shall assume an interpolated form for each of the time dependent unknowns ϕ_j defined by its values at several time intervals

$$\phi_j = N^{(i)}(t) \phi_j^{(i)} \quad (\text{sum on } i) \quad (4.39)$$

in which $N^{(i)}(t)$ are appropriate shape functions defined continuously within the interval.

For instance, if a linear interpolation is assumed, (4.39) can be written explicitly for the time interval $(0 \leq t \leq \Delta t)$ as

$$\phi_j = \left(1 - \frac{t}{\Delta t}\right) \phi^{(n)} + \frac{t}{\Delta t} \phi^{(n+1)} \quad (4.40)$$

From the above, the time derivative can be readily obtained as

$$\dot{\phi}_j = \left(-\frac{1}{\Delta t}\right) \phi^{(n)} + \left(\frac{1}{\Delta t}\right) \phi^{(n+1)} \quad (4.41)$$

As the previous step solution $\phi^{(n)}$ is known, only one weighted residual substitution needs to be evaluated. More specifically, Eqs.(4.40) and (4.41) are first substituted into (4.35), then the resulting residual is multiplied by $t/\Delta t$, and the weighted residual is integrated over the time interval ($0 \leq t \leq \Delta t$). We obtain finally

$$\left(\frac{\alpha_{ij}}{\Delta t} + \frac{2}{3} \beta_{ij}\right) \phi_j^{(n+1)} = \frac{2}{(\Delta t)^2} \int_0^{\Delta t} \gamma_i t dt + \left(\frac{\alpha_{ij}}{\Delta t} - \frac{1}{3} \beta_{ij}\right) \phi_j^{(n)} \quad (4.42)$$

It is seen that Eqs.(4.38) and (4.42) are similar and they become identical when θ is set equal to $2/3$ and γ_i is independent of time. The two approaches, however, are based on entirely different concepts. In the finite difference scheme time is discretized and Eq.(4.35) is solved directly; on the other hand, in the Galerkin approach the nodal unknowns are assumed to be continuous functions of time and Eq.(4.35) is solved by some average process in time. The latter approach is therefore more general and can be conveniently extended to multiple time step procedures and higher order approximations in time. The schemes discussed above represent only the simplest recurrence relations available and, of course, schemes of higher order approximation can be readily incorporated if circumstances require.

5. IMPROVED FINITE ELEMENT CODE BASED ON EULERIAN DESCRIPTION

When shocks, compression waves or some other type of discontinuities occur in the material, the gradients of the dependent variables in the governing equations become very large in the neighborhoods of discontinuities. These large gradients lead the effective diffusion terms in the equations to be negative in some regions, and cause numerical instabilities in the interaction process during the numerical computations, if conventional methods described in the previous section are used. To overcome these difficulties, an alternative finite element formulation was investigated.

The present formulation consists of two primary portions. Firstly, the finite element formulation is constructed based on the theorem of weak solutions, so that the jump conditions can be satisfied automatically to take care of shock propagations. Secondly, a generalized two-step, time-splitting, shock smearing scheme has been developed and implemented. The scheme so constructed has a capability to remedy the spurious oscillations arising due to numerical instabilities.

In subsection 5.1, a general discussion on the theorem of weak solutions will be presented without proof. The governing equations in conservation form and the finite element analog of these equations, are presented in the subsequent subsection. The formulation of a two-step, time-splitting scheme is discussed in subsection 5.3. In order to predict the crater size and a numerical solution with adequate accuracy, the free surface of the projectile and target system must be treated with care. Discussion on this aspect is given in the last subsection.

5.1 ON THE THEOREM OF WEAK SOLUTIONS

The results from the theorem of weak solutions have been frequently applied in developing finite difference schemes for solving first order, non-linear hyperbolic equations. In most of these schemes, the advantages of the resulting forms deduced from the theorem are not fully utilized, since they are always in the integral form. This fact, however, can be implemented in a simple way into a finite element scheme, and the advantages can be fully utilized.

Various works on finite difference have indicated that, when the results of the theorem of weak solutions are to be used in the numerical scheme, the governing equations need to be converted into a conservation form (cf. Ritchmyer and Morton [31]). In what follows, therefore, we restrict ourselves in considering the system of hyperbolic equations in conservation form. It is obvious that all the conservation equations can be written in this form. The constitutive equations, however, are not in the conservation form but can be recast into such form as shown in subsection 5.2.

5.1.1 Theorem of Weak Solutions for First Order Quasilinear Equations

Consider a Cauchy problem of a system of quasilinear hyperbolic equations

$$\frac{\partial \phi}{\partial t} + \frac{\partial F^k}{\partial x_k} = G, \quad k = 1, 2, 3 \quad (5.1)$$

on a cylinder $R = \Omega(x) \times T(t)$, where $x = (x_1, x_2, x_3)$, $F^k = F^k(x, t, \phi)$, and $G = G(x, t, \phi)$. A class of piecewise smooth and piecewise continuous, vector valued functions ϕ in R for $t > 0$ are called the weak solutions of (5.1) if the following relation is satisfied.

$$\iint_R \zeta \left(\frac{\partial \phi}{\partial t} + \frac{\partial F^k}{\partial x_k} \right) d\Omega dt = \iint_R \zeta G d\Omega dt \quad (5.2)$$

where $\zeta \in C^\infty$ with compact support on R , i.e., ζ is any continuously differentiable function that vanishes on ∂R , the boundary of R .

Lax [33], Oleinik [34], et al., have shown that, if the following conditions are satisfied:

1. For each $k = 1, 2, 3$, F^k has a continuous partial derivative with respect to ϕ , and $\frac{\partial F^k}{\partial \phi}$ is bounded for $(x, t) \in R$;
2. For bounded ϕ , $\frac{\partial^2 F^k}{\partial \phi \partial x_k}$, $\frac{\partial^2 F^k}{\partial \phi^2}$ are continuous, and $\frac{\partial^2 F^k}{\partial \phi^2} \geq 0$;
3. The function $G(x, t, \phi)$ has a continuous partial derivative with respect to ϕ .

The generalized solution of Eq. (5.1) with a piecewise continuous initial condition is unique, and satisfies Eq. (5.2).

The proof of the theorem can be found in the aforementioned references, and will not be presented here. However, we shall discuss in what follows some immediate consequences of the theorem directly related to our proposed formulation.

5.1.2 Jump Condition

Following the Green's theorem, Eq. (5.2) can be deduced to a form

$$\iint_R \left(\phi \frac{\partial \zeta}{\partial t} + F^k \frac{\partial \zeta}{\partial x_k} \right) d\Omega \, dt$$

$$\begin{aligned}
&= \iint_R \frac{\partial}{\partial t} [\zeta(x, t) \phi(x, t)] d\Omega dt + \iint_{\partial\Omega \times T} \zeta F^k n_k dS dt \\
&- \iint_R \zeta G d\Omega dt
\end{aligned} \tag{5.3}$$

where n_k is the k^{th} component of the outward unit normal vector on ∂ , the boundary of Ω .

Observe now the integrals

$$I_v = \iint_R \frac{\partial}{\partial t} [\zeta(x, t) \phi(x, t)] d\Omega dt \tag{5.4}$$

for some $t_1 \in T$, $x \in \bar{\Omega}$; and

$$I_s = \iint_{\partial\Omega \times T} \zeta(x, t) F^k(x, t) n_k dS dt \tag{5.5}$$

for all $x \in \partial\Omega$, and $t \in T$. Since $\zeta(x, t)$ is piecewise continuous function with compact support in R , it is obvious that $I_s \equiv 0$ if there is no discontinuity in R . Otherwise, we may deduce without difficulty the jump of the function F^k across the discontinuity, i.e.,

$$I_s = \iint_{\partial\Omega_s \times T} \zeta [F^k] n_k dS dt \tag{5.6}$$

where $\partial\Omega_s$ is the surface of the shock layer, $[F^k]$ denotes the jump of F^k , the k^{th} component of F , across the shock.

For the integral I_V , if there is no discontinuity on \bar{R} , Eq. (5.4) can be reduced to

$$I_V = \int_{\Omega} \zeta(x, t) \phi(x, t) d\Omega - \int_{\Omega} \zeta(x, 0) \phi(x, 0) d\Omega$$

Across a shock, however, the Leibnitz's rule yields

$$\begin{aligned} I_V = & \int_{\Omega} \zeta(x, t) \phi(x, t) d\Omega - \int_{\Omega} \zeta(x, 0) \phi(x, 0) d\Omega \\ & + \int_T \zeta(x_1, \xi) \phi(x_1, \xi) \int_{\partial\Omega_s(t)} c_s(\eta, \xi) dS(\eta) d\xi \\ & - \int_T \zeta(x_2, \xi) \phi(x_2, \xi) \int_{\partial\Omega_s(t)} c_s(\eta, \xi) dS(\eta) d\xi \end{aligned}$$

where the subscripts 1, 2 denote the values at the upstream and downstream of the shock, respectively. Here, the speed of sound is defined as

$$C_s = \left| \frac{\partial S^k}{\partial t} n_k \right|$$

The last two terms in the above integral is no more than the jump of ϕ , i.e.,

$$I_V = \int_{\Omega} \zeta(x, t) \phi(x, t) d\Omega - \int_{\Omega} \zeta(x, 0) \phi(x, 0) d\Omega$$

$$+ \int_{\partial\Omega_s \times T} \zeta(x, t) c_s(x, t) [[\phi]] dS dt \quad (5.7)$$

Since the entropy condition requires that

$$c_s [[\phi]] - [[F^k]] n_k = 0 \quad (5.8)$$

The substitution of (5.6) and (5.7) into (5.3) then yields

$$\begin{aligned} & \iint_R \left(\phi \frac{\partial \zeta}{\partial t} + F^k \frac{\partial \zeta}{\partial x_k} \right) d\Omega dt \\ &= - \int_{\Omega} \zeta(x, 0) \phi(x, 0) d\Omega - \iint_R \zeta G d\Omega dt \end{aligned} \quad (5.9)$$

This consequence implies that (5.9) satisfies the jump condition (5.8) automatically.

5.2 FINITE ELEMENT ANALOGUE OF WEAK SOLUTIONS

Recall that we are considering a system of equations

$$\frac{\partial \phi}{\partial t} + \frac{\partial F^k}{\partial x_k} = G \quad (5.1)$$

where $F^k = F^k(x, t, \phi)$, $k = 1, 2, 3$ and $G = G(x, t, \phi)$. In this section, we shall formulate the finite element analog of equations in the form of (5.1). To do this, we have to write the conservation equations and the constitutive equations for impact problems in the above form.

5.2.1 Governing Equations in Conservation Form

It is obvious that the conservation equations (4.1) through (4.3) are in the conservation form. The constitutive equations (4.9), however, are not in the form of (5.1). Therefore, we recast the constitutive equations as

$$\frac{\partial S_{ij}}{\partial t} + \frac{\partial (v_k S_{ij})}{\partial x_k} = \Theta S_{ij} + 2\mu \left(d_{ij} - \gamma \Phi \frac{S_{ij}}{\sqrt{J_2}} \right) - S_{im} \omega_{mj} + S_{mj} \omega_{im}$$

where $\Theta = \text{div } \gamma$. Here, an additional term ΘS_{ij} appears on the right-hand side, which is considered as the forcing term.

Thus, for high velocity impact problems, the governing equations can be written in the conservation form (5.1) with

$$\phi = \begin{Bmatrix} \rho \\ V_j; j = 1, 2, 3 \\ E \\ S_{ij}; i, j = 1, 2, 3 \end{Bmatrix}$$

$$F^k = \begin{Bmatrix} v_k \rho \\ v_k V_j - \sigma_{jk}; j = 1, 2, 3 \\ v_k E - \sigma_{lk} V_l \\ v_k S_{ij}; i, j = 1, 2, 3 \end{Bmatrix}; k, l = 1, 2, 3$$

$$G = \left\{ \begin{array}{l} 0 \\ F_j; j=1,2,3 \\ F_j v_j; j=1,2,3 \\ [(\Theta - 2\mu\gamma\phi / \sqrt{J_2}) S_{ij} + 2\mu d_{ij} \\ - S_{im} \omega_{mj} + S_{mj} \omega_{im}]; i,j,m=1,2,3 \end{array} \right\} \quad (5.10)$$

5.2.2 Finite Element Formulation

Suppose that the discrete approximation is constructed by appropriate interpolation functions in each element, and take $\zeta(x, t)$ defined in (5.9) to be the weighting function with compact support in the cylinder $\Delta R = \Omega_e \times T$. Here, Ω_e is the volume of an element e , $T = [0, \Delta t]$ and Δt is the time step in the time-split scheme. In order to utilize integral relation (5.9) to minimize the error, we have to approximate the (weighting) function ζ by the shape function at the previous time step, i.e.,

$$\zeta_r = (1 - \frac{t}{\Delta t}) N_r, \quad r = 1, 2, \dots, m \quad (5.11)$$

where m is the number of nodes in the element e . Also, approximate the solution to (5.1) as

$$\phi = N_s \left[(1 - \frac{t}{\Delta t}) \phi_s^{(n)} + \frac{t}{\Delta t} \phi_s^{(n+1)} \right], \quad s = 1, \dots, m \quad (5.12)$$

With these expressions, we obtain a matrix equation in the form of

$$\left([A_{rs}] - \frac{\Delta t}{3} [B_{rs}] \right) \left\{ \phi_s^{(n+1)} \right\} = \left([A_{rs}] + \frac{2\Delta t}{3} [B_{rs}] \right) \left\{ \phi_s^{(n)} \right\} + \Delta t \left\{ C_r \right\} \quad (5.13)$$

where

$$\begin{aligned} A_{rs} &= \int_{\Psi} N_r N_s d\Psi \\ B_{rs} &= \int_{\Psi} v_k \frac{\partial N_r}{\partial x_k} N_s d\Psi \\ C_r &= \int_{\Psi} \left[H^k \frac{\partial N_r}{\partial x_k} + N_r G \right] d\Psi \end{aligned} \quad (5.14)$$

Here, the vector $\underline{H} = \underline{F} - \phi \underline{v}$.

5.2.3 Remarks

Instead of using Eq. (5.11), we may as well as approximate the weighting function by $\zeta_r = \frac{t}{\Delta t} N_r$, $r = 1, 2, \dots, m$. In this case, however, the integral formula (5.3) instead of (5.9) has to be used. Mathematically, these two formulations could achieve the same accuracy and possess a similar stability character. Nevertheless, the surface integrals appearing in (5.3) would affect the numerical computations, as will be shown in the numerical experiments.

This argument also explains the difficulties encountered in the conventional Galerkin method. It is essential that, after integration by parts, the Galerkin's formulation as shown in (4.42) is similar to the matrix equation (5.13). The only difference between (4.42) and (5.13) is their relaxation factors, i.e., a coefficient $2/3$ in (4.42) is replaced in (5.13) by a factor $-1/3$. However, the forcing vector $\left\{ C_r \right\}$ in (4.42) contains surface integrals as in the aforementioned case when $\zeta_r = \frac{t}{\Delta t} N_r$ and (5.3) are used. Moreover, matrix

equation (4.42) does not satisfy the jump conditions. Therefore, the conventional Galerkin formulation is considered less significant for solving hyperbolic equations.

It is important to note that, however, neither the use of $\xi_r = \frac{t}{\Delta t} N_r$ nor $\xi_r = \left(1 - \frac{t}{\Delta t}\right) N_r$ can always represent accurately the class of test functions having compact support on R if the conventional shape functions are used. These known classes of shape functions may not vanish or equal to a same constant on all boundaries of the cylinder R , although we have presumed that they do as required by the theorem of weak solutions. The error arises from this aspect, nevertheless, can be reduced easily by treating the boundary conditions with care during the numerical computations. Meanwhile, constructing a new class of shape functions does not seem to be practical due to the difficulties involved.

5.3 GENERALIZED TWO-STEP, TIME-SPLITTING SCHEME

It is well known that the finite element method with conventional assembly techniques is equivalent to the centered finite difference scheme. When the method is applied to solve flow problems containing shock waves, numerical instabilities generally arise primarily due to the lack of dissipative terms. In the finite difference approach, this difficulty can be overcome by either one, or a combination of the following schemes:

- Introducing artificial viscosity,
- Replacing the center difference by a noncogenic difference scheme,
- Utilizing the two-step finite-difference scheme, or
- Introducing Lax-Wendroff's second order correction, etc.

All of the above variations except the second have been adopted in the current finite element codes to solve the impact problem. It is found that the last two

approaches yielded promising results. However, due to the excessive computation time needed with the Lax-Wendroff second order scheme, we have decided to adopt the two-step, time-splitting procedure.

Consider a non-linear matrix equation

$$([A_{rs}] - \Delta t \theta [B_{rs}]) \{\phi_s^{(n+1)}\} = ([A_{rs}] + \Delta t (1 - \theta) [B_{rs}]) \{\phi_s^{(n)}\} + \Delta t \{C_r\} \quad (5.14)$$

where $[A_{rs}]$, $[B_{rs}]$ are square matrices, $\{C_r\}$ is a column matrix, and $\phi^{(n)}$ denotes the solution of ϕ at the n^{th} time step. In the present case, the factor $\theta = 1/3$, the matrices

$$A_{rs} = \int_{\Omega} N_r N_s d\Omega,$$

$$r, s = 1, 2, \dots, l$$

$$B_{rs} = \int_{\Omega} \frac{\partial N_r}{\partial x_k} N_s v_k d\Omega$$

and the vector

$$C_r = \int_{\Omega} \left\{ \frac{\partial N_r}{\partial x_k} H^k + N_r G \right\} d\Omega$$

where $H^k = F^k - v_k \phi$.

Following the general approach of two-step procedure (see Richtmyer and Morton [31]), the solution of (5.14) can be solved by the following steps:

$$([A_{rs}] - a \Delta t \theta [B_{rs}^{(n)}]) \{\phi_s^{(n+a)}\} = ([A_{rs}] + a \Delta t (1 - \theta) [B_{rs}^{(n)}]) \{\phi_s^{(n)}\} + a \Delta t \{C_r^{(n)}\} \quad (5.15)$$

$$\left([A_{rs}] - \Delta t \theta [\tilde{B}_{rs}^{(n+1)}] \right) \left\{ \phi_s^{(n+1)} \right\} = \left([A_{rs}] + \Delta t (1 - \theta) [\tilde{B}_{rs}^{(n+1)}] \right) \left\{ \phi_s^{(n)} \right\} + \Delta t \left\{ \tilde{C}_r^{(n+1)} \right\} \quad (5.16)$$

where

$$\tilde{B}_{rs}^{(n+1)} = \alpha B_{rs}^{(n)} + (1 - \alpha) \bar{B}_{rs}^{(n+a)}$$

$$\tilde{C}_r^{(n+1)} = \alpha C_r^{(n)} + (1 - \alpha) \bar{C}_r^{(n+a)}$$

Here α is a relaxation factor, and the constant a may be an integer or a fraction multiplier of the time step. As will be seen in Section 6, the numerical computations become more stable as the parameter a increases. The mathematical aspect of the present formulation is yet to be studied in depth. In particular, the relation between α and the ratio of the time step size and the element size must be determined in order to obtain an optimal accuracy for the general impact problems.

5.4 FREE SURFACE CONSIDERATIONS

In order to predict the crater size and produce a numerical solution with adequate accuracy, the free surface of the projectile and target system must be treated with care. Essentially, a free surface has zero pressure, but with its geometric shape changing with time. In the present formulation, the imposition of zero pressure on the free surface could be carried out conveniently by proper consideration of the boundary integrals in the resulting algebraic equations; however, the adjustment of the free surface location is somewhat more complicated. There are several ways of handling the free surface problem. In this subsection, two approaches which are believed to be suitable for the present technique will be discussed. One of the approaches is to consider the equation governing the free surface motion as a part of the governing equations. The other one is simply to compute the solution on the free surface by an extrapolation procedure.

5.4.1 Method Accommodating the Free Surface Equation

Consider the free surface in Fig. 5-1, which separates the interior of the target from the void region, and let $h(x, y, t)$ be the vertical distance from the x - y plane to the free surface. An equation governing the free surface movement can be derived as follows.

In Fig. 5-2, let A and B be two adjacent points on the free surface at time, t , with vertical distance defined by $h(x, y, t)$ and $h(x + u\Delta t, y + v\Delta t, t)$ respectively. After Δt , point A moves to point A' whose vertical distance is $h(x + u\Delta t, y + v\Delta t, t + \Delta t)$. From the figure, we have

$$\begin{aligned}\Delta h &= h(x + u\Delta t, y + v\Delta t, t + \Delta t) - h(x + u\Delta t, y + v\Delta t, t) \\ &= h(x + u\Delta t, y + v\Delta t, t + \Delta t) - h(x, y, t) + h(x, y, t) - h(x + u\Delta t, y + v\Delta t, t) \\ &= w\Delta t - h(x + u\Delta t, y + v\Delta t, t) + h(x, y, t)\end{aligned}$$

Dividing through by Δt and letting $\Delta t \rightarrow 0$, we have

$$\frac{\partial h}{\partial t} = w - u \frac{\partial h}{\partial x} - v \frac{\partial h}{\partial y} \quad (5.17)$$

or equivalently, with first order approximation

$$\Delta h = (w - u \frac{\partial h}{\partial x} - v \frac{\partial h}{\partial y}) \Delta t \quad (5.18)$$

As mentioned above, to analyze the free surface motion, we consider Eq. (5.17) as a part of the governing equations, and is computed successively with the conservation equations, the constitutive equations, and the equation of state. Equation (5.17) must be solved to find h , or equivalently Δh , at each node. Here we confine our attention only to the vertical movement of the free surface.

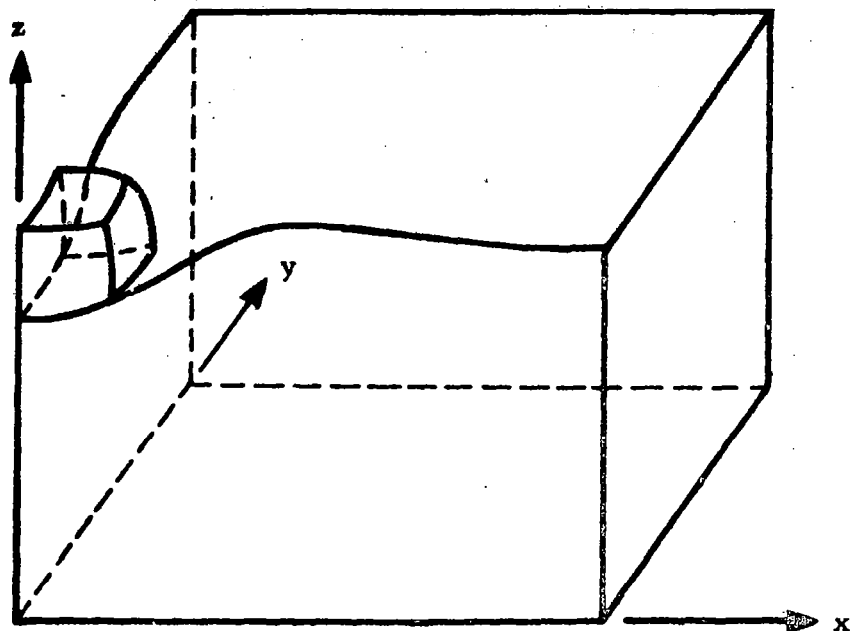


Fig. 5-1 - Target-Projectile Configuration with Target Free Surface Defined by $h(x, y, t)$

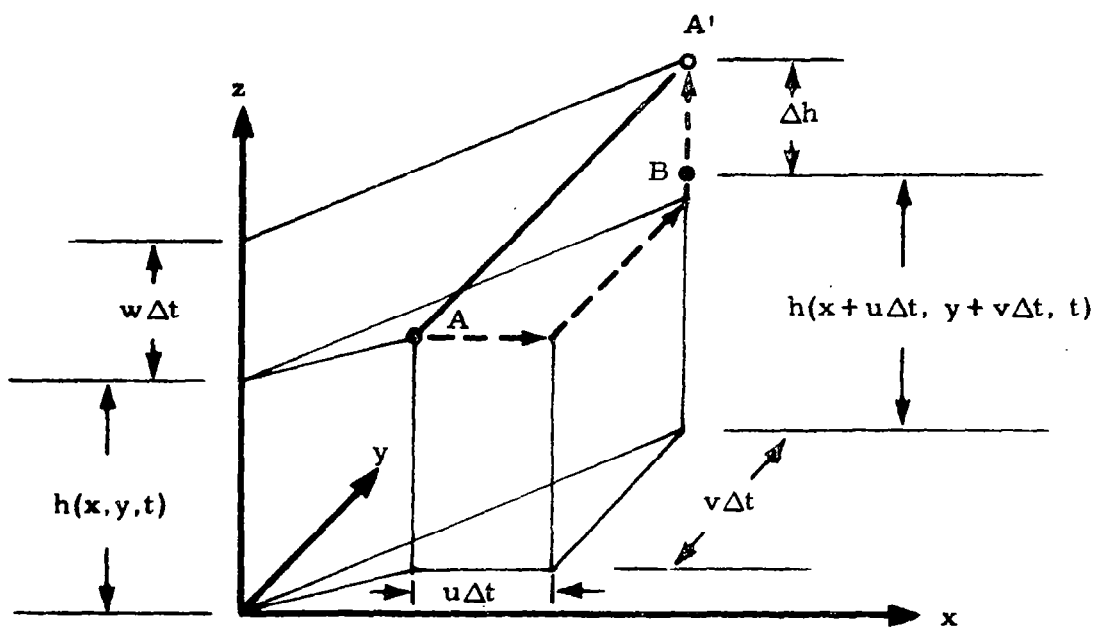


Fig. 5-2 - Motion of Points on Free Surface

The advantage of this approach is its formulation can be incorporated into the coupled Eulerian-Lagrangian code directly as part of the code in the rezoning process. However, since Eq.(5.17) has the similar form as the governing equations, similar problems on numerical instability may arise during the computations. This problem remains to be investigated in future studies.

5.4.2 Method of Extrapolation

Recently, an improved numerical finite element procedure is proposed by France [35]. The approach is applied to deal with two-dimensional steady state free surface problems. As an alternative to adjust the mesh in order to accommodate the movement and subsequent location of the free surface as in the previous method, extrapolation is used in conjunction with a fixed finite element grid. The exact position of the free surface is determined when the imposed boundary conditions are satisfied.

The extension of this approach into three-dimensional problems is straight-forward. The following illustrates the procedure with a linear brick type element. A typical element in the physical domain with the interface passing through is depicted in Fig. 5-3. Here the shaded area represents the free surface which cuts the edges of the element at a, b, c, d . The nodal points of the element are denoted by $1, 2, \dots, 8$.

Let $\psi(x, t)$ be a function whose value on the free surface is specified. At each time step, we assume that the function can be approximated as

$$\psi = N_r \psi_r, \quad r = 1, 2, \dots, m \quad (5.19)$$

Then, the value of ψ at the point a can be expressed as

$$\psi_a = \frac{1}{2} [(1+h_a)\psi_1 + (1-h_a)\psi_5] \quad (5.20)$$

where $(1, -1, h_a)$ is the location of a based on the local coordinate system. Thus, the nodal value of ψ at node 5 can be obtained as

$$\psi_5 = [2\psi_a - (1 - h_a)\psi_1] / (1 + h_a) \quad (5.21)$$

The values of ψ at nodes 6, 7 and 8 can be obtained in the similar way. The matrix equation for the entire boundary surface is thus generated in terms of the values at points of the free surface cutting the edges of all "boundary" elements. But all values of ψ at "boundary" nodes are computed from the previous time step, and ψ on a, b, c, \dots are all specified. Hence, the shape of the free surface can be obtained by solving this matrix equation.

It is seen that this approach is simpler to formulate compared to the previous one, and the computations involve only algebraic equations. Since the element geometry is "fixed", it is only necessary to formulate the governing matrix equation for the initial cycle. These facts can naturally save computation time considerably.

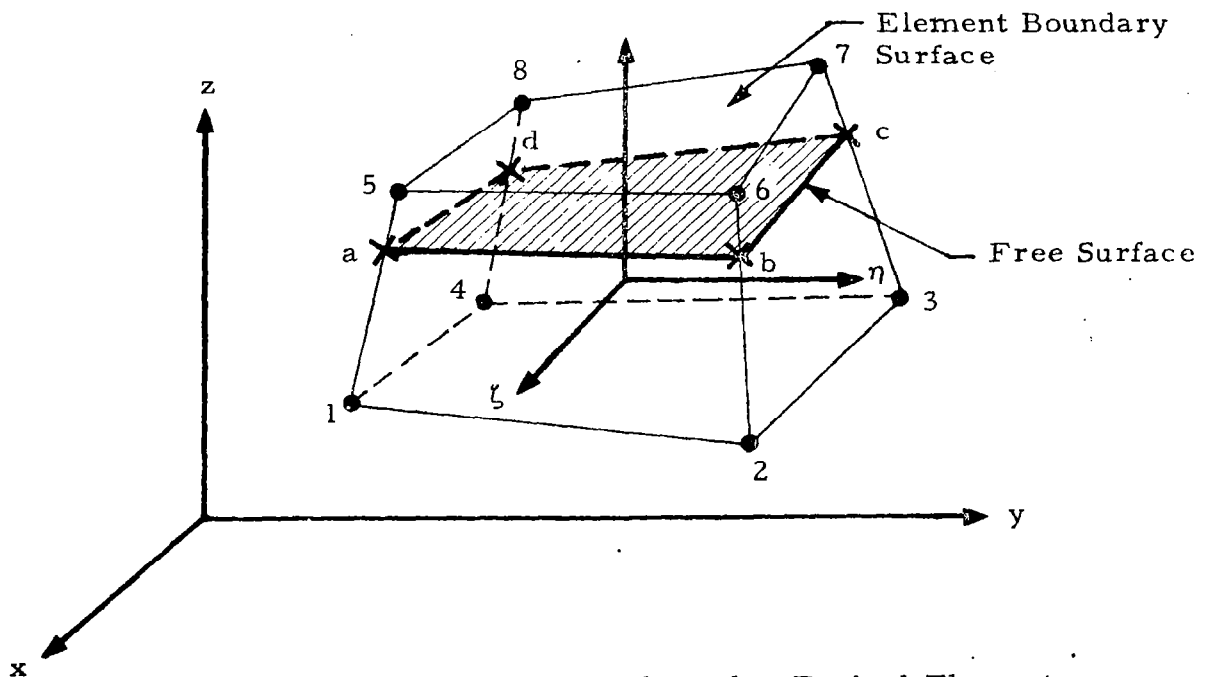


Fig. 5-3 - Free Surface Passing Through a Typical Element

5.5 SCHEME FOR SOLVING A LARGE SYSTEM OF EQUATIONS

As is seen now, the numerical solution of the subject problem must deal with a system of governing partial differential equations. With the methods proposed herein, these equations are solved separately but coupled through iterations, thus reducing computer storage requirements to a great extent. However, for a general three-dimensional problem even with only one equation to solve, a solution with adequate accuracy will generally involve a large number of unknown parameters and hence result in a large system of algebraic equations. Therefore an effective scheme for solving such system of equations is obviously needed.

The various methods to solve a large system of algebraic equations can be classified either as a direct elimination process or as an indirect iterative process. The direct elimination process solves the system at a minimum number of arithmetic operations while storage is at a maximum. For a large scale problem, even with the banded nature of the matrix taken into consideration, the storage can still easily exceed the core memory available on most existing computers. Thus, any large system equation solver would have to make provision for efficient transfer of data between core memory and auxiliary memory. The iterative process, on the other hand, requires only a minimum storage while the number of arithmetic operations, due to the iterative nature, is not definite. For matrix with diagonal dominance, the convergence is fast, but for any other matrix the convergence is usually slow or even not convergent at all.

Traditionally, the finite element workers have favored the direct elimination process for the following reason. The structural problems are mostly linear, or in case of nonlinear problems the nonlinear terms can conveniently be moved to the right-hand side with the load vector. Thus, for a given structure, the decomposed coefficient matrix is invariant and the most time consuming decomposition process needs only be performed once and for all. This decomposed matrix can then be used over and over to obtain a new solution corresponding to a new loading at a later time. It can also be used to obtain

an updated solution in an iterative scheme for nonlinear problems. This resolving capability of the direct elimination process makes it extremely attractive.

Efforts have also been concentrated on storing only the nonzero coefficients together with an auxiliary pointer matrix to record their locations. For input purposes, this scheme certainly saves a lot of storage. Unfortunately, nonzero coefficients are generated within the band in the decomposition process. Thus, the decomposed matrix would be relatively dense and it appears that there can be no saving on storage at output. In addition, some elaborate scheme is required to keep track of these generated nonzero coefficients.

At this time, no definite conclusion has yet been reached whether to use the direct elimination process or the iterative process. It appears that storing the entire band matrix in core memory or auxiliary memory, and using the direct elimination process would be a good approach. Recently, two computer programs based on such an approach were published. The program due to Wilson et al. [36] was written for a positive definite symmetrical band matrix, while the program by Vendhan et al. [37] can take either symmetric or unsymmetrical band matrix. On the other hand, the iterative process such as the "Frontal Solution Technique" [38] is also very attractive for its minimal storage requirements and consideration of the nonlinearity of a problem. All these equation solvers are under study for possible inclusion in the final computer program.

6. TEST PROBLEMS AND NUMERICAL RESULTS

In this section we discuss, in detail, both the inviscid hydrodynamic model and hydroelasto-viscoplastic model of a one-dimensional impact problem. Subroutines for numerical evaluation of shape functions, generation of matrix equations, as well as the equation solver, etc., are tested and debugged by solving various cases of heat conduction problems. The finite element/Galerkin procedure discussed in Section 4 is employed to solve the problem, and the details are presented in the Subsection 6.1. In the second subsection, we shall discuss the inviscid hydrodynamic code in some extent. Included in the discussions will be the numerical experiments of the given test problems in impacts, the comparisons between the methods of weighted residuals and the improved scheme discussed in Section 5, and some related aspects concerning the numerical technique. The hydroelasto-viscoplastic model will be discussed in the last subsection.

6.1 HEAT CONDUCTION IN SOLIDS

The heat conduction problem was chosen to test and debug a number of subroutines such as the numerical evaluation of shape functions and their derivatives for various three-dimensional isoparametric elements, assembly routine, time marching schemes, and equation solver, etc. The problem had been analyzed rather thoroughly to give us confidence in these subroutines, however, for brevity, only major results are presented herein.

As is well known, the heat conduction problem is governed by the diffusion equation in the following form

$$\frac{\partial T}{\partial t} = \nabla^2 T \quad (6.1)$$

subjected to an initial condition and to a set of boundary conditions that are admissible to the equation. Note that the variables in (6.1) and in what follows are all normalized by the characteristic length, time and temperature.

The steady state solution of the problem, i.e., the asymptotic solution of (6.1) at $t \rightarrow \infty$, is identical to the solution of Laplace equation:

$$\nabla^2 T = \frac{\partial^2 T}{\partial x^2} + \frac{\partial^2 T}{\partial y^2} + \frac{\partial^2 T}{\partial z^2} = 0 \quad (6.2)$$

subject to the same set of boundary conditions of either specifying the temperature, or the normal derivative of the temperature, or a combination of both, as in the unsteady case. This problem, when cast in a variational form, has the following integral expression

$$\begin{aligned} I = & \iiint_V \frac{1}{2} \left[\left(\frac{\partial T}{\partial x} \right)^2 + \left(\frac{\partial T}{\partial y} \right)^2 + \left(\frac{\partial T}{\partial z} \right)^2 \right] dV \\ & - \iint_S \left(q T + \frac{1}{2} \alpha T^2 \right) dS \end{aligned} \quad (6.3)$$

It can be shown that, upon minimizing the above integral (i.e., $\delta I = 0$), one will obtain (6.2) together with the following natural boundary condition,

$$\frac{\partial T}{\partial n} = q + \alpha T \quad (6.4)$$

Standard finite element procedures are then applied, based on (6.3) to obtain a system of algebraic equations in the form:

$$\beta_{ij} T_j = \gamma_i \quad (6.5)$$

where

$$\begin{aligned} \beta_{ij} = & \iiint_V \left(N_{i,x} N_{j,x} + N_{i,y} N_{j,y} + N_{i,z} N_{j,z} \right) dV \\ & - \iint_S \alpha N_i N_j dS \end{aligned} \quad (6.6)$$

and

$$\gamma_i = \iint_S q N_i dS$$

In the above, β_{ij} is the influence coefficient matrix, γ_i is the load matrix, and the repeated index j implies summation from 1 to m , the total number of unknown parameters. N_i and $N_{i,x}$ etc., are the shape functions and their derivatives, respectively. Since isoparametric elements are used, numerical integration scheme described previously is used to obtain these matrices.

Two sample problems were chosen to check out the computer codes. They are the heat conduction in a cube and that in a hollow sphere, for which analytic solutions are available for comparison purposes (see Carslaw and Jaeger, [39], pp. 177-179, and pp. 230-231).

6.1.1 Steady State Heat Conduction in a Cube

Let us consider a cube (see Fig.6-1a) defined by

$$0 \leq x \leq a, \quad 0 \leq y \leq b, \quad 0 \leq z \leq c$$

subject to the following boundary conditions

$$T = T_1 \quad \text{on } x = 0$$

$$T = T_2 \quad \text{on } x = a$$

$$T = 0 \quad \text{on other surfaces}$$

The analytic solution in terms of infinite series is

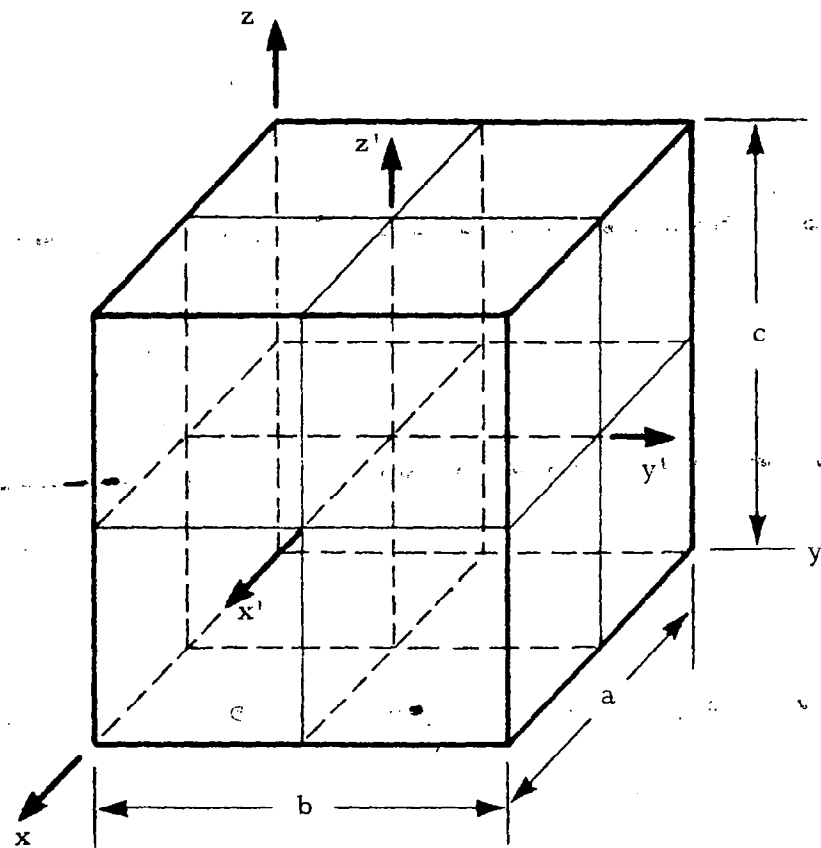
$$T = \frac{16}{\pi^2} \sum_{m=0}^{\infty} \sum_{n=0}^{\infty} \frac{\left[T_1 \sinh \ell(a-x) + T_2 \sinh \ell x \right] \sin \frac{(2m+1)\pi y}{b} \sin \frac{(2n+1)\pi z}{c}}{(2m+1)(2n+1) \sinh \ell a}$$

in which

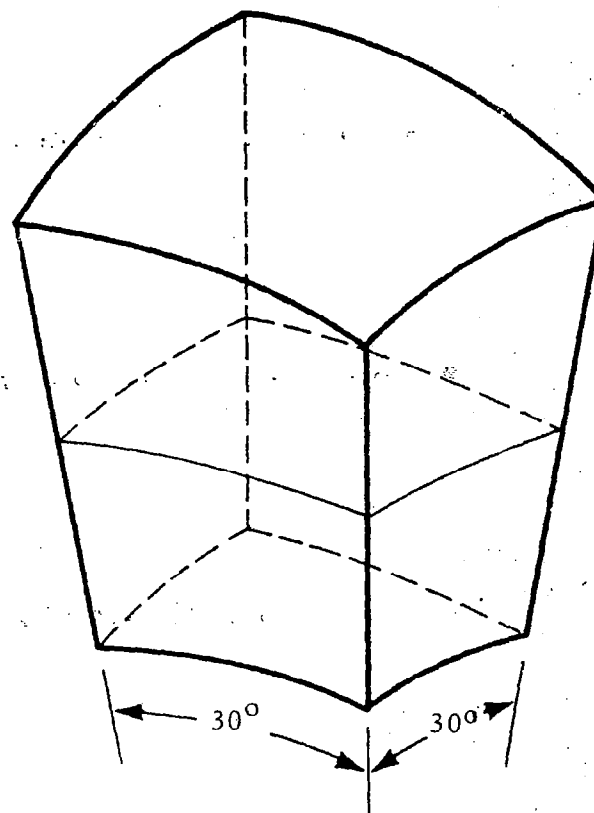
$$\ell = \left\{ \left[\frac{(2m+1)\pi}{b} \right]^2 + \left[\frac{(2n+1)\pi}{c} \right]^2 \right\}^{1/2}$$

For numerical computations, the element mesh shown in Fig. 6-1a is used together with $a = b = c = 1$, $T_1 = 0$ and $T_2 = 1$. To impose the boundary conditions on the surfaces of the cube, the nodal parameters on these surfaces are set equal to 0.0 or 1.0 accordingly. However, because the temperature is double-valued along the four edges of the surface $x = a$, some average scheme has been adapted to take care of this singular behavior, with the four corner-node parameters set equal to $1/3$ and the remaining nodal parameters on the edges set equal to $1/2$. An alternate approach to resolve this difficulty is to use another grid with finer mesh arranged in the aforementioned region. With the present uniform mesh (two elements in each direction), computations have been carried out using both the cubic and quadratic isoparametric elements. Our results, as shown in Fig. 6-2, appear to compare well with the series solution and the property of symmetry about the y' - and z' -axes was also observed. Both sets of finite element results show some oscillation about the series solution, this waviness is believed due to the relatively coarse mesh used and the singular behavior of the boundary condition along the four edges on surface $x = a$.

6-5



a. Cube



b. Hollow Sphere

Fig. 6-1 - Finite Element Representations by Isoparametric Elements

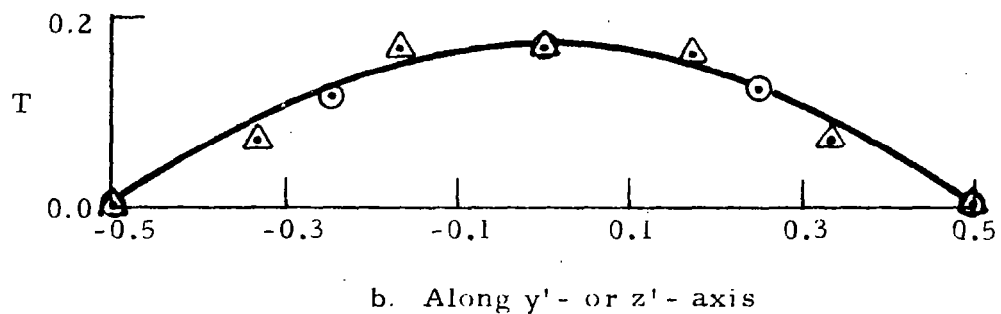
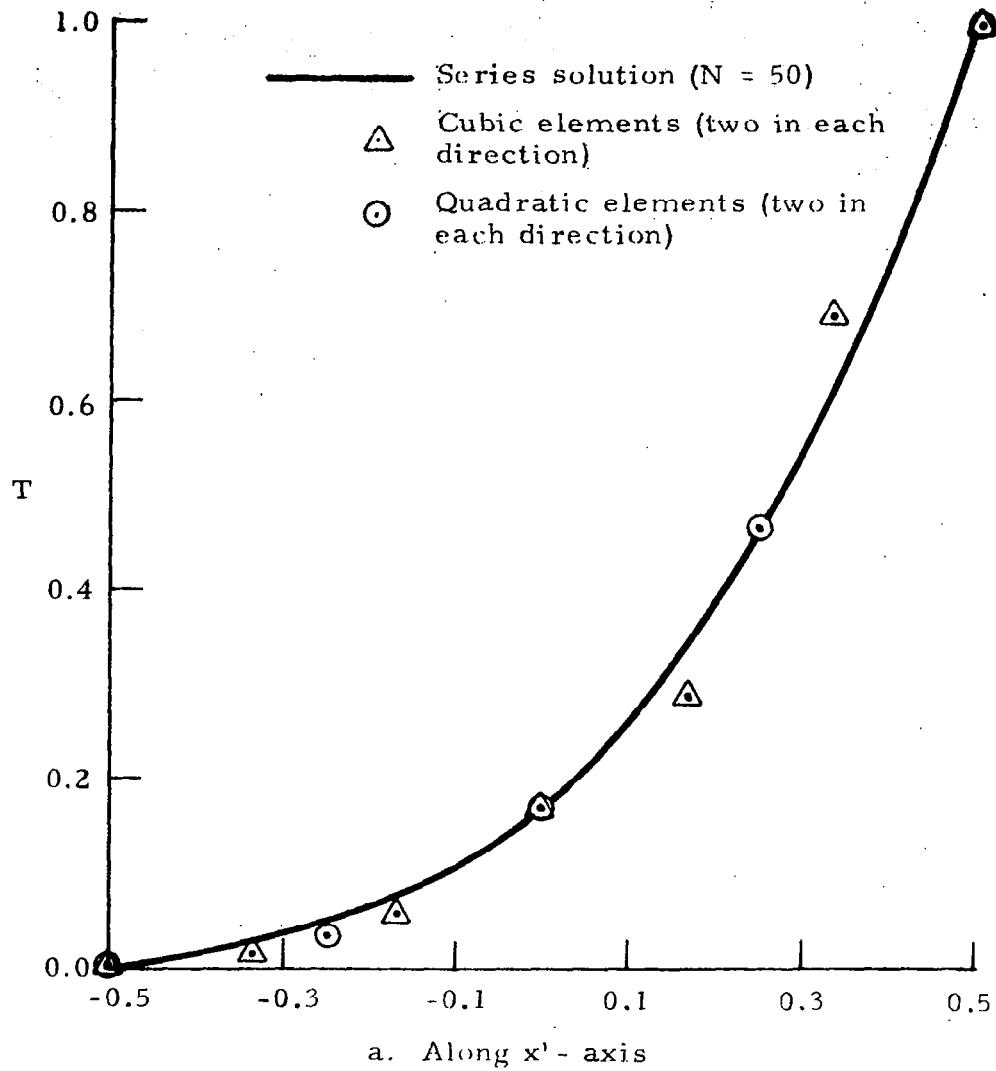


Fig. 6-2 - Comparison of Predicted Temperature Distribution in a Cube

6.1.2 Steady State Heat Conduction in a Hollow Sphere

The hollow sphere is defined by $a \leq r \leq b$, subject to the boundary conditions

$$T = T_1 \quad \text{on } r = a$$

and

$$T = T_2 \quad \text{on } r = b$$

The analytic solution is in the following form

$$T = \frac{a(b-r)T_1 + b(r-a)T_2}{r(b-a)}$$

Because the solution is a function of r only, a prism as shown in Fig. 6-1b was taken for computations. The inner and outer radii of the hollow sphere were chosen to be 1.0 and 2.0, respectively. The boundary conditions imposed on the prism are

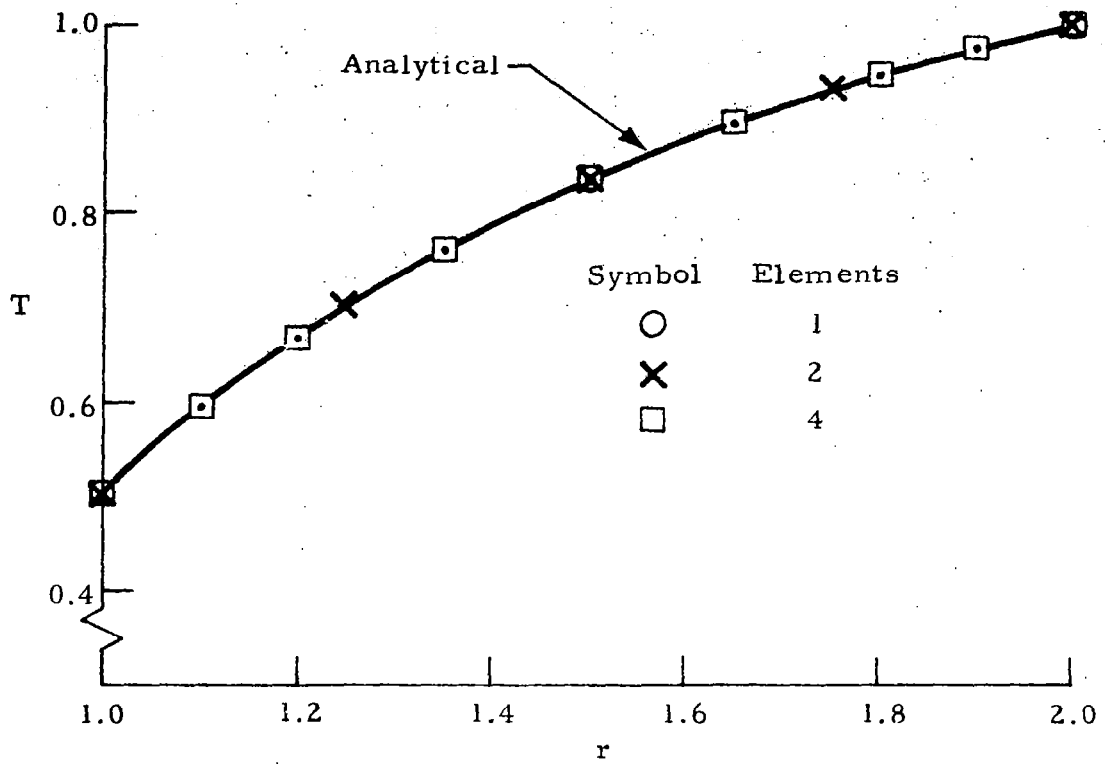
$$T = 0.5 \quad \text{on } r = 1.0$$

$$T = 1.0 \quad \text{on } r = 2.0$$

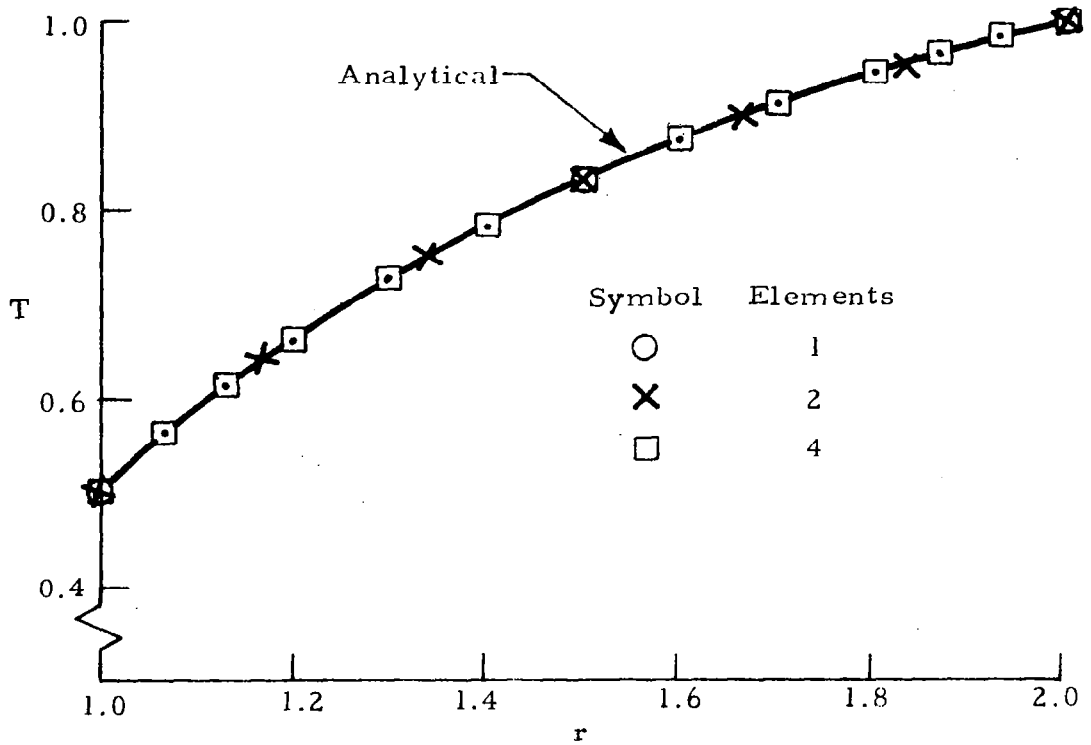
and

$$\frac{\partial T}{\partial n} = 0 \quad \text{on other surfaces}$$

Again, both quadratic and cubic isoparametric elements have been used in the computations, with results shown in Fig. 6-3. As is seen, there exists excellent agreement between our predicted results and the analytic solution, even with only one element. Results obtained by using finer meshes are almost identical to the analytic solution. The high accuracy achieved by the present analysis is obviously attributable to the ability of isoparametric elements to represent both the geometry and the solution function accurately. Also, for the present problem, the well posed boundary conditions (no singular behavior) make it easier to obtain an accurate numerical solution with relatively few elements.



a. With Quadratic Isoparametric Elements



b. With Cubic Isoparametric Elements

Fig.6-3 - Comparison of Predicted Temperature Distribution in the Radial Direction of a Hollow Sphere

6.1.3 Transient Solution

The time marching schemes discussed in Subsection 4.4 have been tested numerically for the three-dimensional transient heat conduction problem. The governing differential equation now has the form

$$\frac{\partial T}{\partial t} = \frac{\partial^2 T}{\partial x^2} + \frac{\partial^2 T}{\partial y^2} + \frac{\partial^2 T}{\partial z^2} \quad (6.1)$$

with initial and appropriate boundary conditions. By applying the Galerkin technique with respect to the space variables, a system of algebraic equations, with an additional term involving time derivative, is obtained

$$\alpha_{ij} \dot{T}_j + \beta_{ij} T_j = \gamma_i \quad (6.7)$$

where

$$\alpha_{ij} = \iiint_V N_i N_j dV$$

$$\beta_{ij} = \iiint_V (N_{i,x} N_{j,x} + N_{i,y} N_{j,y} + N_{i,z} N_{j,z}) dV - \iint_S \alpha N_i N_j dS$$

and

$$\gamma_i = \iint_S q N_i dS \quad (6.8)$$

The steady state solution of the hollow-sphere problem was again selected as the testing case. The tests include different time marching schemes, size of time step, various order of elements, and effects of initial conditions. The solution is considered as reaching steady state when certain prescribed convergence criterion is satisfied. The one presently used is that for every

undetermined parameter the difference between two consecutive time steps must be less than 10^{-4} . All the testing cases except one ($\Delta t = 2.0$ in Fig. 6-4) satisfy this criterion in less than ten time steps. Figures 6-4 through 6-8 show some of the results.

Figure 6-4 shows the temperature history at the point $r = 1.5$ obtained by the implicit finite difference scheme with $\theta = 0.5$ (i.e., the Crank-Nicholson type), using two linear elements. Although the results show some oscillation about the steady state solution the scheme is obviously stable, regardless of time step size. The scheme of two-step Galerkin in time (equivalent to $\theta = 2/3$ in the implicit finite difference scheme) was also tested for the same problem, with results shown in Fig. 6-5. Oscillation about the steady state is seen to be reduced significantly with improved convergence rate, thus demonstrating the merits of the Galerkin process in time. Two additional tests were conducted for cases with quadratic and cubic isoparametric elements together with two-step Galerkin process in time. The trends of convergence for these cases are shown in Figs. 6-6 and 6-7, respectively. For this particular problem, no significant difference is observed in the paths of convergence with various numbers of elements.

Results in Figs. 6-5 through 6-7 were obtained by assuming zero solution throughout the entire field (including those on the boundary) at time $t = 0$. To see how the initial condition affects the solution path, non-zero boundary conditions were also applied from the onset ($t = 0$), and results are shown in Fig. 6-8. Some significant disturbance for the first steps is noticed, especially for cases with a large time step. The disturbance, nevertheless, was quickly damped out and convergent solution is still attainable.

6.1.4 Radiation Boundary Conditions

Subroutines for the boundary integral involving a curved surface has been written and was checked by analyzing the problem of heat conduction in a hollow-sphere subject to "radiation" boundary conditions (see [34], p. 19). Instead of

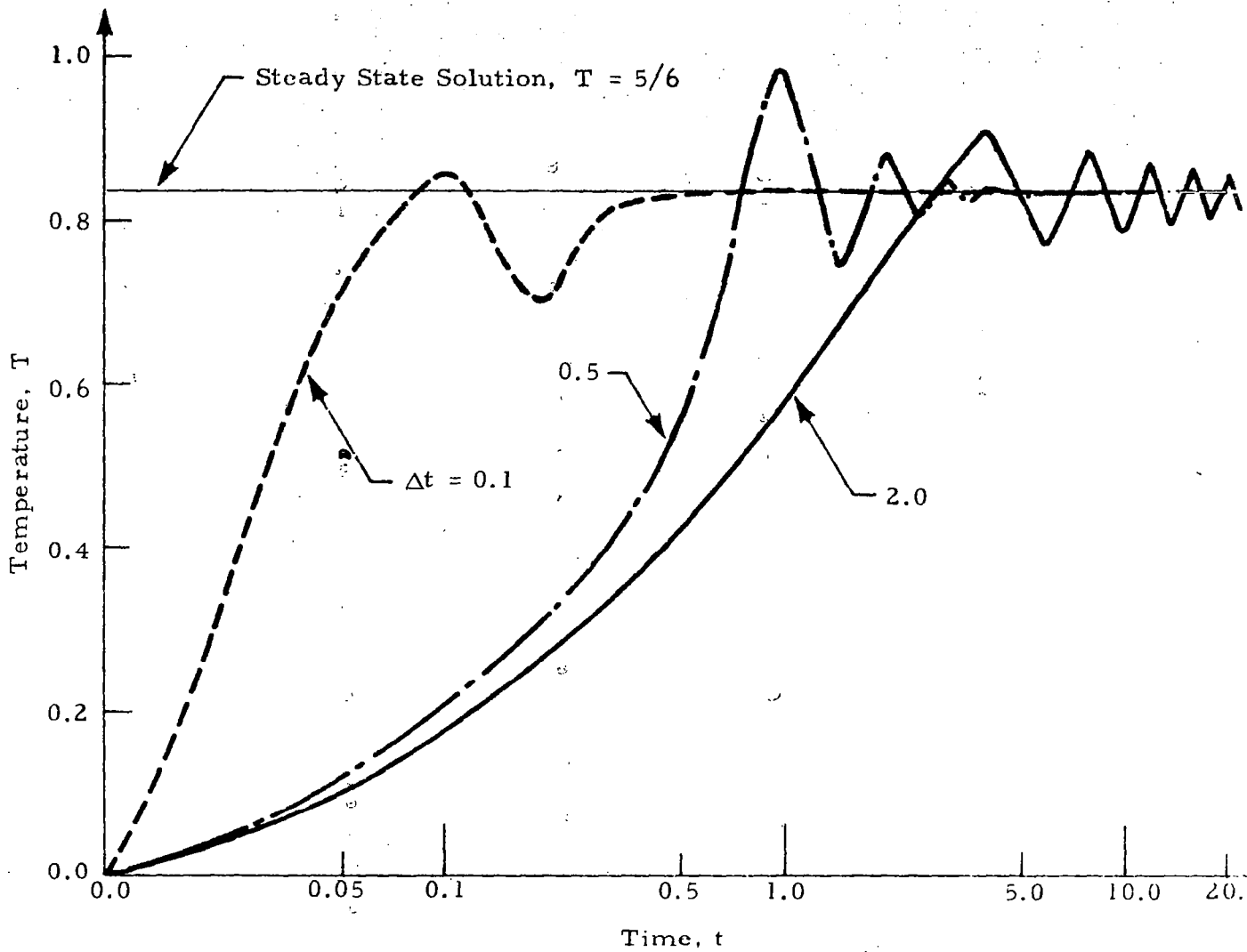


Fig. 6-4 - Predicted Temperature History of a Typical Point ($r = 1.5$) of the Hollow Sphere with Various Time Step Sizes (two linear elements, Crank-Nicholson in time with $\theta = 0.5$)

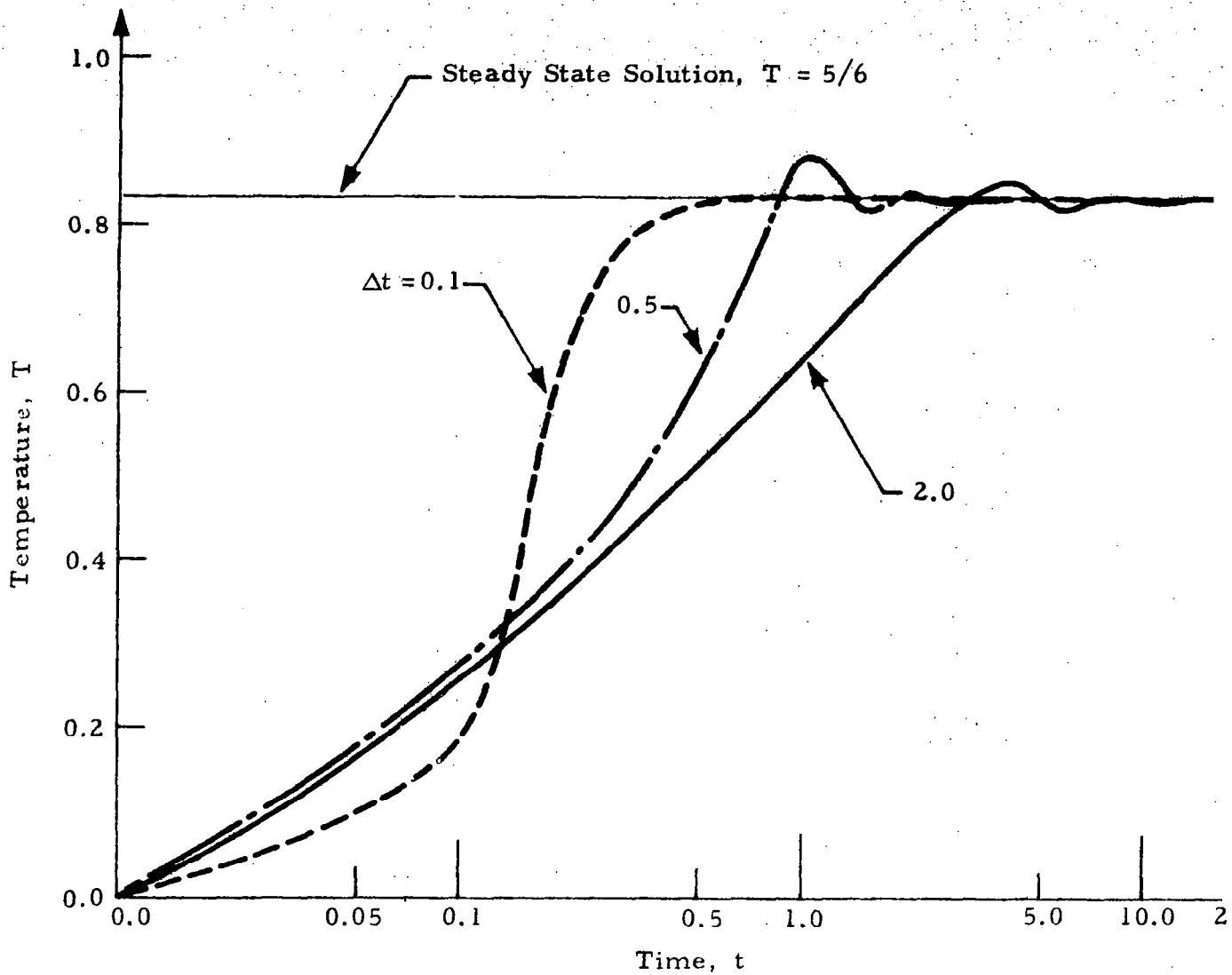


Fig.6-5 - Predicted Temperature History at a Typical Point ($r = 1.5$) of the Hollow Sphere with Various Time Step Size (two linear elements, Galerkin in Time)

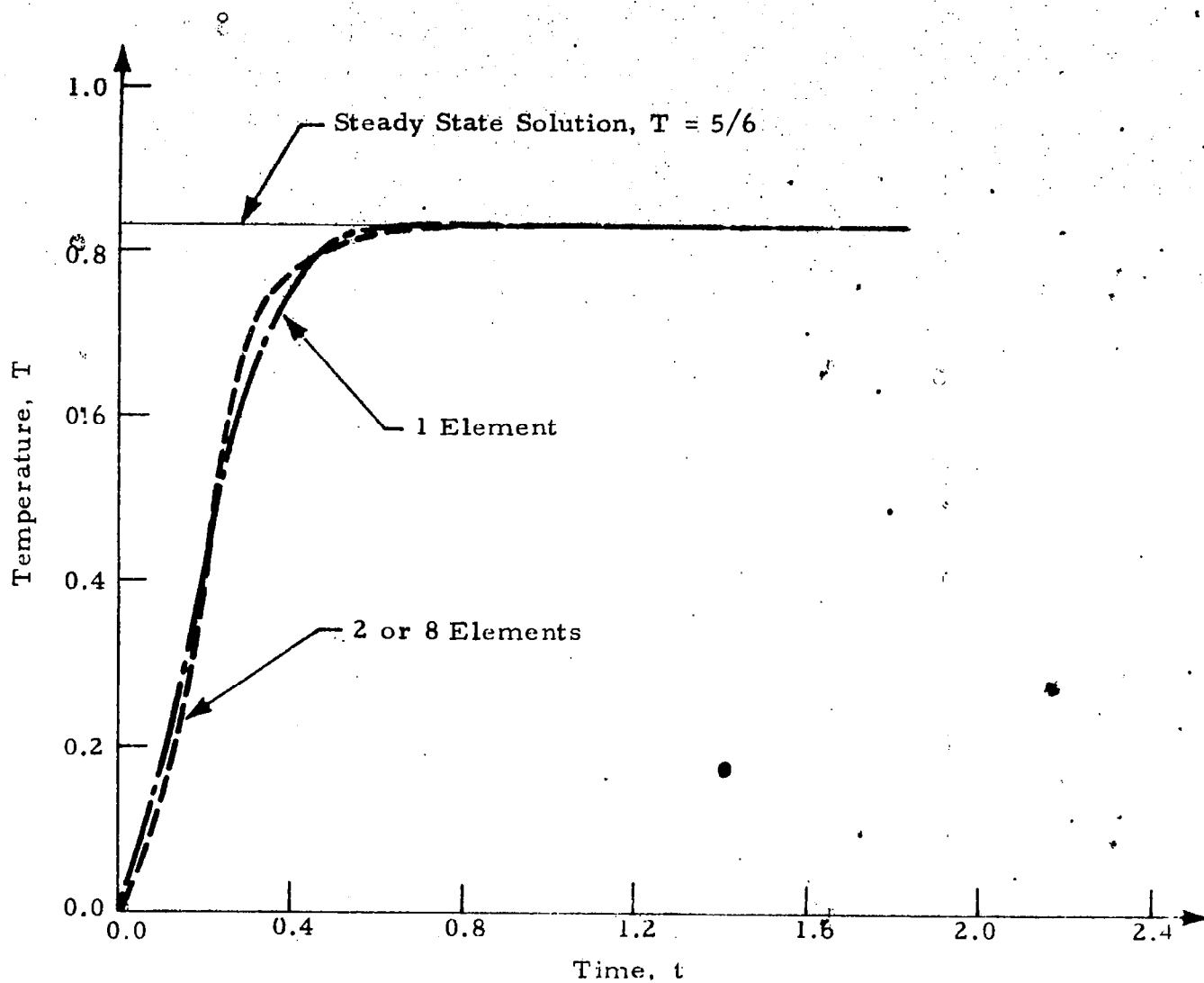


Fig. 6-6 - Predicted Temperature History of a Typical Point ($r = 1.5$) of the Hollow Sphere with Various Number of Quadratic Elements ($\Delta t = 0.2$, Galerkin in Time)

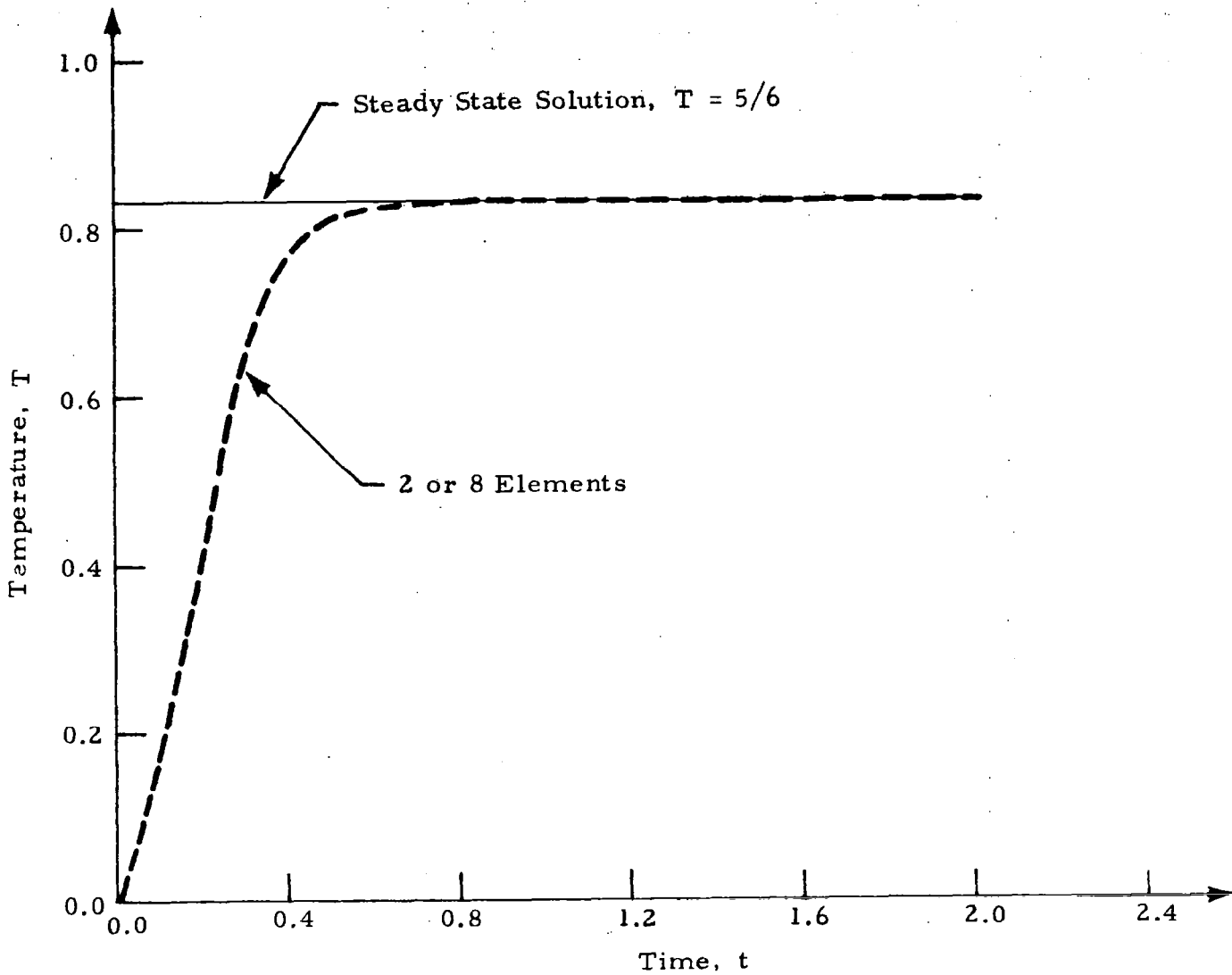


Fig.6-7 - Predicted Temperature History of a Typical Point ($r = 1.5$) of the Hollow Sphere with Various Number of Cubic Elements ($\Delta t = 0.2$, Galerkin in Time)

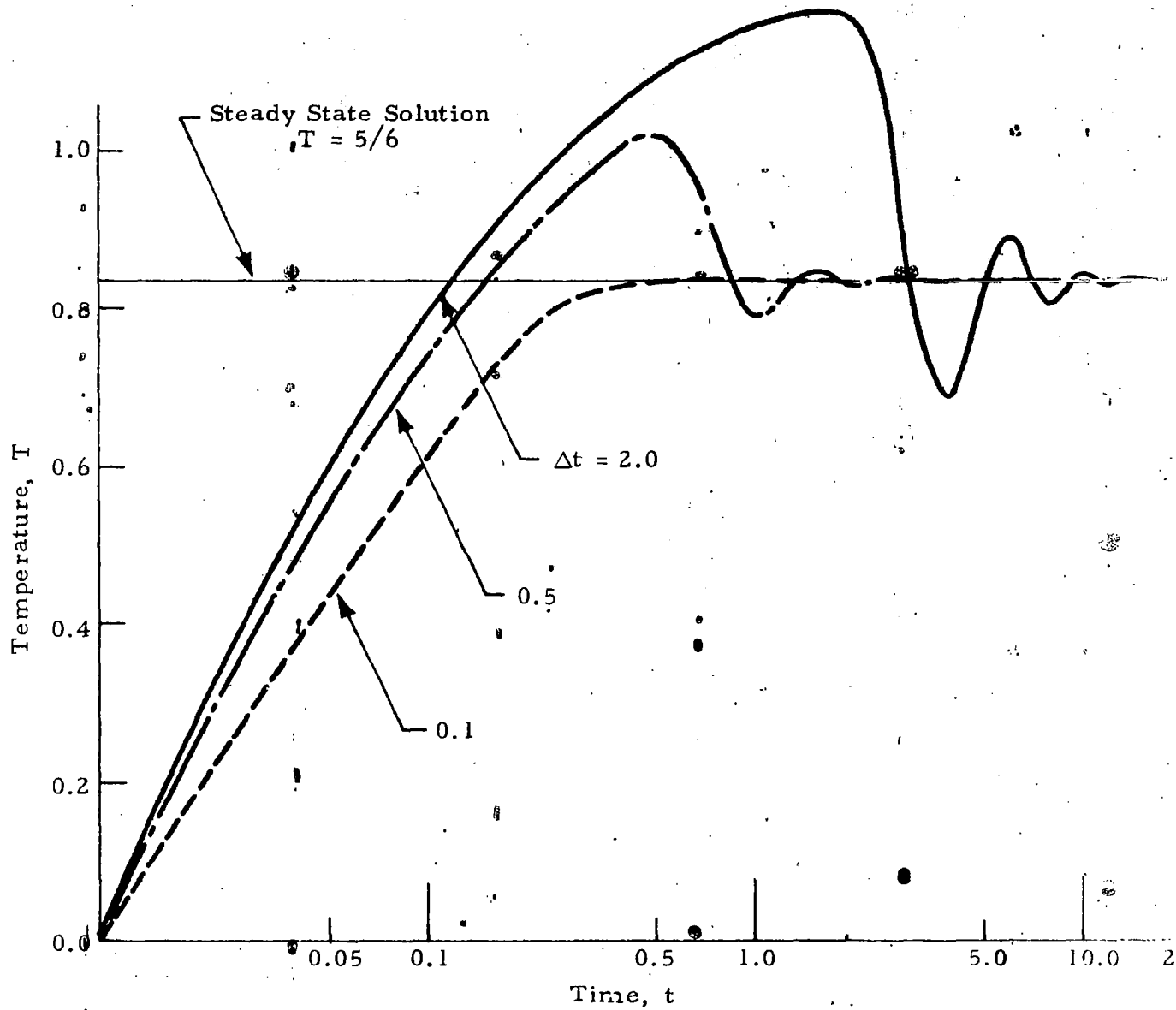


Fig.6-8 - Predicted Temperature History at a Typical Point ($r = 1.5$) of the Hollow Sphere with Non-Zero Boundary Conditions Applied at $t = 0$ (linear elements, Galerkin in Time)

specifying the temperature on the inner and outer surfaces, the boundary conditions are now

$$\frac{\partial T}{\partial n} = h_1 (T_1 - T) \quad \text{at} \quad r = a$$

$$\frac{\partial T}{\partial n} = h_2 (T_2 - T) \quad \text{at} \quad r = b$$

The above expressions indicate: at $r = a$ radiation from the medium at T_1 , and at $r = b$ radiation into the medium at T_2 . h_1 and h_2 represent the ratio of surface conductance to thermal conductivity of the medium. The analytical solution for this problem is

$$T = \frac{T_1 h_1 a^2 [b^2 h_2 - r(bh_2 - 1)] + T_2 h_2 b^2 [r(ah_1 + 1) - a^2 h_1]}{r[b^2 h_2 (ah_1 + 1) - a^2 h_1 (bh_2 - 1)]}$$

For numerical computations, we choose

$$a = 1, \quad b = 2, \quad h_1 = 2, \quad h_2 = 1, \quad T_1 = 0, \quad \text{and} \quad T_2 = 1$$

Then the exact solution becomes

$$T = \frac{6r - 4}{5r}$$

Figure 6-9 shows the predicted temperature distributions using only two elements, linear, quadratic or cubic. The numerical results obtained by using higher order elements and the analytic solution agree very closely; the results obtained by using linear elements, though less accurate, are generally good. Figure 6-10 shows the temperature history at the point $r = 1.5$ with various element representations for the same problem, with Galerkin process in time. In all the cases the solutions converged to the steady state solution (convergence criterion 10^{-4}) within 20 time steps.

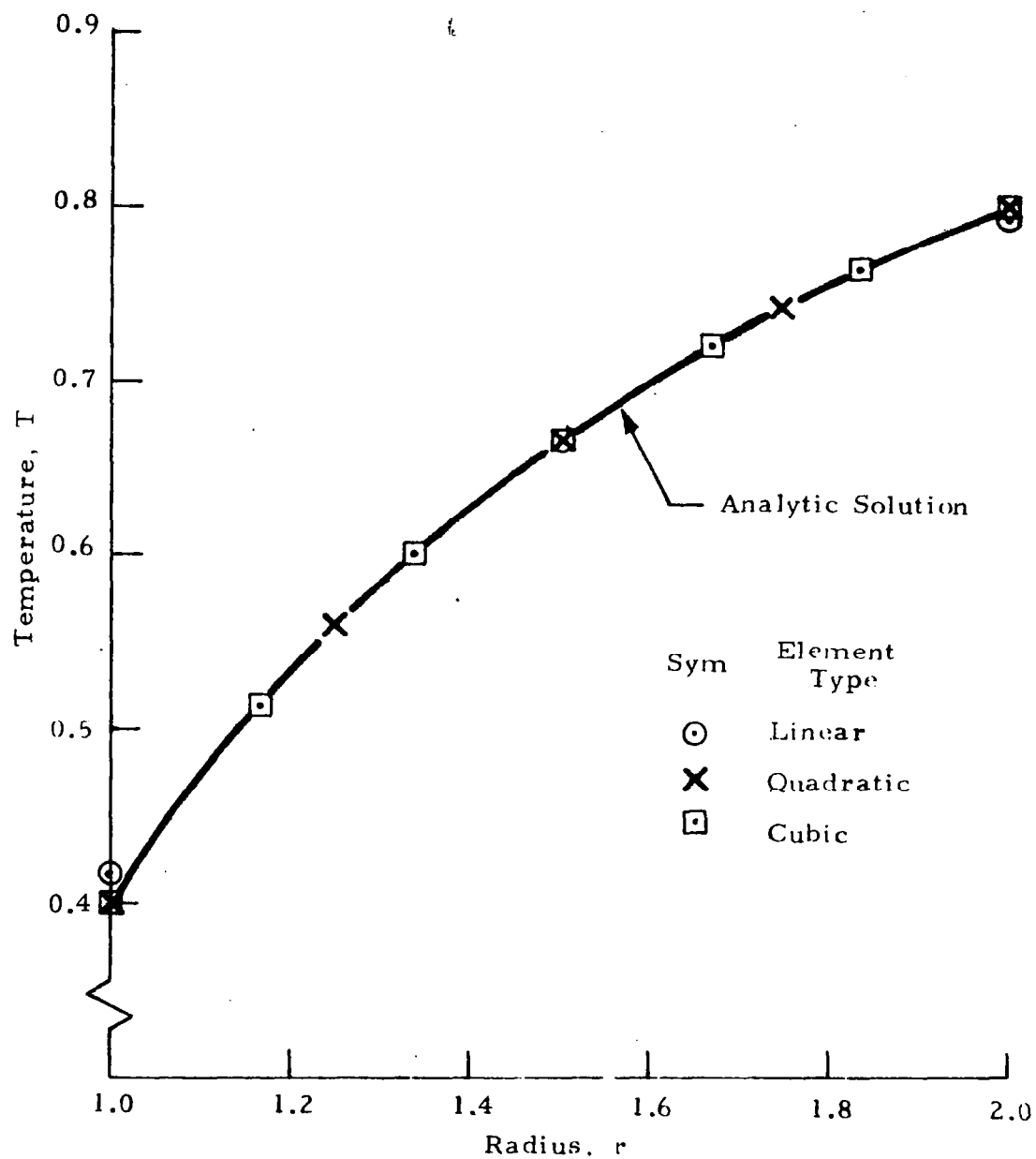


Fig. 6-9 - Comparison of Predicted Temperature Distribution for a Hollow Sphere Subject to Radiation Boundary Conditions

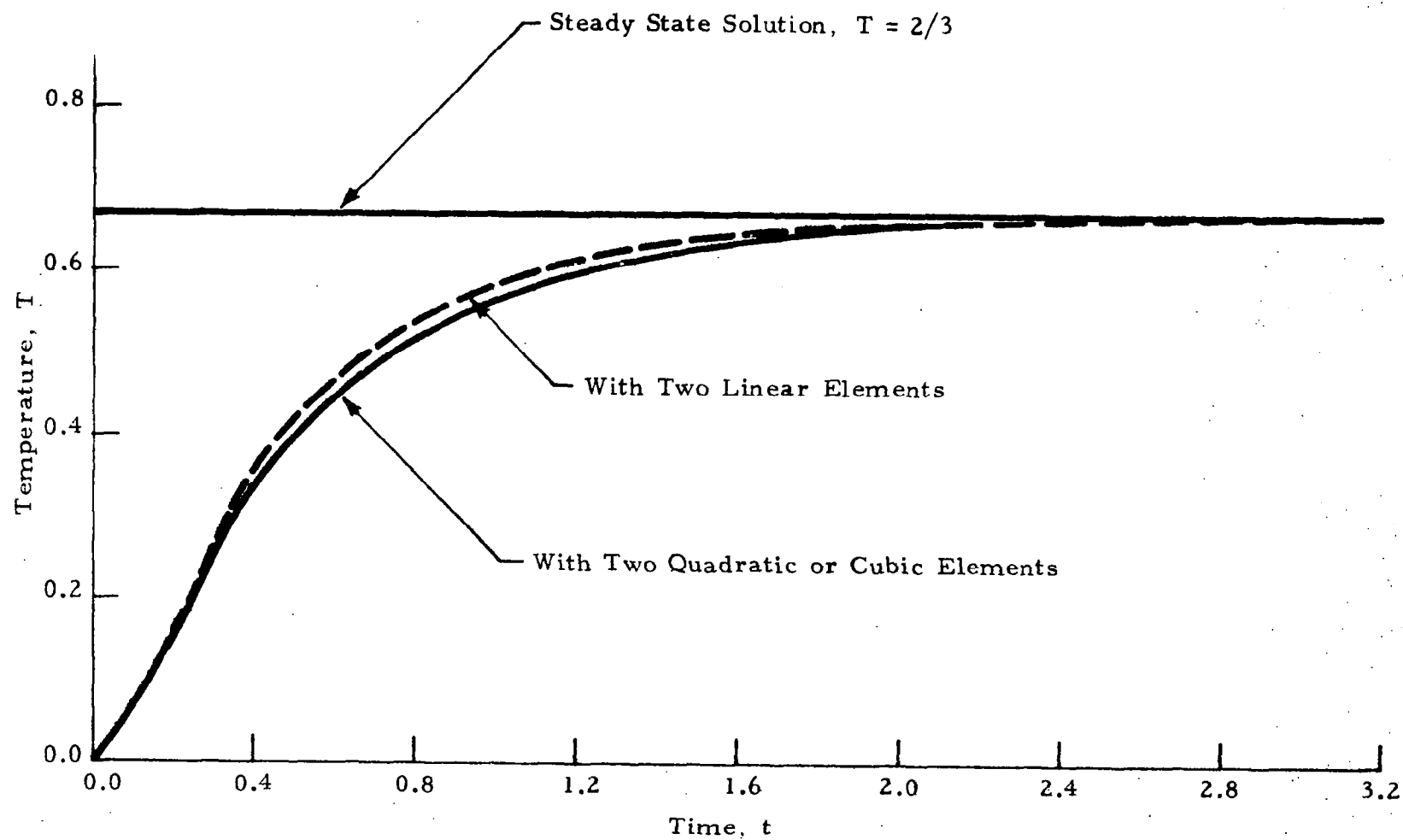


Fig. 6-10 - Predicted Temperature History of a Typical Point ($r = 1.5$) of the Hollow Sphere with Radiation Boundary Conditions ($\Delta t = 0.2$, Galerkin in Time)

5.2 IMPACT PROBLEMS WITH HYDRODYNAMIC MODEL

5.2.1 Description of a Typical Impact Problem

As pointed out in our earlier discussions, a hydrodynamic model is a good approximation in the early stages of the high velocity impact process, during which the pressure is comparable to the shear strengths of the target material. As a starting point we begin with a numerical solution to the hydrodynamic equations with the inviscid adiabatic approximation. In this case the conservation equations, with $\sigma_{ij} = -P \delta_{ij}$, become

$$\begin{aligned}\frac{\partial}{\partial t} (\rho) &= - \frac{\partial}{\partial x_i} (\rho v_i) \\ \frac{\partial}{\partial t} (\rho v_i) &= - \frac{\partial}{\partial x_i} (P) - \frac{\partial}{\partial x_j} (\rho v_i v_j) + \rho f_i \\ \frac{\partial}{\partial t} (\rho e) &= - \frac{\partial}{\partial x_i} (P v_i) - \frac{\partial}{\partial x_j} (\rho e v_j) + \rho f_i v_i\end{aligned}\tag{6.9}$$

view of (4.4), the above equations can be written in the alternate form

$$\begin{aligned}\frac{\partial \rho}{\partial t} + v_i \frac{\partial \rho}{\partial x_i} + \Theta \rho &= 0 \\ \frac{\partial}{\partial t} (V_j) + v_i \frac{\partial}{\partial x_i} (V_j) + \Theta V_j &= - \frac{\partial P}{\partial x_j} + F_j \\ \frac{\partial}{\partial t} (E) + v_i \frac{\partial}{\partial x_i} (E) + \Theta E &= - \frac{\partial}{\partial x_i} (P v_i) + F_i v_i\end{aligned}\tag{6.10}$$

Consider the impact of a cube on a semi-infinite body of possibly dissimilar material at a velocity of V_o . For simplicity we can assume that the target is a semi-infinite cube of dimension four times larger than that of the projectile. Because of the symmetry about the z -axis, it is sufficient to analyze the quadrant bounded by positive x, y, z -axes (see Fig. 6-11). A typical finite element mesh of the projectile-target configuration is shown in Fig. 6-12, which is generated by a program subroutine (MESH). The subroutine generates nodal numbers and their coordinates in the target as well as in the projectile.

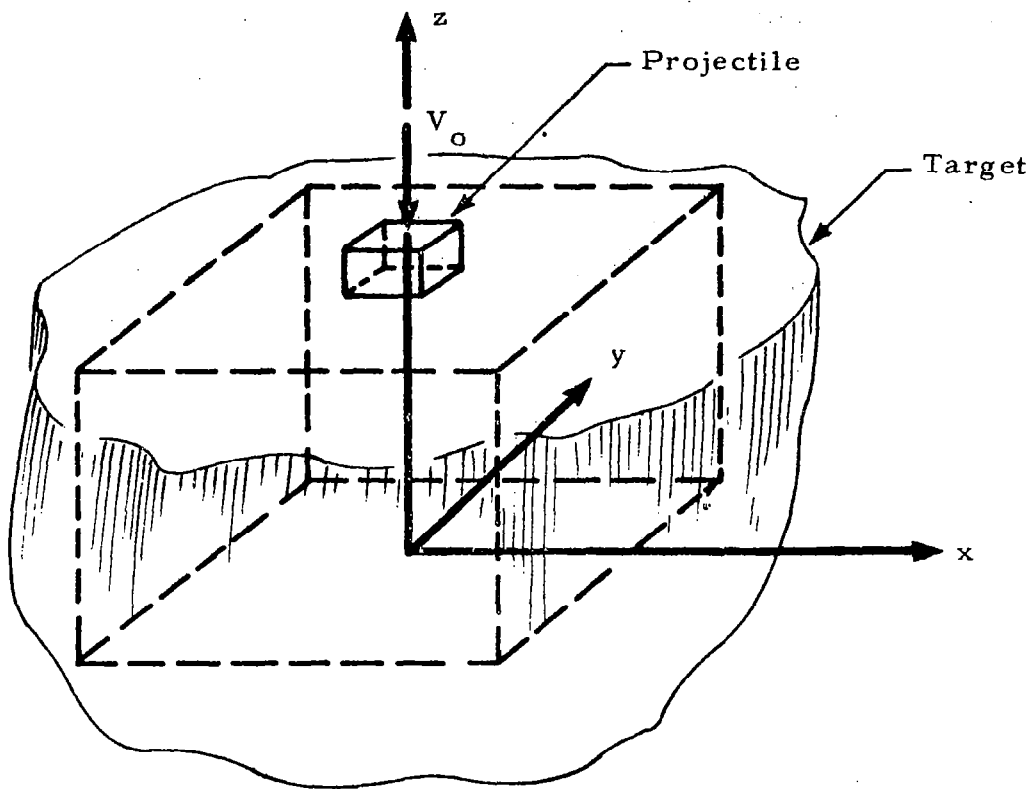
Initial Conditions: We assume that the target is at rest at time $t = 0$. Let S_p denote the set of nodal points in the projectile and S_t denote the set of nodal points in the target. Then $S_o = S_p \cap S_t$ denotes the set of nodal points common to the target and projectile (i.e., on the interface). For $t = 0^+$, we have the following initial conditions for density, pressure, and internal energy.

$$\begin{aligned} \rho_i &= \rho_{ot}, & i \in S_t \\ \rho_i &= \rho_{op}, & i \in S_p \\ P_i &= 0, & i \in S_p \cup S_t - S_o \\ P_i &= P_o, & i \in S_o \\ \epsilon_i &= 0, & i \in S_p \cup S_t \end{aligned}$$

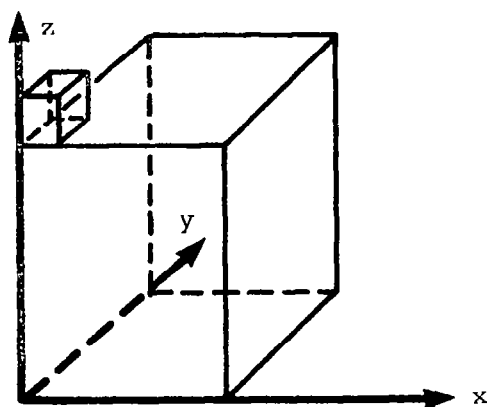
where the subscript "i" refers to the i^{th} node, ρ_{ot} and ρ_{op} being the initial densities of the target and the projectile, respectively, and P_o is the pressure at the interface, and should be calculated from the Rankine-Hugoniot relations for the target and projectile,

Projectile	Target
$P_1 = \rho_{op} (V_o - q) (V_o + U_1)$	$P_2 = \rho_{ot} q U_2$
$(1 - \eta_1) (V_o + U_1) = V_o - q$	$(1 - \eta_2) U_2 = q$
$\epsilon_1 = P_1 (1 - \eta_1) / 2 \rho_{op}$	$\epsilon_2 = P_2 (1 - \eta_2) / 2 \rho_{ot}$

(6.12)



a. Entire Configuration



b. A Quadrant of the Target-Projectile System

Fig.6-11 - Impact of a Cube on Semi-Infinite Target

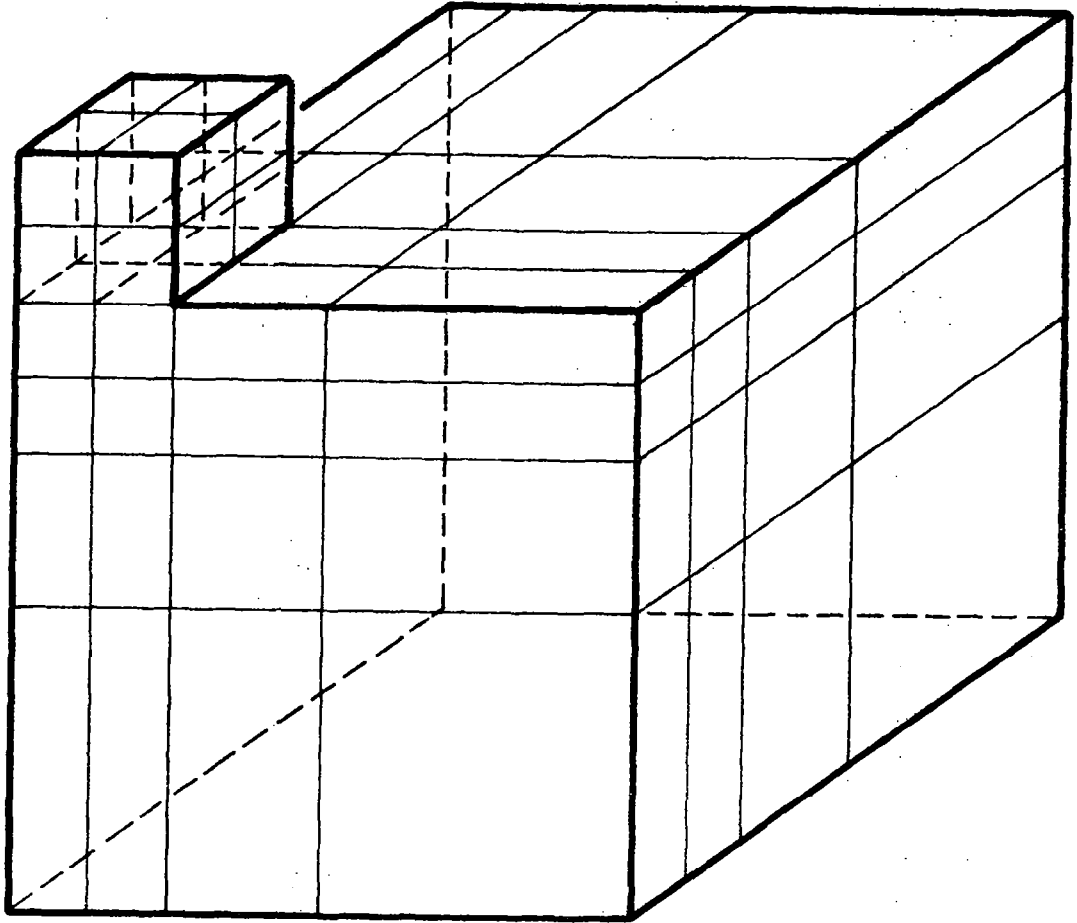


Fig. 6-12 - A Typical Finite Element Mesh of the Projectile-Target Configuration

Here the subscript "1" refers to the projectile and "2" refers to the target; q is the particle velocity at the interface and U is the shock velocity. We have assumed in writing (6.12) that the initial pressure and internal energies are zero. From (6.12) we obtain

$$V_o - q = \sqrt{\frac{P_1}{\rho_{op}}} (1 - \eta_1) \quad (6.13)$$

and

$$q = \sqrt{\frac{P_2}{\rho_{ot}}} (1 - \eta_2) \quad (6.14)$$

The interface pressure is given when $P_1 = P_2 = P_o$. When the projectile and the target are of the same material the interface particle velocity, q , is given by

$$q = V_o/2 \quad (6.15)$$

To calculate the interface pressure P_o at impact we proceed as follows: We have from (6.13) and (6.14),

$$\eta_2 = 1 - \rho_{ot} \frac{V_o}{\sqrt{P_1}} - \sqrt{\frac{1 - \eta_1}{\rho_{op}}} \quad (6.16)$$

For various values of η_1 we can calculate η_2 from (6.16), wherein the pressure P_1 is calculated from the Hugoniot equation of state.

Initial conditions on the velocity components u_i , v_i and w_i in x , y and z -directions, respectively, are

$$\begin{aligned} u_i &= v_i = 0, & i \in S_t \cup S_p \\ w_i &= 0, & i \in S_p - S_o \\ w_i &= -V_o, & i \in S_p - S_o \\ w_i &= -q, & i \in S_o \end{aligned} \quad (6.17)$$

where q is computed from (5.14) (q is equal to $V_o/2$ for like metal impacts).

Another way is to use conditions at $t = 0^-$, the time prior to impact, as initial conditions. To do this, every unknown is set equal to zero except density and those quantities related to impact velocity such as velocity, momentum and total energy in the projectile. These initial data may be discontinuous, which are, of course, taken care of conveniently in the present formulation. This set of initial conditions has been used in most of the computations.

Boundary Conditions: As mentioned earlier the pressure must be zero on the free surfaces. Since the target is semi-infinite, the material particles far away from the impact region are unaffected. Hence, the internal energy and velocities must be zero and the density must be undisturbed. These boundary conditions, together with conditions for the plane of symmetry, are sketched in Fig. 6-13.

Remark on the Equation of State: As mentioned earlier, there are two forms of equation of state being frequently used in high velocity impact problems. They are the Los Alamos equation of state and the Tillotson's equation of state, both obtained from experiment. Obviously values of computed pressure distribution in materials depend heavily on the particular equation of state being used, which in turn will affect the entire numerical solution. Some uncertainty apparently exists regarding the two equations as they do not appear to agree closely in general and each seems to have its own range of validity. For instance, the Los Alamos equation of state and Tillotson's equation of state differ substantially in the case of aluminum (see Figs. 6-14 and 6-15) for internal energy values below $7.5 \text{ Mb-cm}^3/\text{gm}$, and agree closely in the range of 40 to 43 $\text{Mb-cm}^3/\text{gm}$, as seen in Fig. 6-16. Therefore, caution must be exercised when a specific equation of state is employed in the numerical computations, and it seems that a more accurate equation of state is needed.

6.2.2 One-Dimensional Impact Problem

A one-dimensional impact problem is used herein to test the validity of the formulations presented in Sections 4 and 5. The problem under

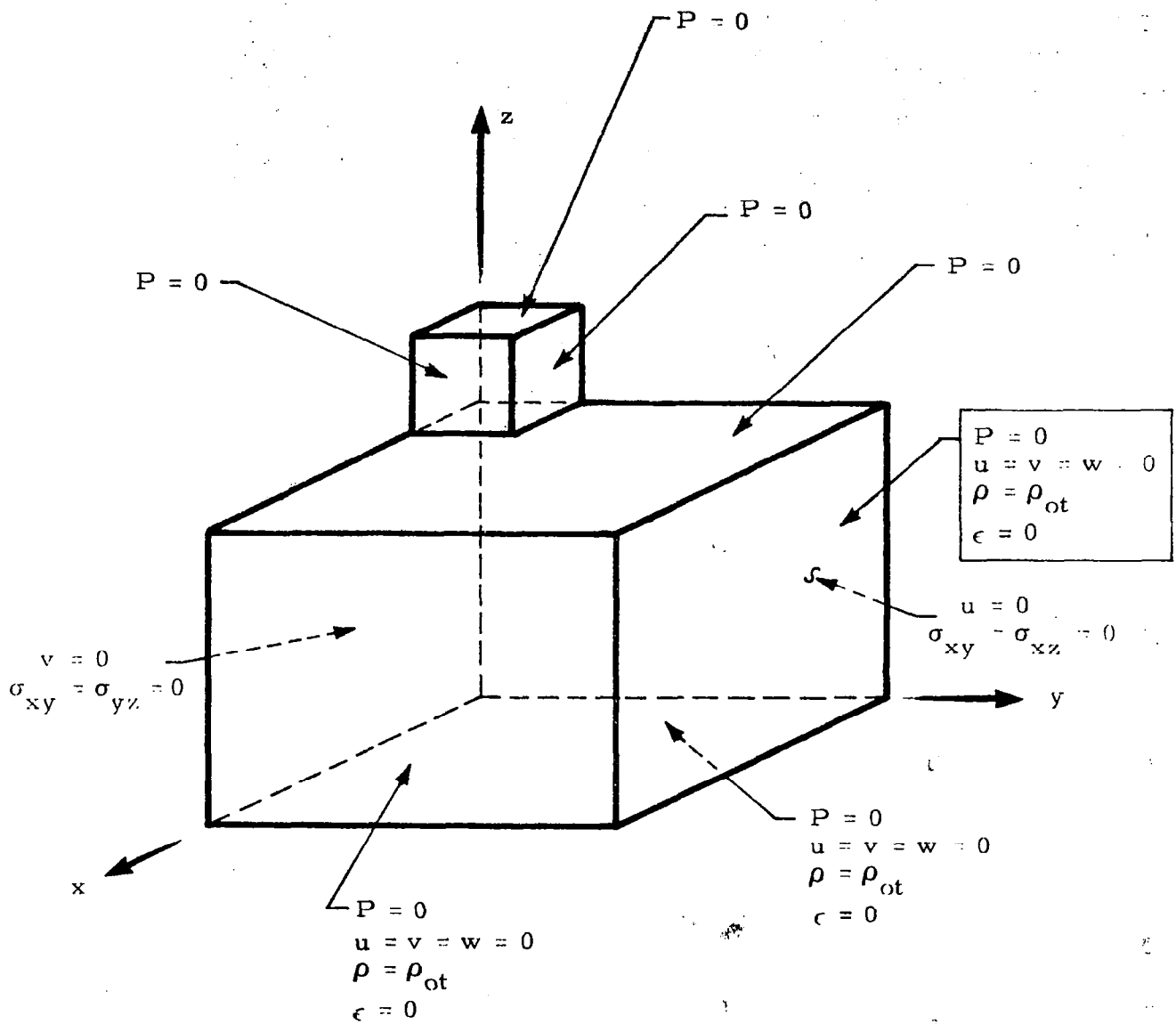


Fig. 6-13 - Boundary Conditions

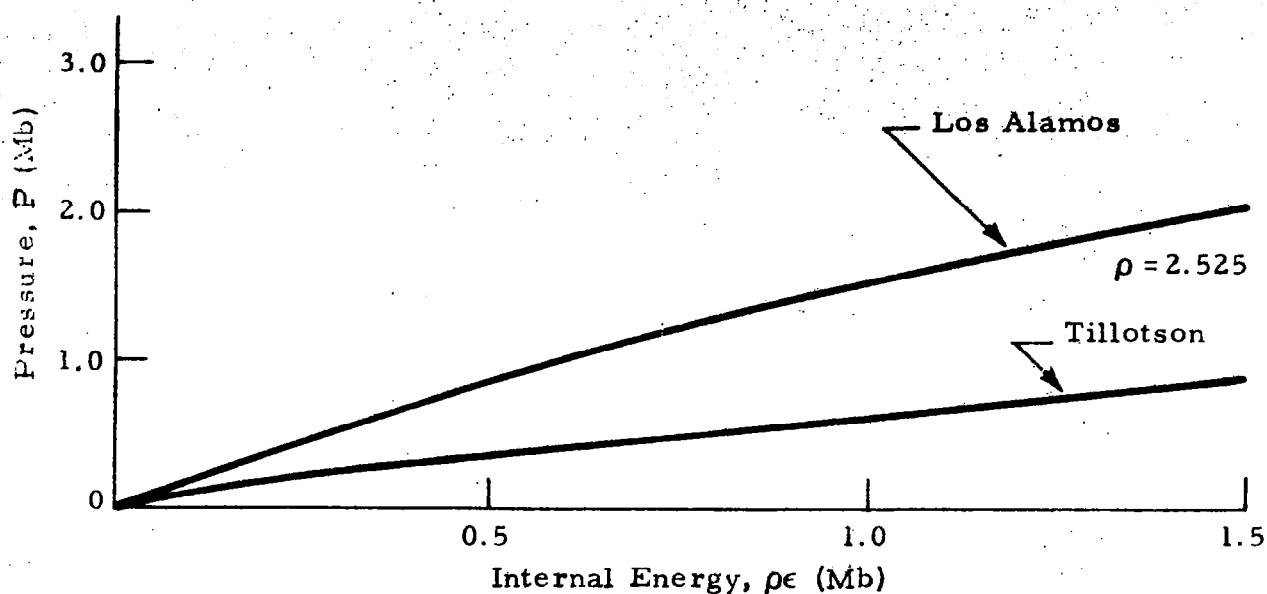


Fig. 6-14 - Variation of Pressure with Internal Energy (Aluminum $\rho_0 = 2.702 \text{ gm/cm}^3, \rho\epsilon = 0 \text{ to } 1.5 \text{ Mb}$)

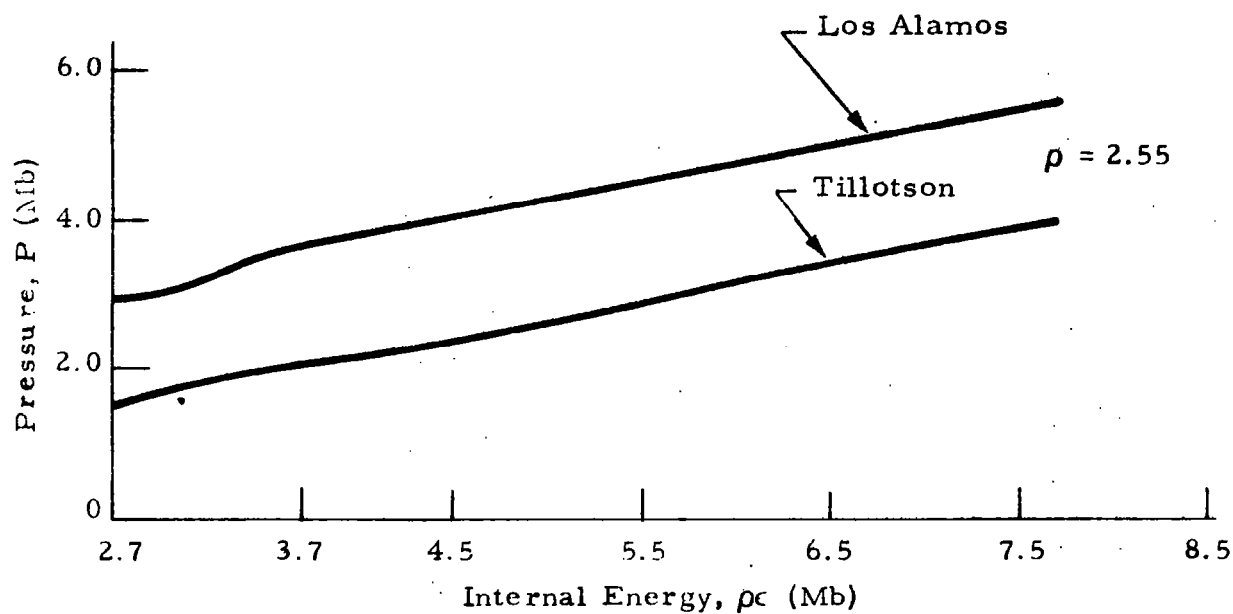


Fig. 6-15 - Variation of Pressure with Internal Energy (Aluminum $\rho_0 = 2.702 \text{ gm/cm}^3, \rho\epsilon = 2.7 \text{ to } 7.5 \text{ Mb}$)

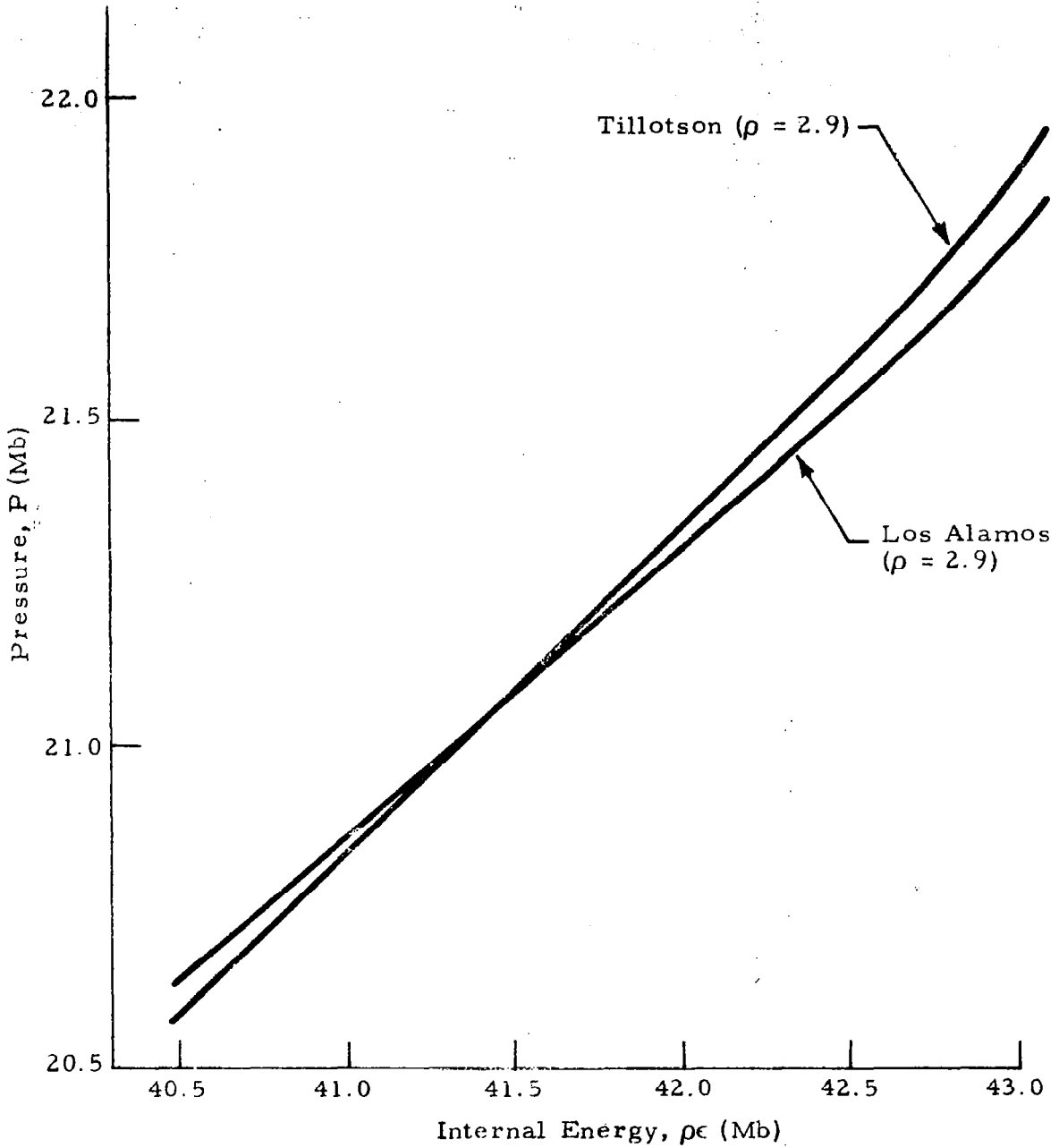


Fig. 6-16 - Variation of Pressure with Internal Energy (Aluminum, $\rho_0 = 2.702 \text{ gm/cm}^3$, $\rho\epsilon = 40.5$ to 43 Mb)

consideration is that an infinite plate traveling at a specified speed, v_0 , hits normally on another infinite plate at rest, as depicted in Fig. 6-17a. The two plates are 30 cm thick, and composed of the same aluminum material with initial density $\rho_0 = 2.77 \text{ gm/cm}^3$. The impact velocity is chosen to be $v_0 = 0.008 \text{ cm}/\mu\text{sec}$ for which a solution in elastic range of impact is available for comparison [40].

The problem was solved by the three-dimensional models described in Sections 4 and 5. The mesh and nodal numbering are generated by subroutine MESH and depicted in Fig. 6-17b. The Rankine-Hugoniot pressure, P_s , is readily obtained, using the Los Alamos equation of state,

$$P_s = 5.99868 \times 10^{-3} \text{ megabar} \quad (6.18)$$

The following numerical computations are performed based on inviscid assumption together with the Los Alamos equation of state.

Solution Computed by Methods of Weighted Residual: It is found from the numerical solution of (6.10) that the Galerkin approach does not perform satisfactorily. Although the scheme appears to be stable up to the time computed, there is a sign that the pressure development in the material tends to grow indefinitely. This phenomenon becomes more severe when the impact velocity is increased. Spurious oscillations with fairly large amplitudes always gather near the wave front, and the peak pressure is seen to exceed the Hugoniot pressure by about 50% to 100% as the velocity v_0 increases from 0.008 to 0.75 cm/ μsec . As remedies to the instabilities, some modifications such as incorporating the mid-point Runge-Kutta scheme into the code, as well as other methods of weighted residuals such as the least squares approach are introduced. Figure 6-18 shows the time history of pressure at interface computed by the method of least squares. The results computed by a modified Galerkin approach using mid-point Runge-Kutta scheme are found to be almost identical to those shown in Fig. 6-18. There is some improvement on the development

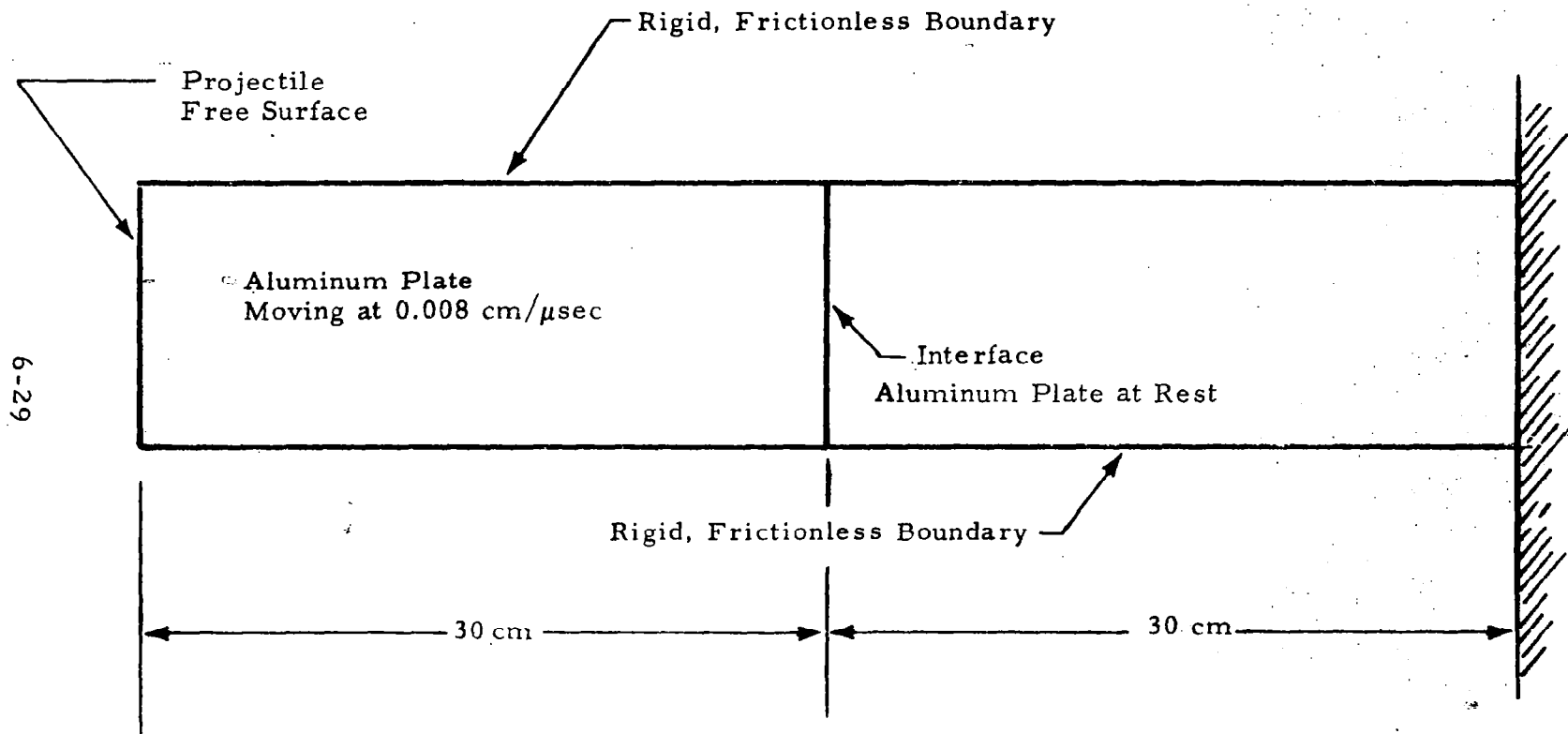


Fig. 6-17a - Configuration of Plates at Time of Impact

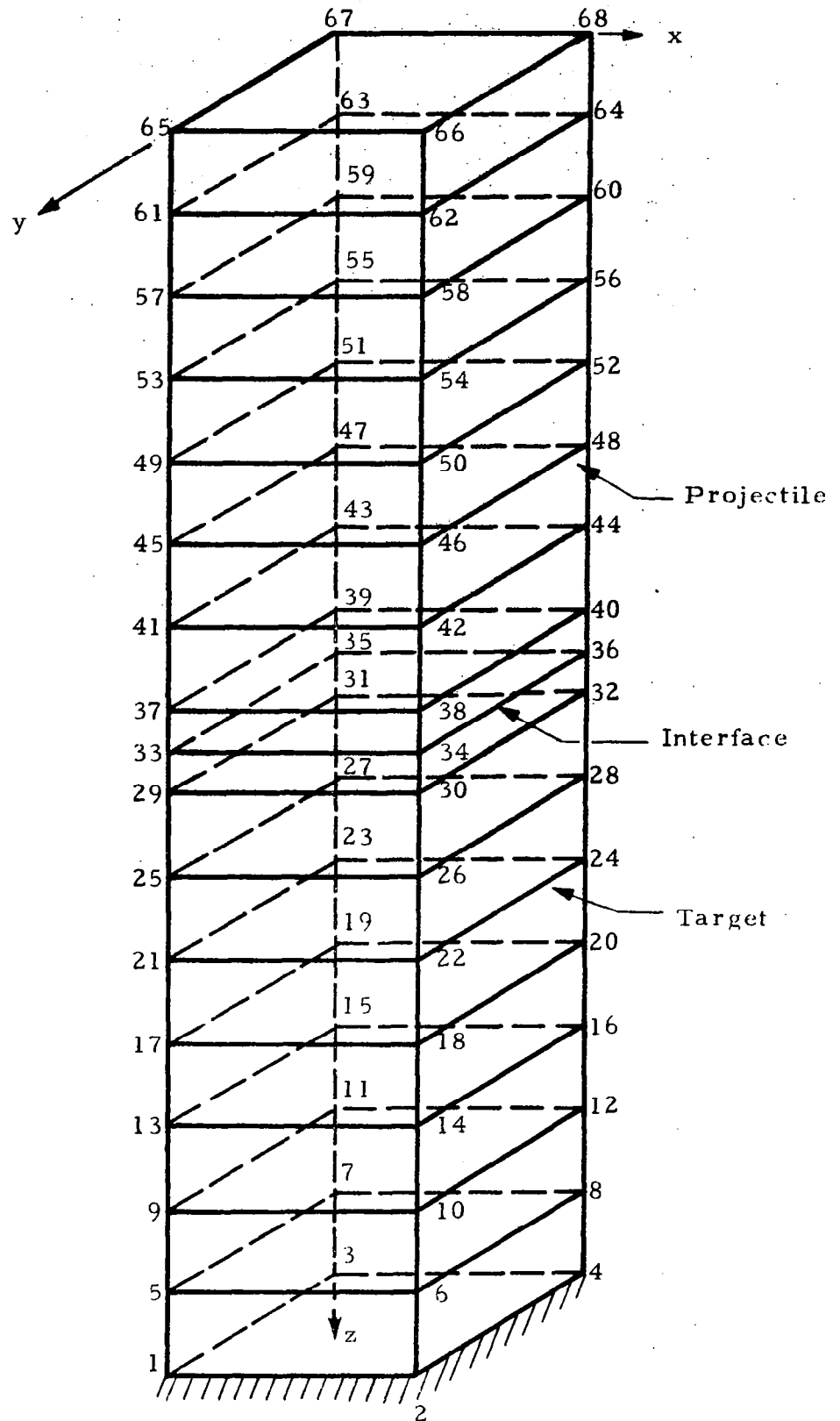


Fig. 6-17b — Numbering of Nodes in the Finite Element Representation (16 Linear Elements)

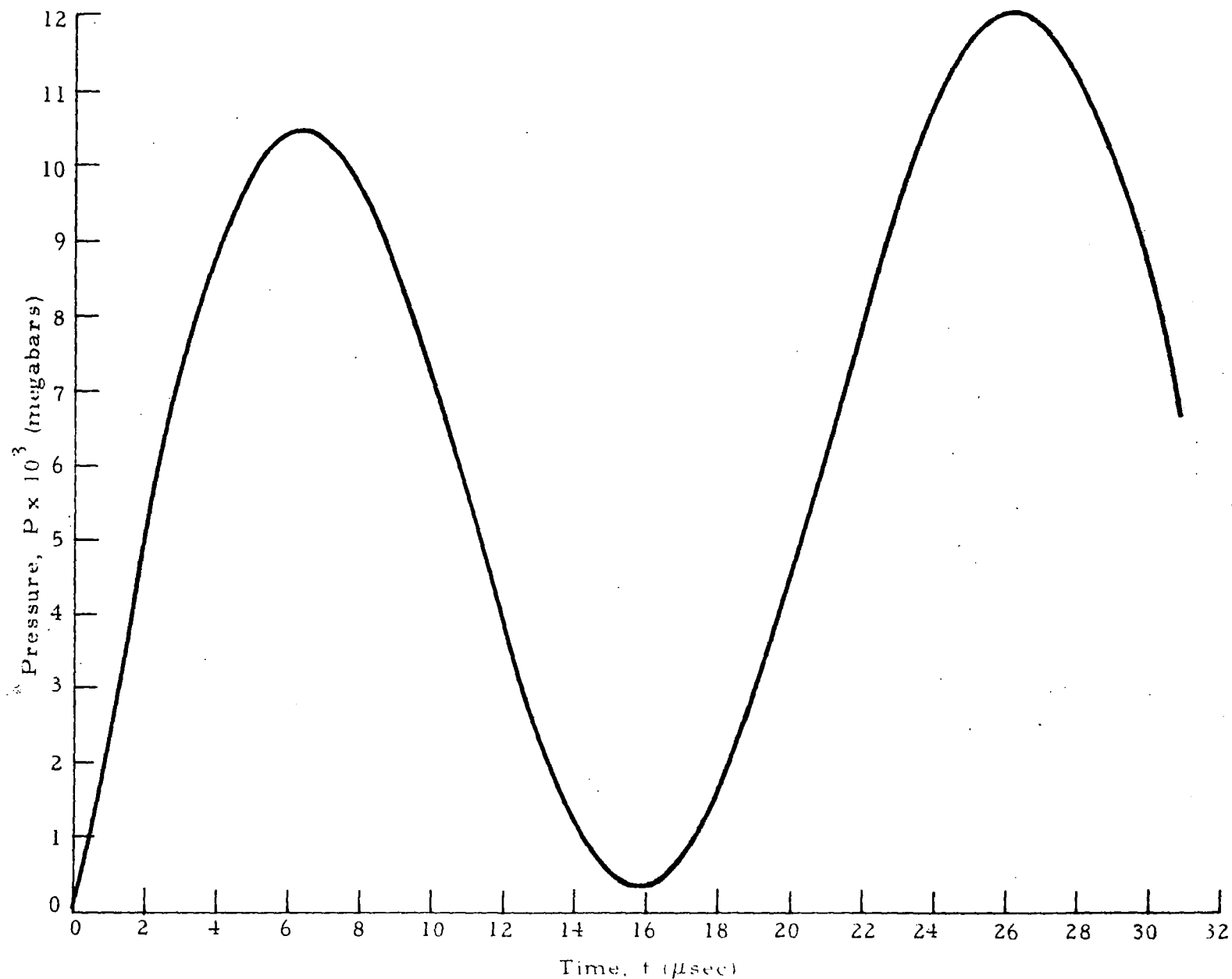


Fig. 6-18 - Time History of Pressure at Interface for 1-D Impact Problem Using Least Squares Scheme with 16 Linear Elements ($v_0 = 0.008 \text{ cm}/\mu\text{sec}$, $\rho_0 = 2.77 \text{ gm cm}^{-3}$)

history of the pressure field. However, the pressure at the interface still shows a tendency to diverge as time increases. The numerical instabilities can also be detected by the spurious oscillations near the shock fronts as shown in Fig. 6-19.

Solution Computed by Weak Solution Formulation: The pressure history at the interface computed using (5.15) and (5.16) with $a = 1/2$ is depicted in Fig. 6-20, and the corresponding pressure distributions at various times are shown in Fig. 6-21. It is seen that the results are improving compared to the ones computed by methods of weighted residuals as depicted in Figs. 6-18 and 6-19. The solution may be improved even further when the parameter a in (5.15) is increased. Figures 6-22 and 6-23 show the pressure history at the interface using $a = 2$, and 4, respectively. The corresponding pressure distributions are plotted in Figs. 6-24 and 6-25.

All results discussed so far and depicted in Figs. 6-18 through 6-25 are computed using 16 linear elements. As shown in Figs. 6-21, 6-24 and 6-25, the overshoot due to the numerical instability decreases rapidly, and the zig-zag behavior near the wave front becomes less severe as the parameter a increases. These facts indicate that the numerical dissipation introduced in the scheme is proportional to the parameter a .

The plots also show some substantial differences in amplitudes of the pressure waves among different a and α values. In addition, as shown in Figs. 6-22 and 6-23, the numerical dissipation increases as α decreases, and the phase lag becomes more apparent at the same time. These imply that various errors may enter in the computations if the scheme is over-dissipated. The sensitivity of the solutions upon the factor α , however, can be made inert by refining the mesh as shown in Figs. 6-26 through 6-29 where 30 even spaced linear elements were used in the computations. In this case, the same time step size as employed in the 16-element case was used. This verifies the statement mentioned in Section 5.3, namely, the factor α is indeed related directly to the ratio of the time step size and the element size. As the

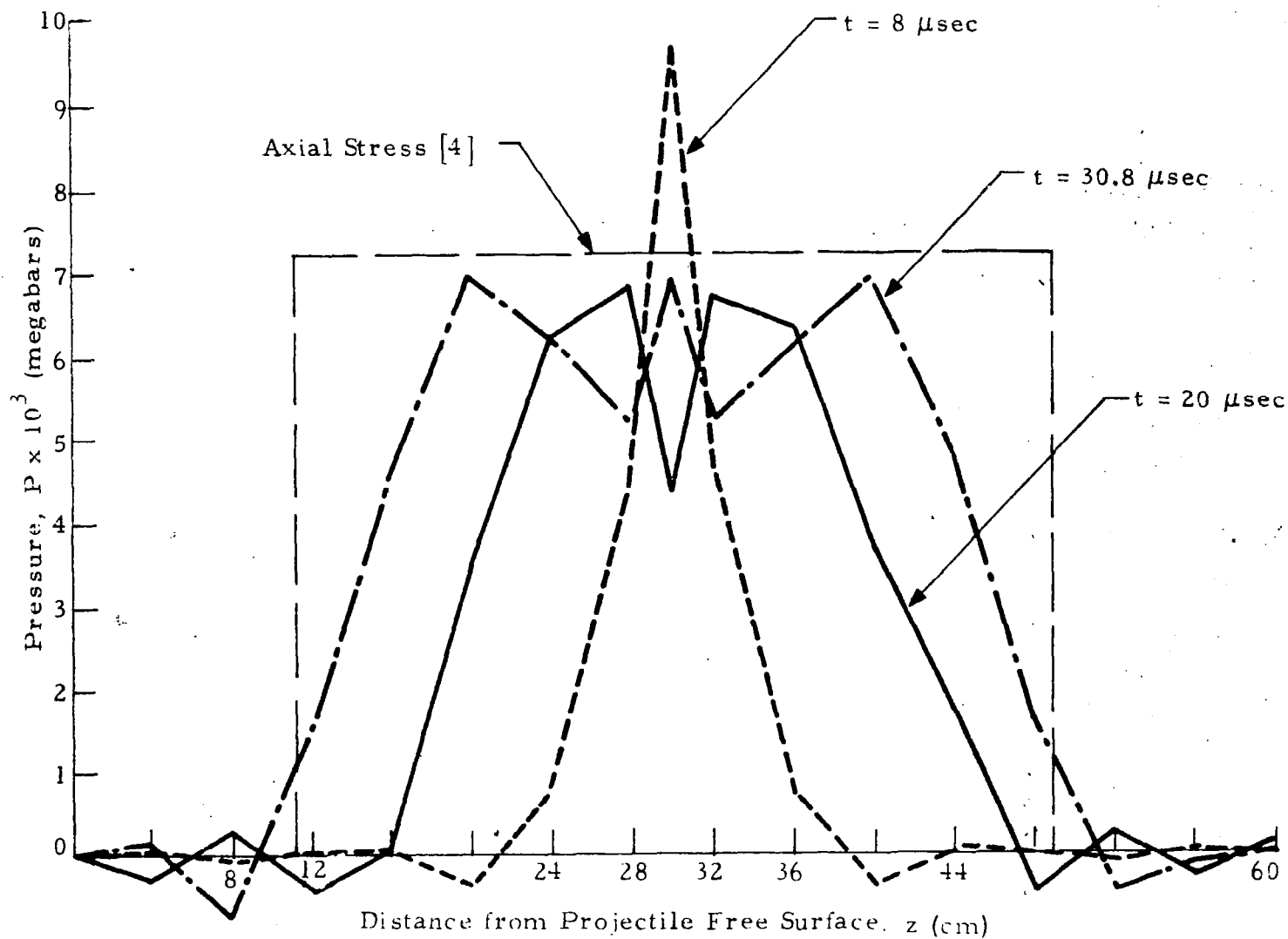


Fig. 6-19 - Pressure Distributions at Various Time for 1-D Impact Problem
 Using Least Squares Scheme with 16 Linear Elements ($v_0 = 0.008$ cm/
 μsec , $\rho_0 = 2.77$ gm/cm³)

6-34

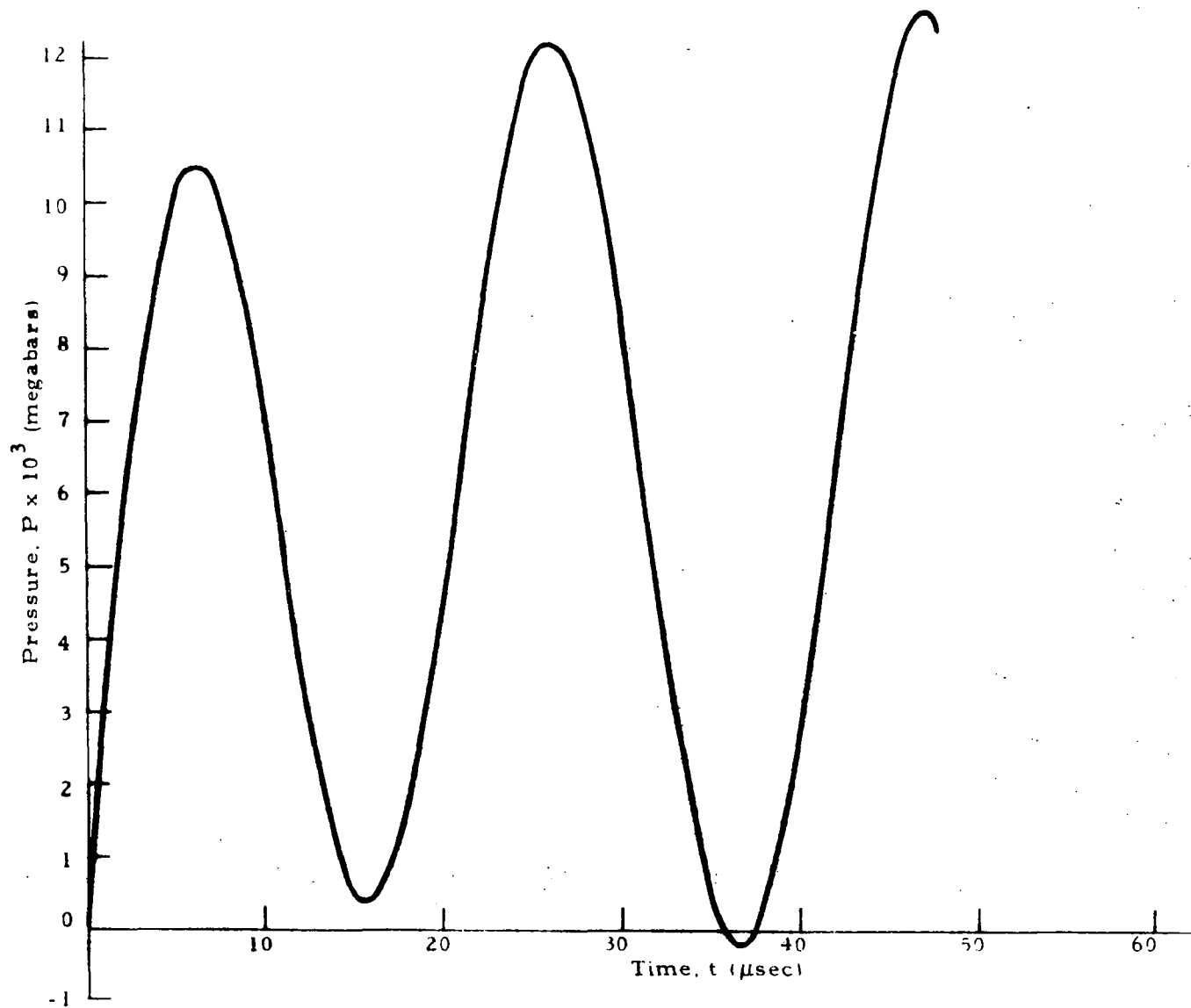


Fig. 6-20 - Pressure Development at the Intensity Interface with 16 Linear Elements ($a = 0.5$, $\alpha = 0.0$)

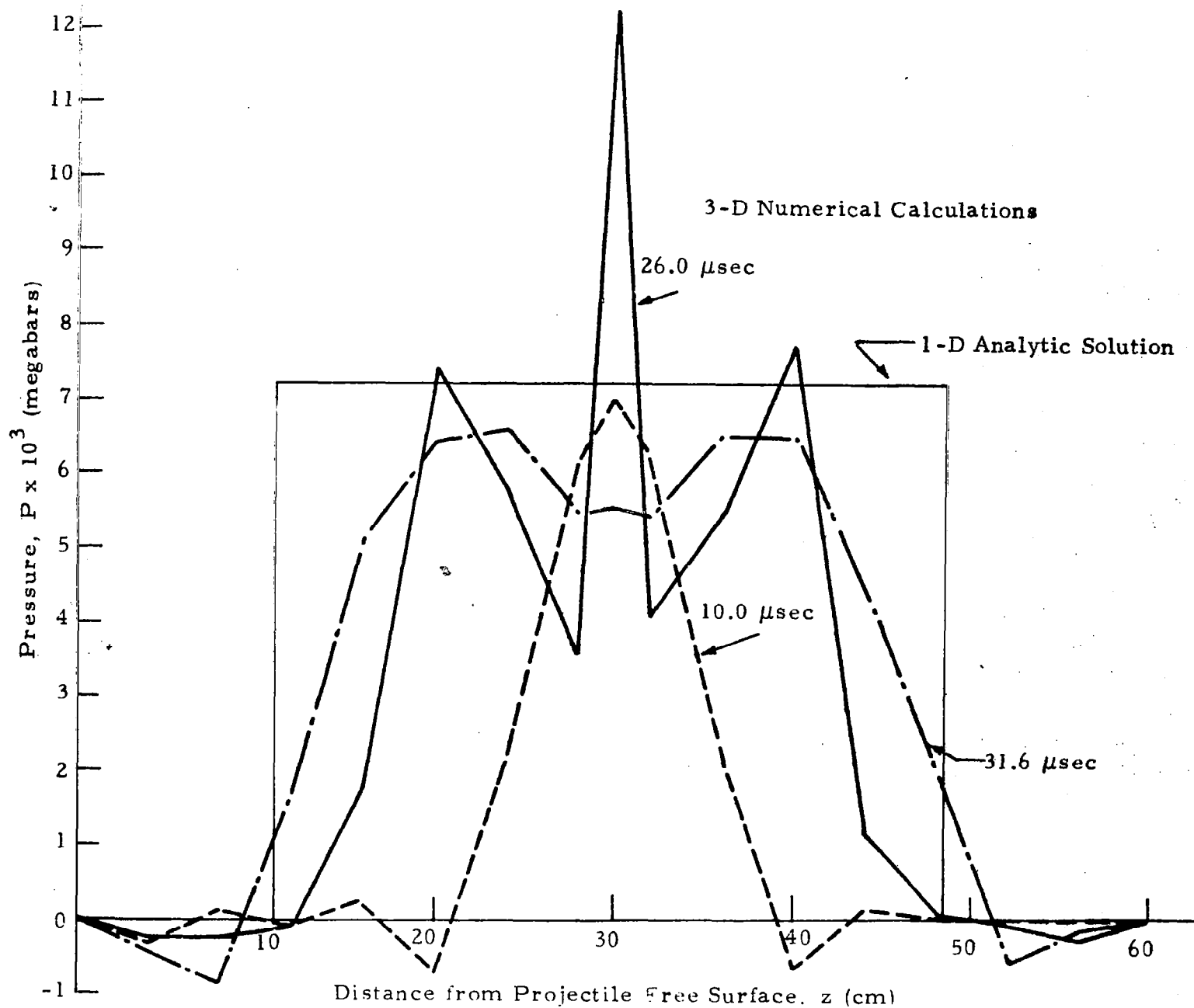


Fig. 6-21 - Pressure Distributions at Various Times
with 16 Linear Elements ($a = 0.5$, $\alpha = 0.0$)

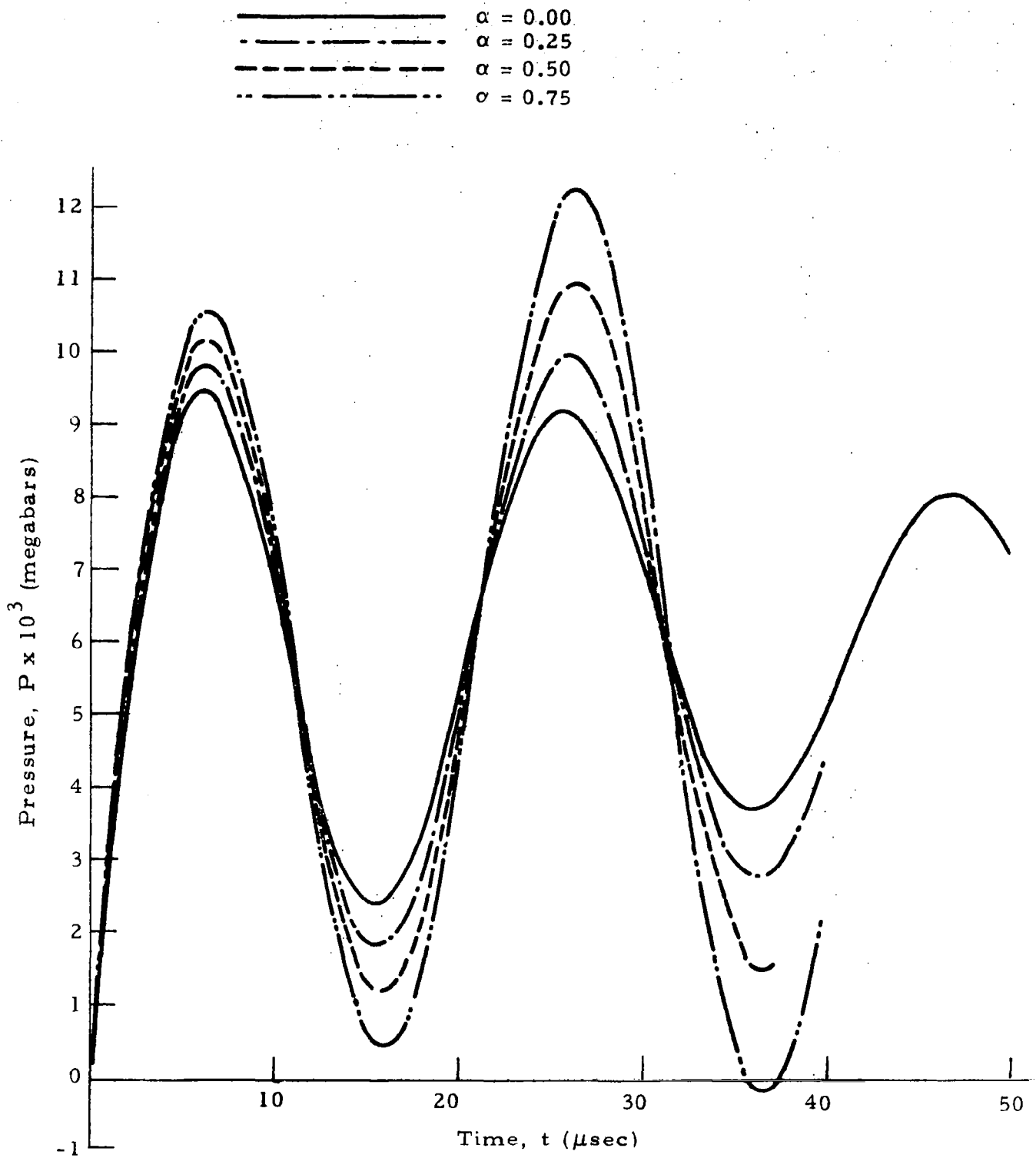


Fig. 6-22 - Pressure Development at the Interface
with 16 Linear Elements ($a = 2.0$)

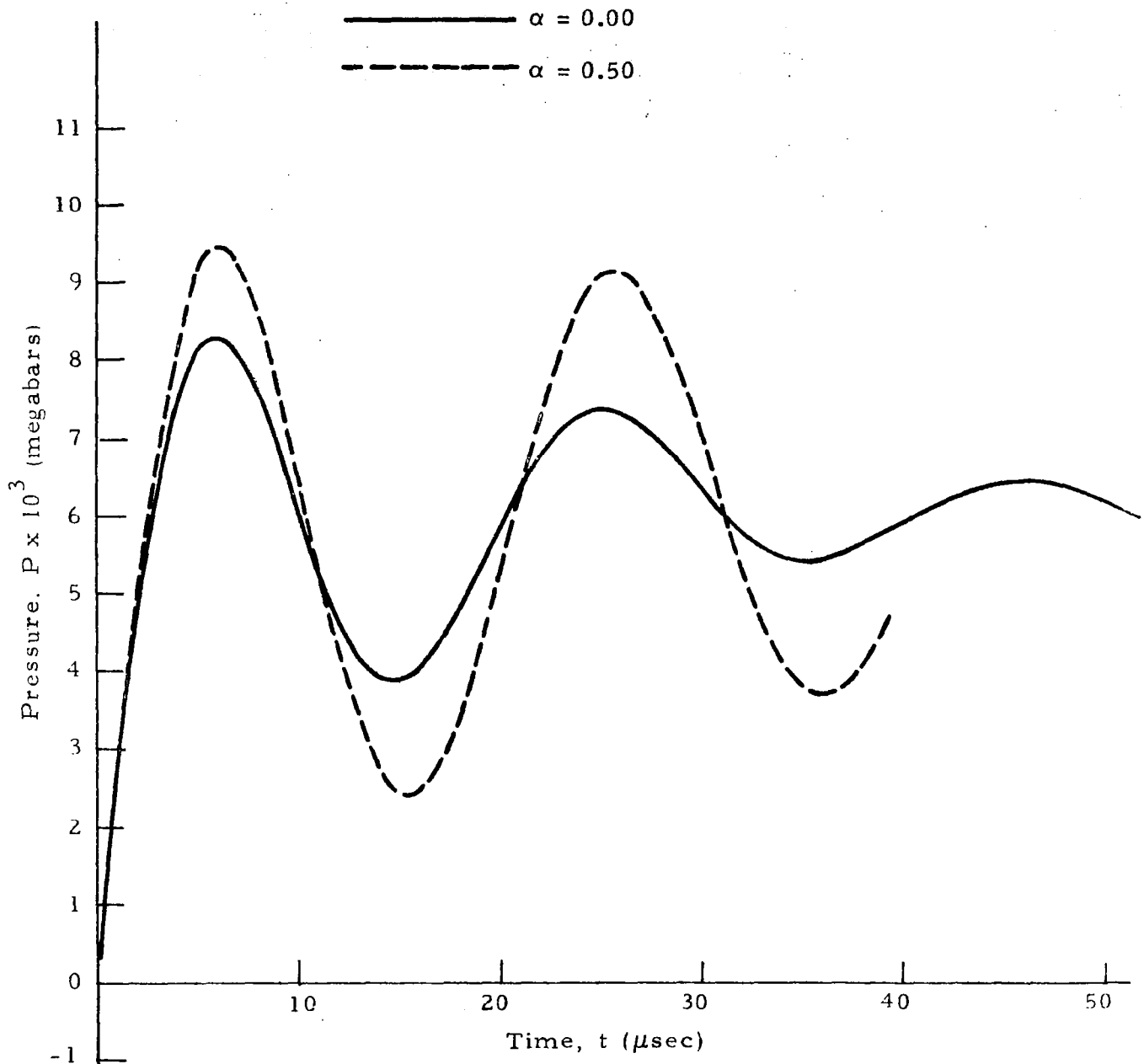
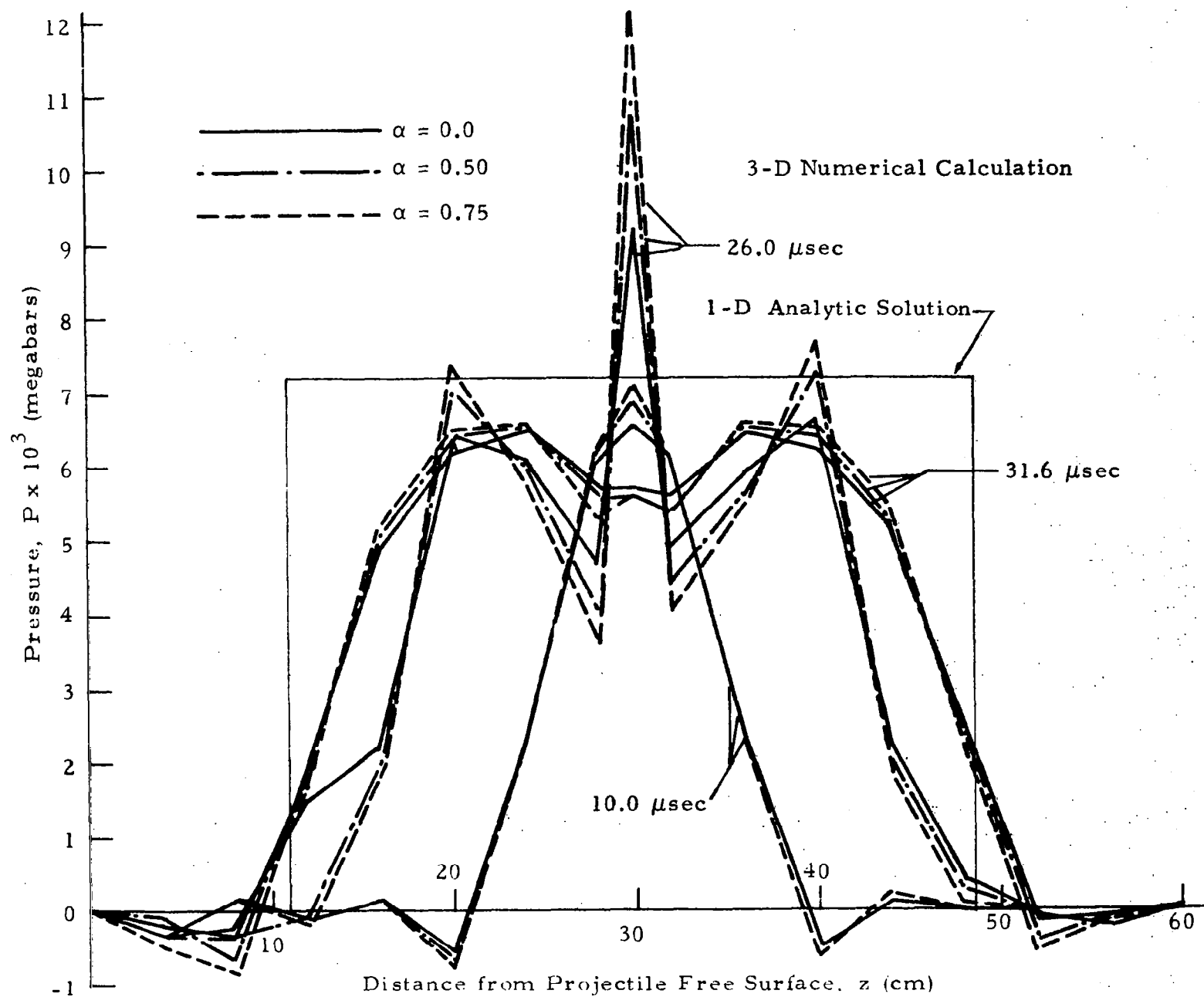


Fig. 6-23 - Pressure Development at the Interface
with 16 Linear Elements ($a = 4.0$)



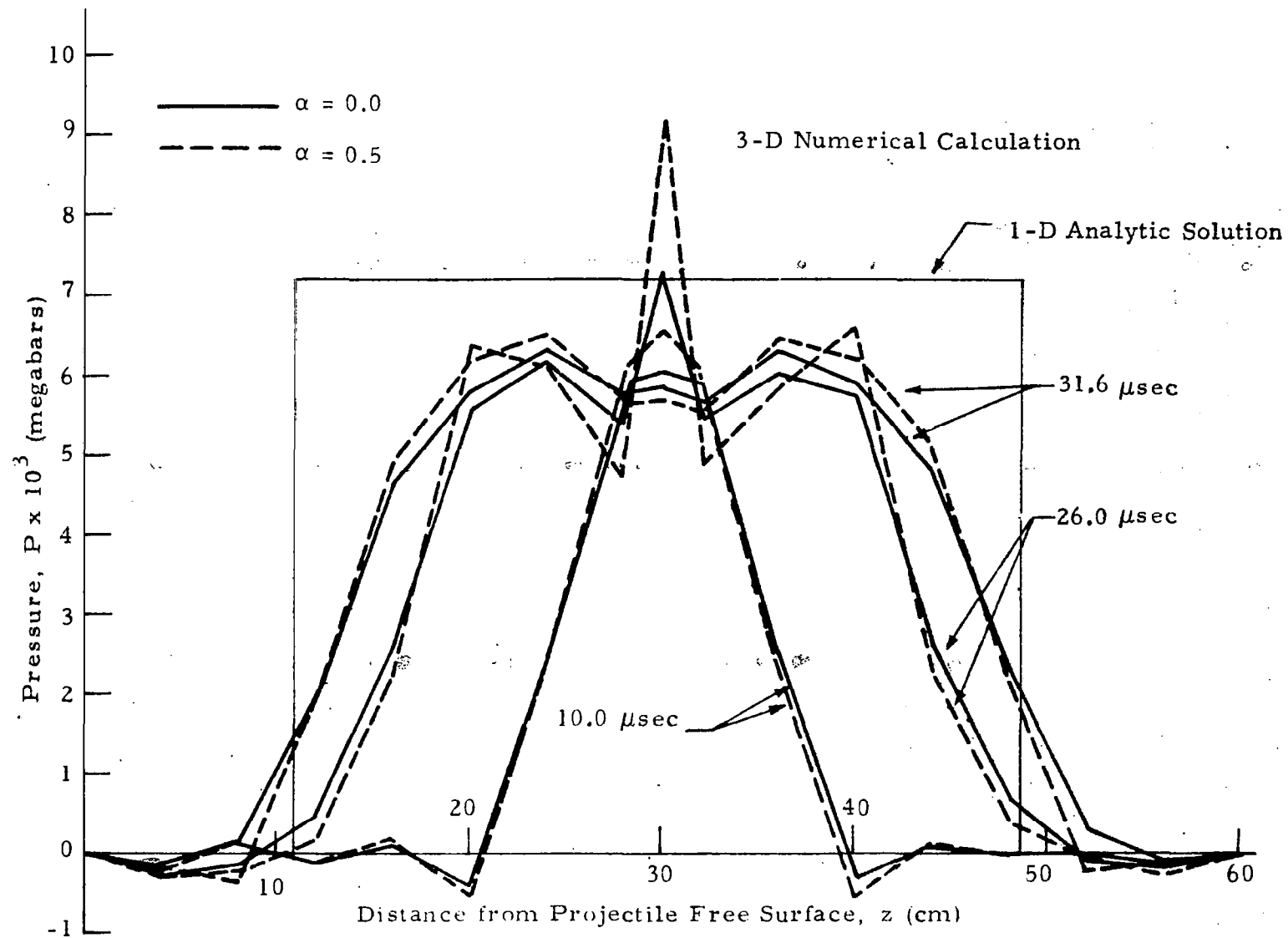


Fig. 6-25 - Pressure Distributions at Various Times
with 16 Linear Elements ($a = 4.0$)

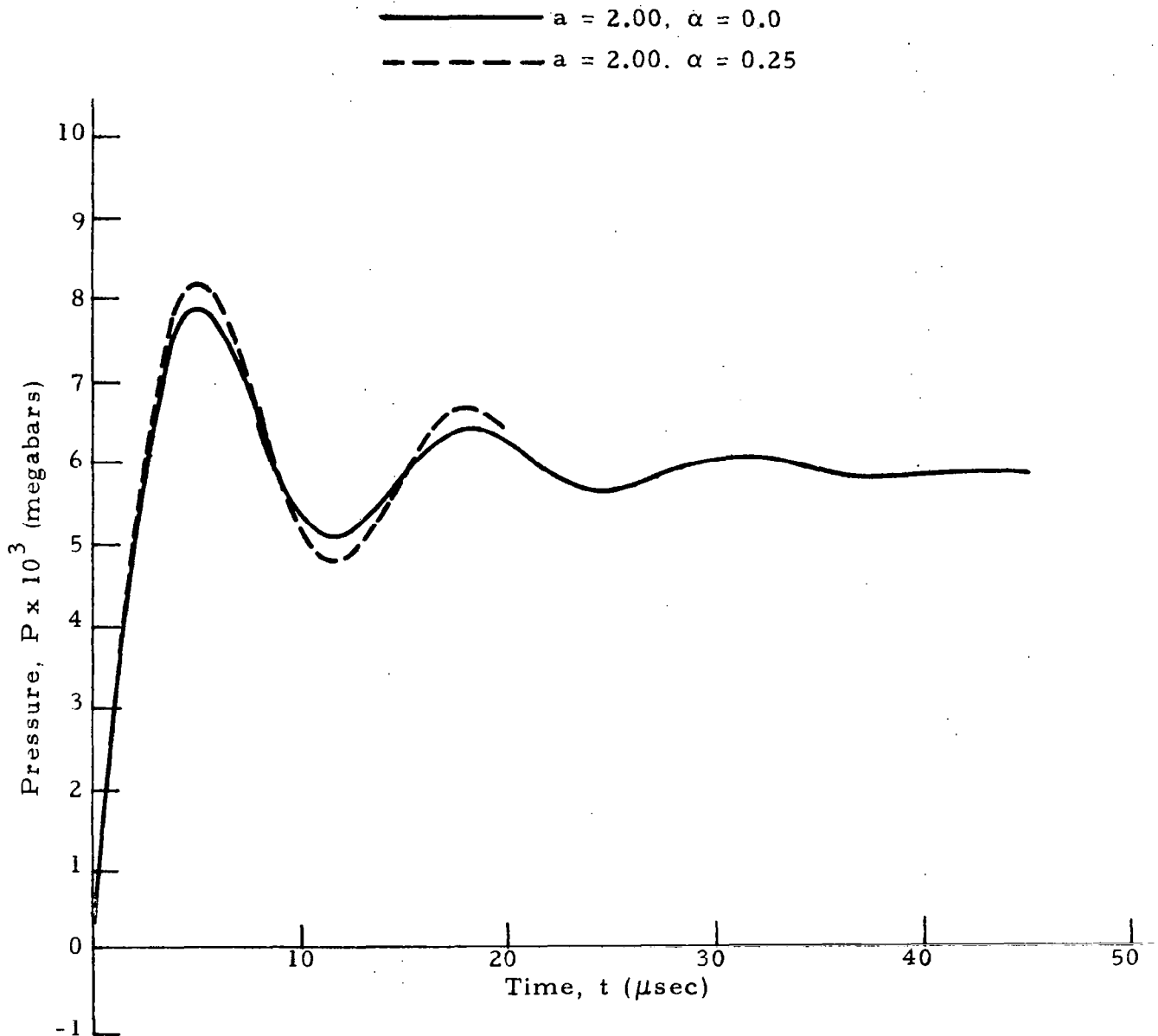


Fig. 6-26 - Pressure Development at the Interface Using 30 Linear Elements ($a = 2.0, \alpha = 0.0$ and 0.25)

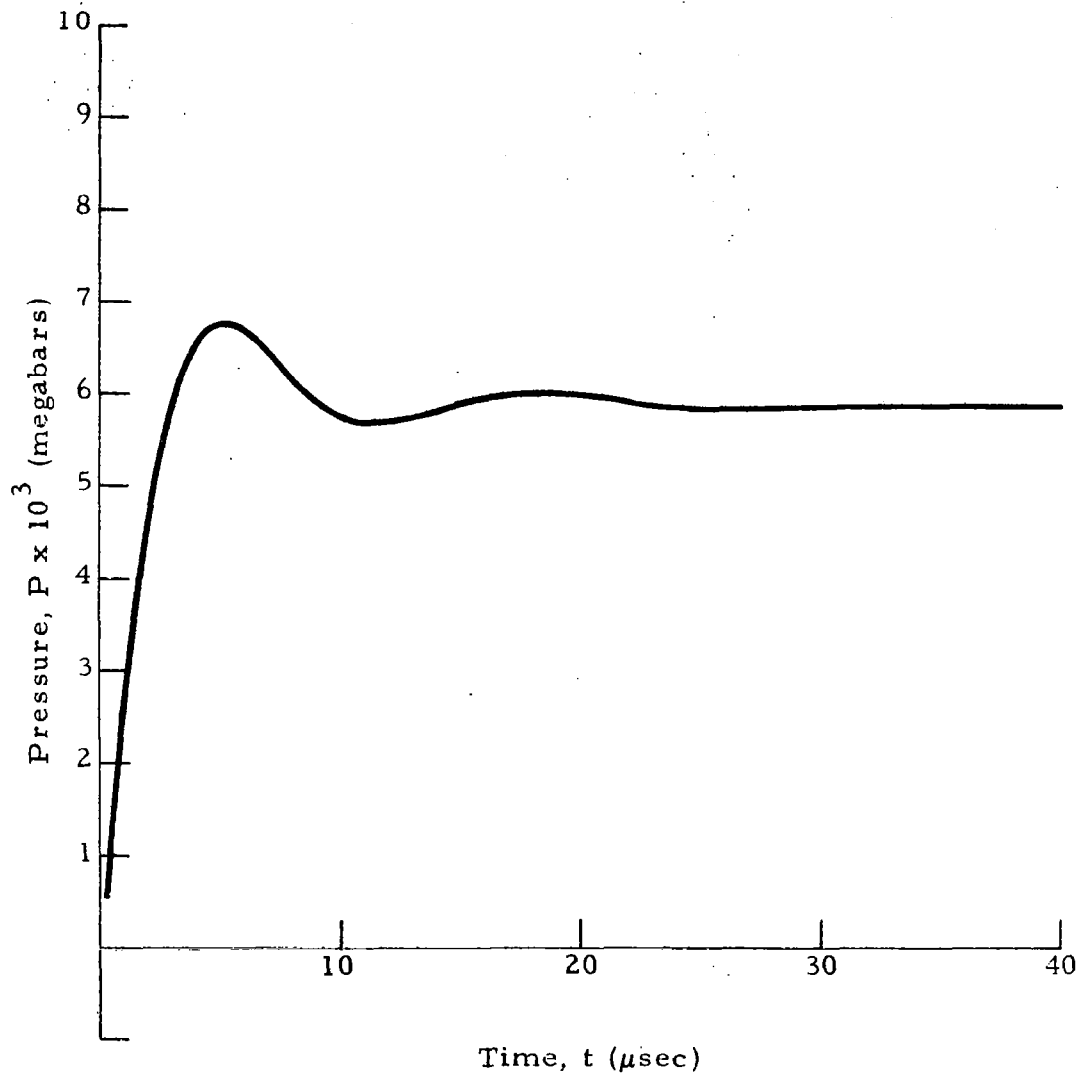


Fig. 6-27 - Pressure Development at the Interface Using 30 Linear Elements ($a = 4.0$, $\alpha = 0.0$)

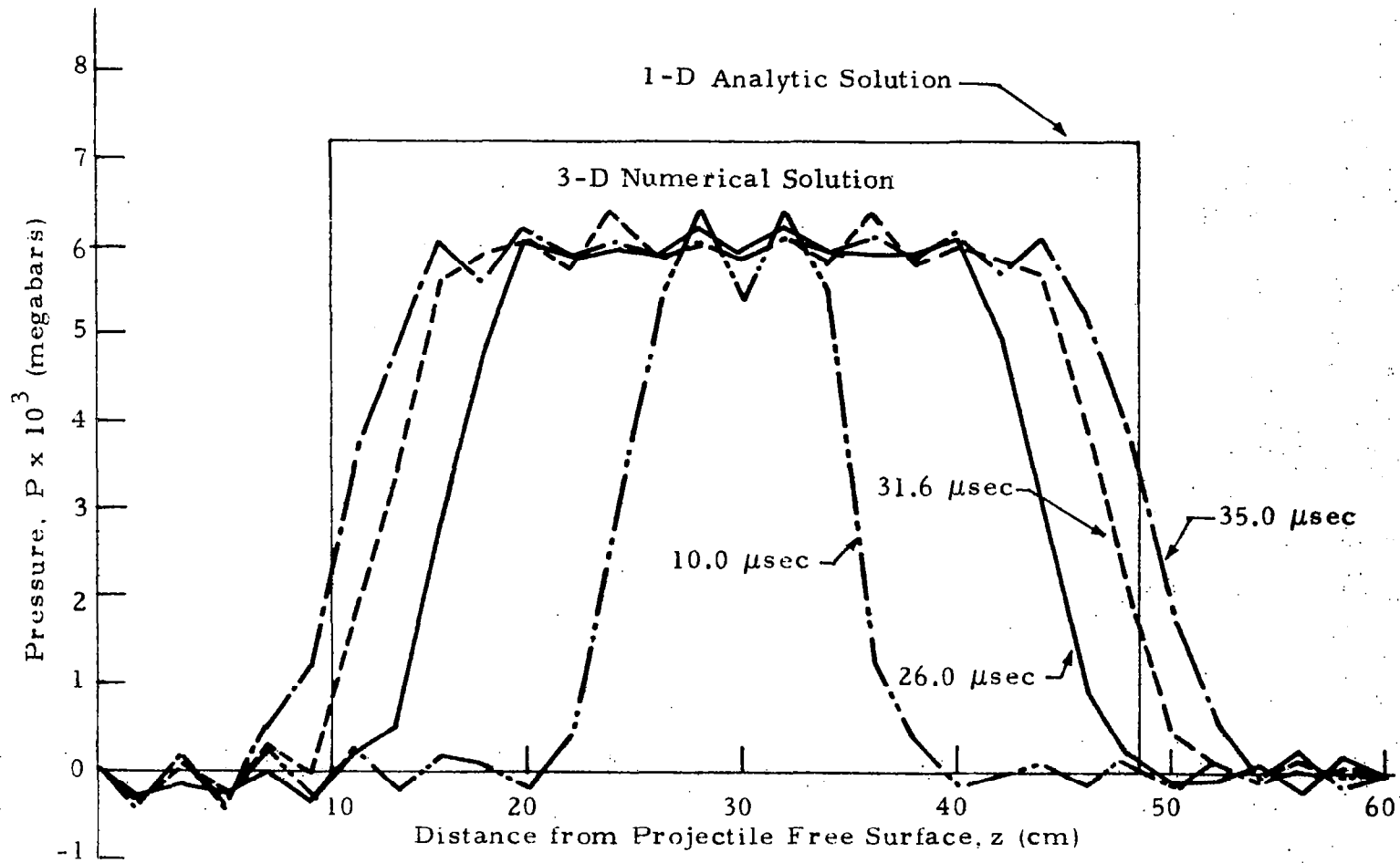


Fig. 6-28 - Pressure Distributions at Various Times Using 30 Linear Elements ($a = 2.0$, $\alpha = 0.0$)

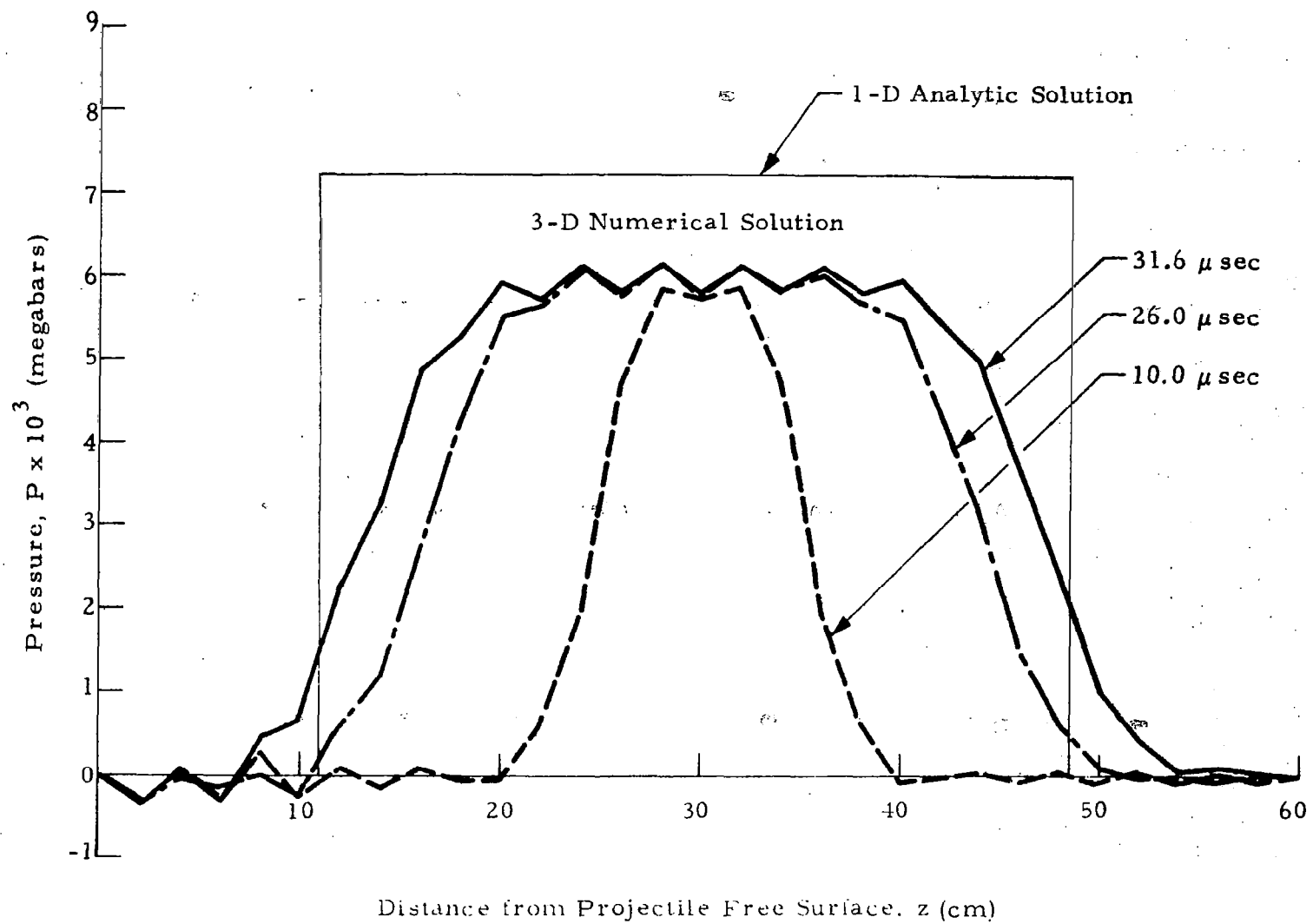


Fig. 6-29 — Pressure Distributions at Various Time Using 30 Linear Elements ($a = 4.0$, $\alpha = 0.0$)

mesh size reduced, the effect of α on the accuracy of the solution becomes less important. The results using 16 quadratic elements also show the same trend. In Figs. 6-30 and 6-31, the pressure history at the interface is depicted using $a = 2.0$ and $a = 4.0$, respectively, with different α . As expected, these results are improved compared to the cases with 16 linear elements, but are less smooth when compared with that using 30 linear elements. Similar comparisons can also be made for the pressure distributions (see, e.g., Figs. 6-24, 6-25 for 16 linear elements, Figs. 6-28, 6-29 for 30 linear elements, and Figs. 6-32, 6-33 for 16 quadratic elements).

As is seen, all the cases seem to underpredict the peak pressure compared to the analytic solution. However, with the same given conditions and Los Alamos equation of state, the pressure computed by Rankine-Hugoniot relations is $P_s = 5.99868 \times 10^{-3}$ megabar. This value is approximately equal to the average value as shown in Figs. 6-28 and 6-29 which indicates that our numerical results are quite reasonable. Accordingly, P_s should be the upper bound for the average pressure distribution in the material under high velocity impact, since the physical as well as numerical dissipative effects may actually reduce the pressure buildup in the material. Therefore, it is believed that the deviation of the analytic solution from the computed Rankine-Hugoniot pressure and from our results could be due to one of the following:

- The assumptions made in the theoretical analysis lead to a too simplified model, so that the analytic solution was overestimated,
- There are possible misprints related to the given conditions in the report we obtained, and
- The analytic pressure distribution, $P_s = 7.22 \times 10^{-3}$ was normalized by the impact velocity, $V_0 = 0.008$ cm/ μ sec, but was not mentioned in the report.

These possibilities hopefully can be cleared up as soon as we locate the original report.

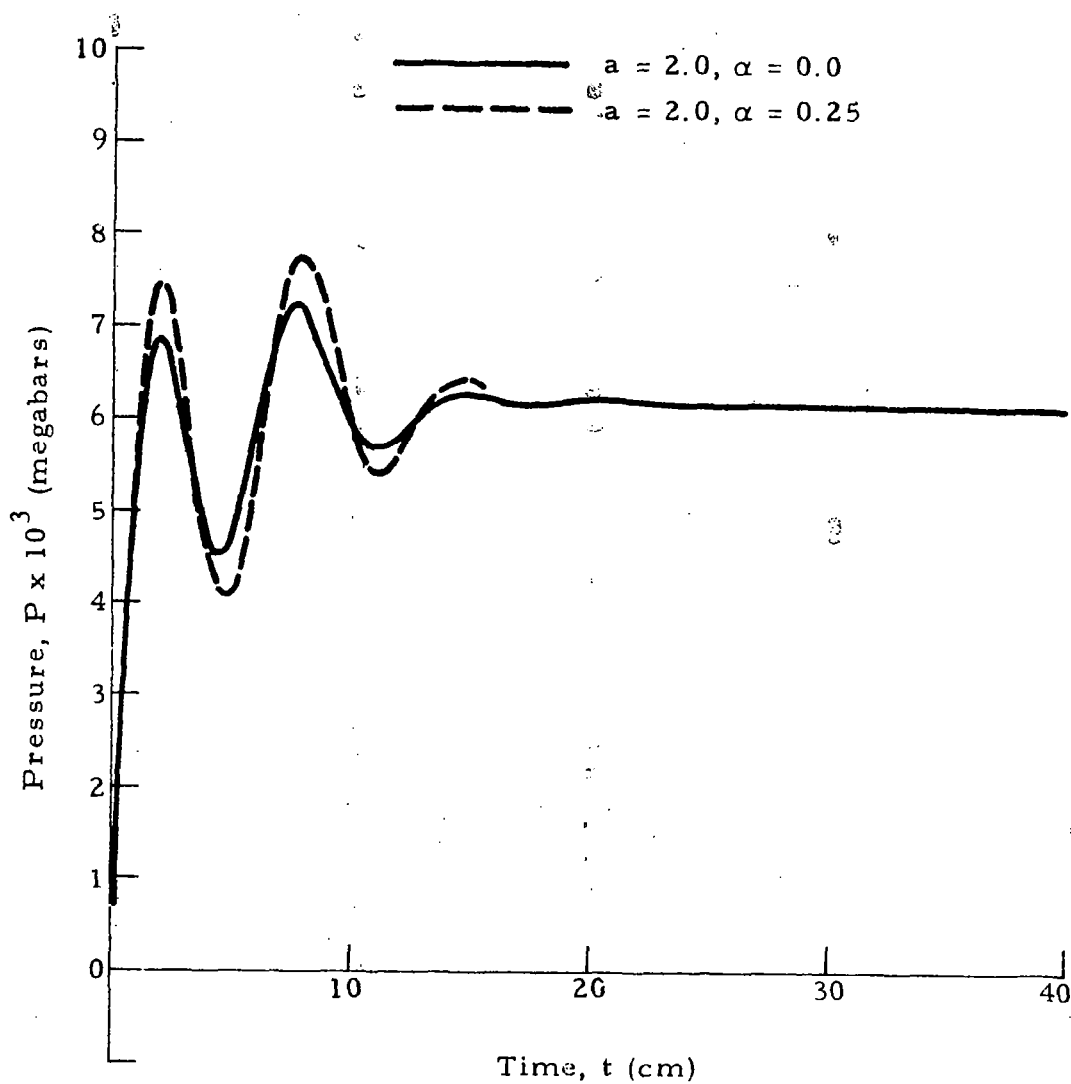


Fig. 6-30 — Pressure Development at the Interface
Using 16 Quadratic Elements
($a = 2.0, \alpha = 0.0$ and 0.25)

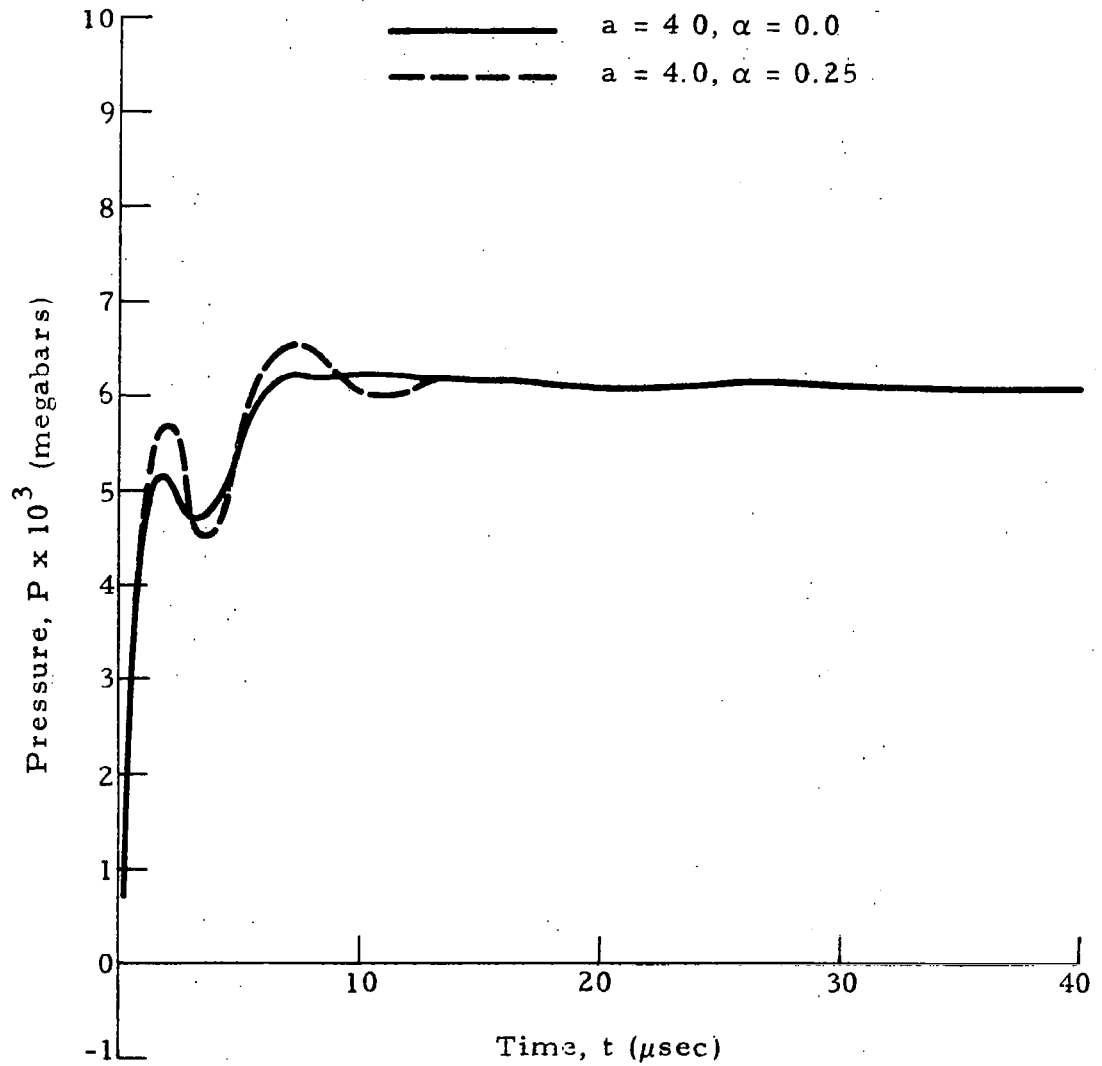


Fig. 6-31 - Pressure Development at the Interface
Using 16 Quadratic Elements
($a = 4.0, \alpha = 0.0$ and 0.25)

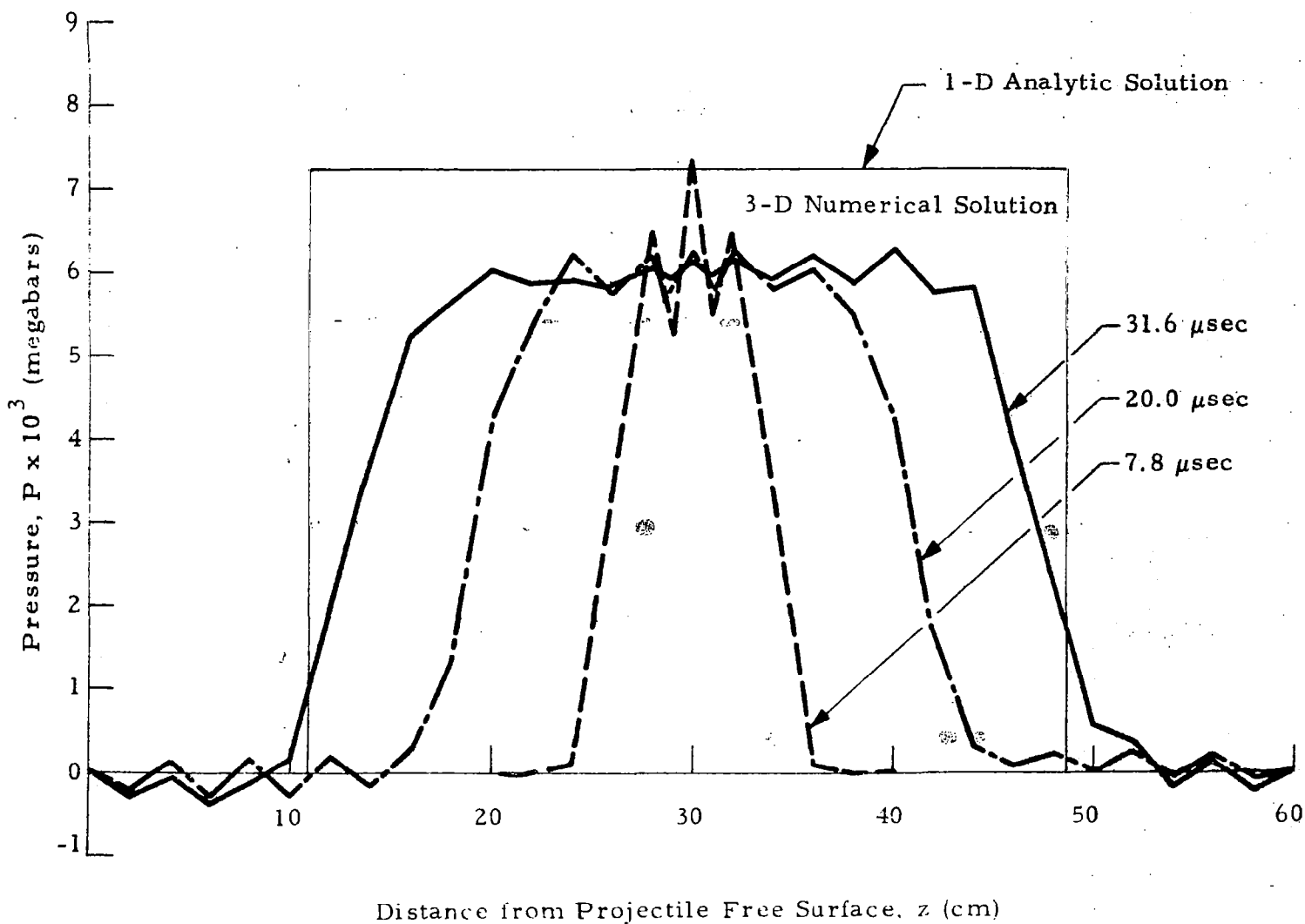


Fig. 6-32 - Pressure Distributions at Various Times Using 16 Quadratic Elements
($a = 2.0$, $\alpha = 0.0$)

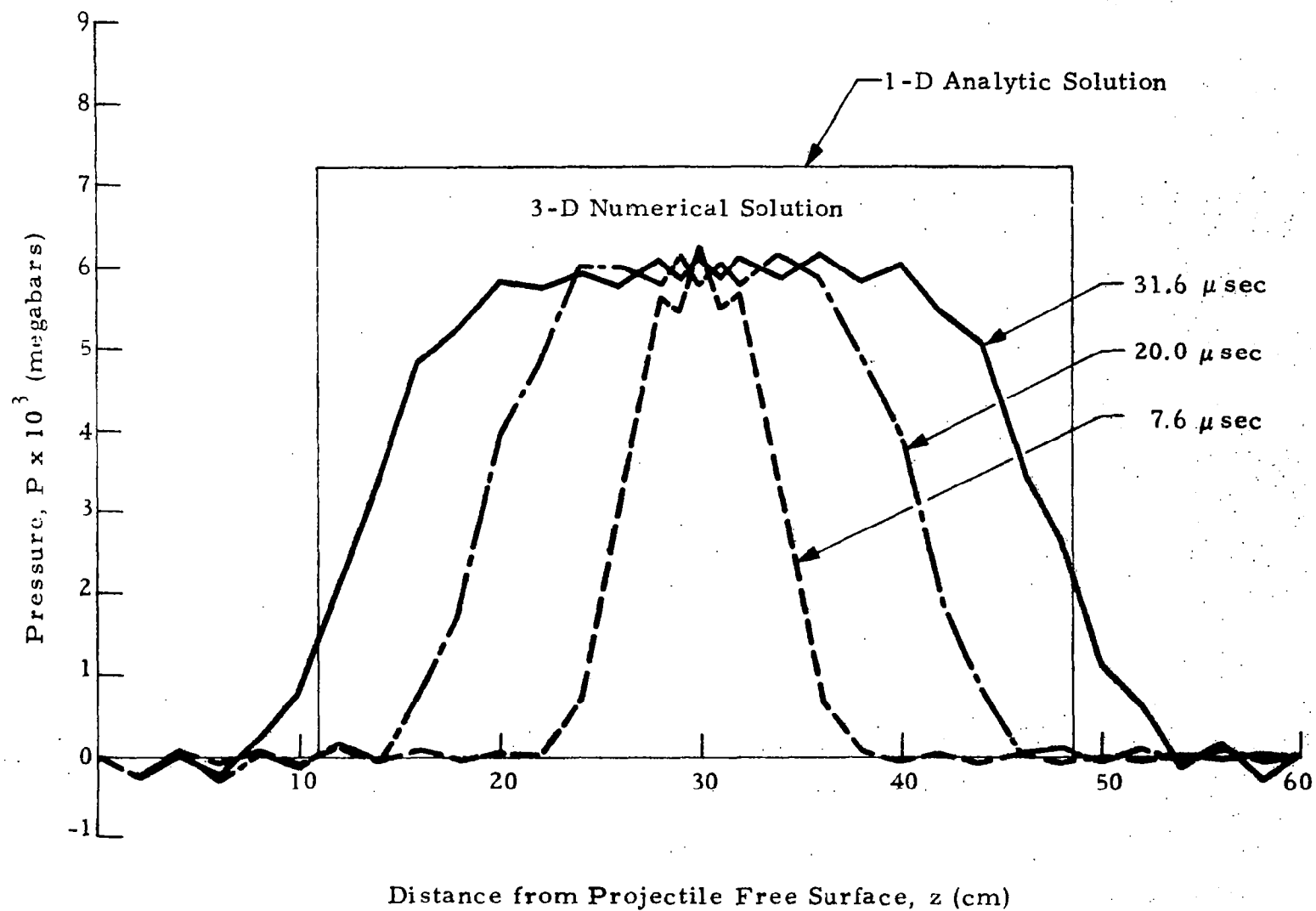


Fig. 6-33 - Pressure Distributions at Various Times Using 16 Quadratic Elements

The speed of sound in a material can be obtained in the relation

$$C_s^2 = \left(\frac{\partial P}{\partial \rho} \right)_s \quad (6.9)$$

Following the Gibb's equation, one has

$$C_s^2 = \frac{P}{\rho} \frac{\partial P}{\partial \epsilon} + \frac{\partial P}{\partial \rho} \quad (6.10)$$

where ϵ is the specific internal energy which is now being considered as a function of total specific energy and the particle velocity. Thus the propagation speed of the pressure waves can be computed by substituting the nodal solution of the conservation equations and equation of state on the element containing the wave front into (6.10). The numerical values of C_s in the target obtained using Los Alamos equation of state at some typical times are shown in Table 6-1. It is seen that the values oscillate around the shock speed computed by Rankine-Hugoniot relation, i.e., $C_{s_{R-H}} = .53569 \text{ cm}/\mu\text{sec}$. In elasto-dynamic theory, on the other hand, the sound speed is represented by

$$C_{s_{El.}} = \sqrt{\frac{(1 - \nu)E}{(1 + \nu)(1 - 2\nu)\rho}} \quad (6.11)$$

where ν is the Poisson ratio, E is the Young's modulus. With $\nu = 0.33$, $E = 10^7 \text{ psi}$ for aluminum, Eq. (6.11) gives $C_{s_{El.}} = 0.60729 \text{ cm}/\mu\text{sec}$, which deviates from the values obtained by the present approach by about 10%. This implies that the compressibility effects play an important role in the dynamic response of materials under high velocity impact loads. In addition, although in the present hydrodynamic model the material is assumed to be inviscid, the dissipation resulting from the equation of state and numerical viscosity as well may affect the local speed of the pressure waves.

Table 6-1

PROPAGATION VELOCITY OF PRESSURE WAVES IN TARGET
AT VARIOUS TIMES AFTER IMPACT
(WITH 30 LINEAR ELEMENTS)

Poisson Ratio, $\nu = 0.33$; Young's Modulus, $E = 10^7$ psi;

Impact Velocity, $V_o = -0.008$ cm/ μ sec

Time, $t(\mu\text{sec})$	0	5.0	10.0	18.0	26.0	31.6	35.0
Shock Speed, C_s (cm/ μ sec)	.53442	.54123	.53846	.53880	.53679	.53801	.53782

Rankine-Hugoniot — $C_s = .53569$ cm/ μ sec

3-D Elastic Waves — $C_s = \sqrt{\frac{(1 - \nu)E}{(1 + \nu)(1 - 2\nu)\rho}} = .60729$ cm/ μ sec

Momentum and Energy Distributions: Momentum and total energy distributions at $t = 20$ and $30 \mu\text{sec}$ are depicted in Figs. 6-34 and 6-35 for 16 linear elements, Figs. 6-36 and 6-37 for 30 linear elements, and Figs. 6-38, 6-39 for 16 quadratic elements. In these plots, the parameter $a = 2.0$ are used. A better accuracy using 30 linear elements against 16 quadratic elements is obvious. In particular, as seen in the rarefaction region, the momentum and total energy distributions computed using 16 quadratic elements are severely distorted by the numerical instabilities. Hence, a larger parameter a is needed, although it is not so obvious from the plots of pressure distributions. Depicted in Figs. 6-40 through 6-42 are momentum and total energy distributions using various types of elements with $a = 4.0$, and as expected, better results are obtained.

6.2.4 Three-Dimensional Impact Problem

A simple problem of a 4 cm aluminum ($\rho_0 = 2.702 \text{ gm/cm}^3$) cube impacting at a velocity of $2.6 \text{ cm}/\mu\text{sec}$ on a semi-infinite cube (16 cm cube) was also tested. The numbering of nodes in the mesh is depicted in Fig. 6-43, with the corresponding boundary conditions given in Fig. 6-13.

For this problem, only preliminary results by the Galerkin procedures are available, which are shown in Figs. 6-44 and 6-45. Figure 6-44 shows the pressure variation with time at various nodes on the interface, while Fig. 6-45 depicts the pressure variation with distance into the target at various time. In the computations, Los Alamos equation of state was used and negative pressures at any node in the projectile-target configuration were not allowed. Nor was the movement of free surface accounted for at the time of computation. Like the one-dimensional problem, the Galerkin formulation again indicated some numerical instabilities which must be remedied.

Computations using the weak solution formulation is in progress, which will be discussed in the final report.

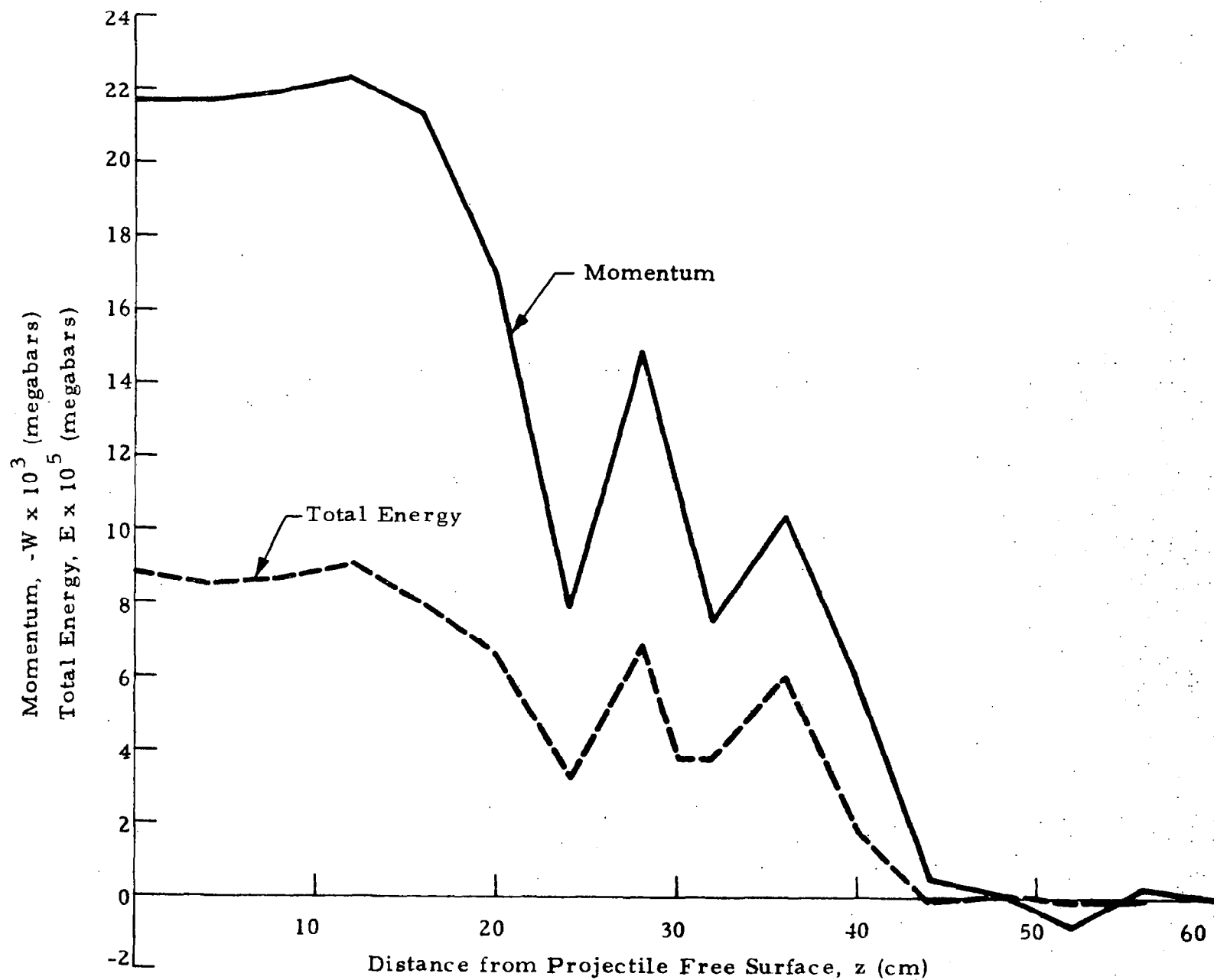


Fig. 6-34—Momentum and Total Energy Distributions at $t = 20.0 \mu\text{sec}$
 (16 Linear Elements; $\rho = 2.0$; $\mu = 0.0$)

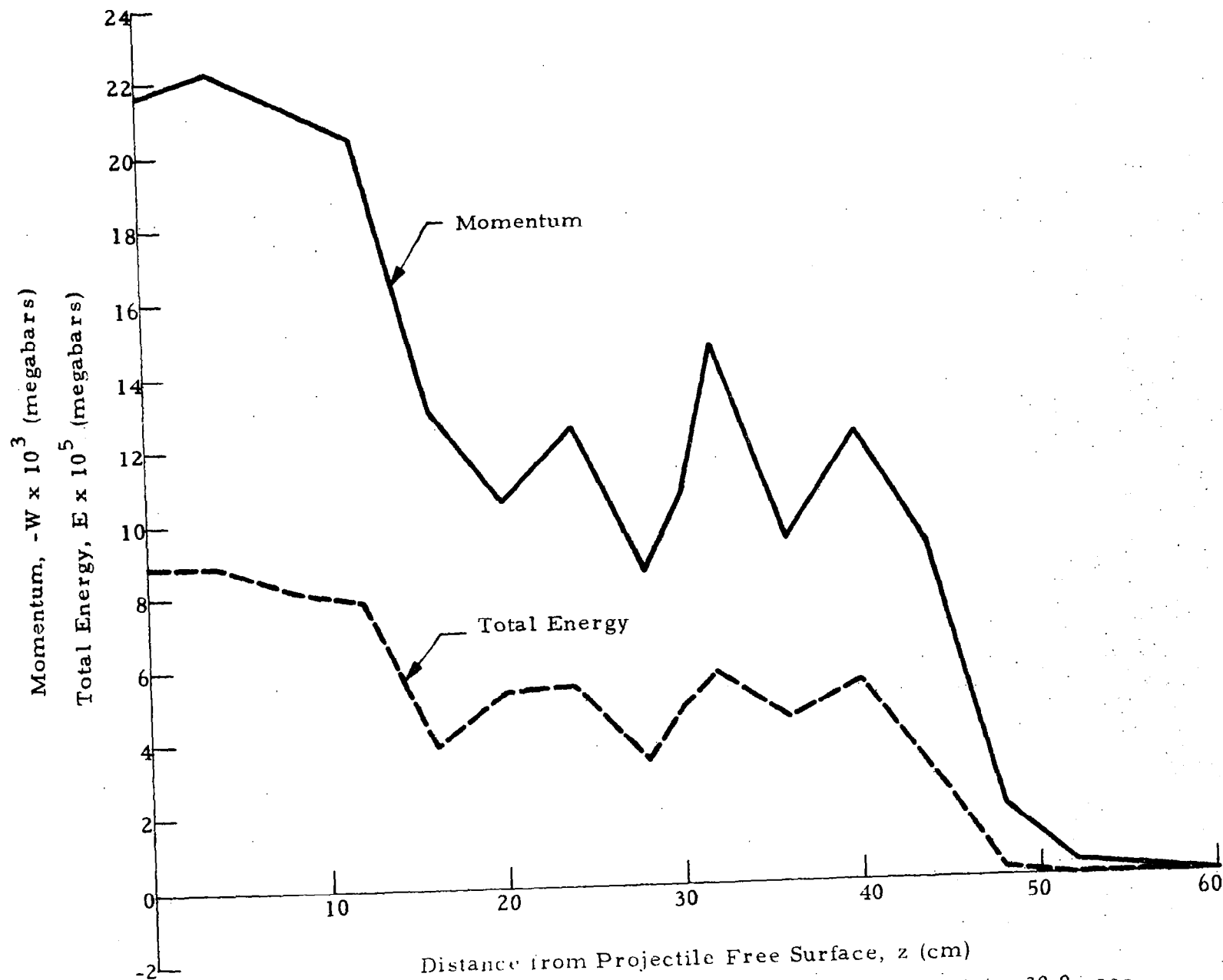
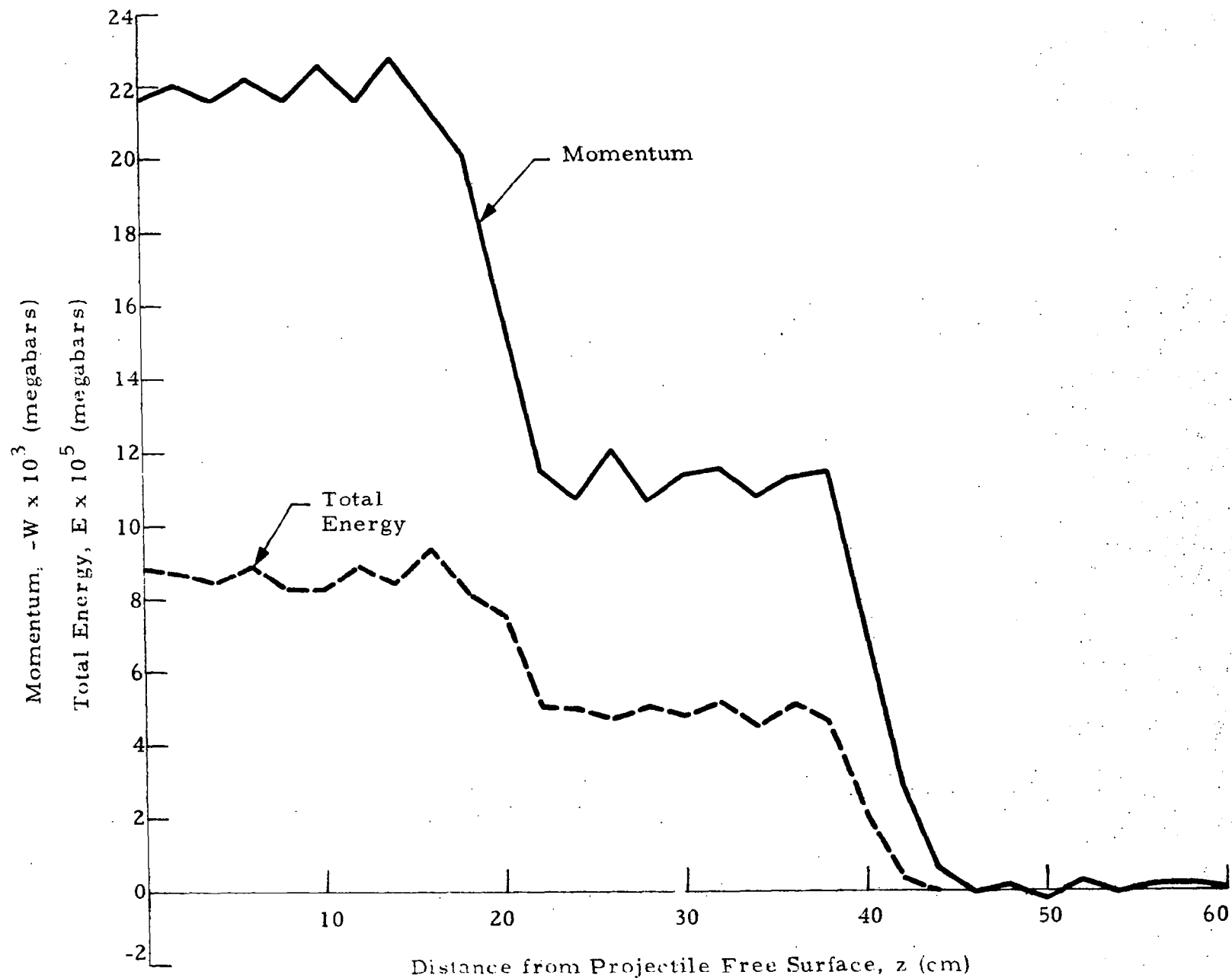


Fig. 6-35 - Momentum and Total Energy Distributions at $t = 30.0 \mu\text{sec}$
(16 Linear Elements; $a = 2.0$, $\alpha = 0.0$)

Fig. 6-35 - Momentum and Total Energy Distributions at $t = 20.0$ msec

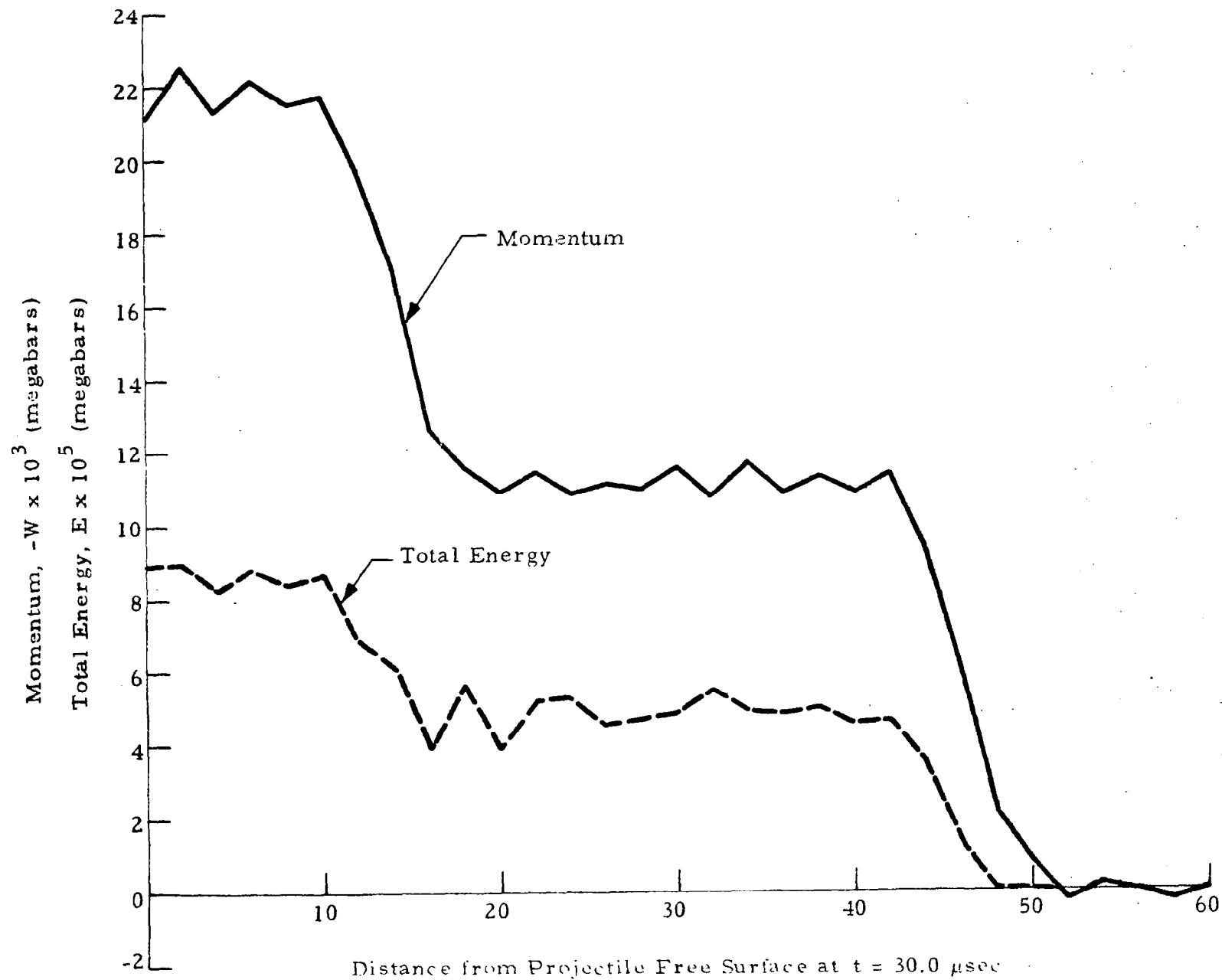
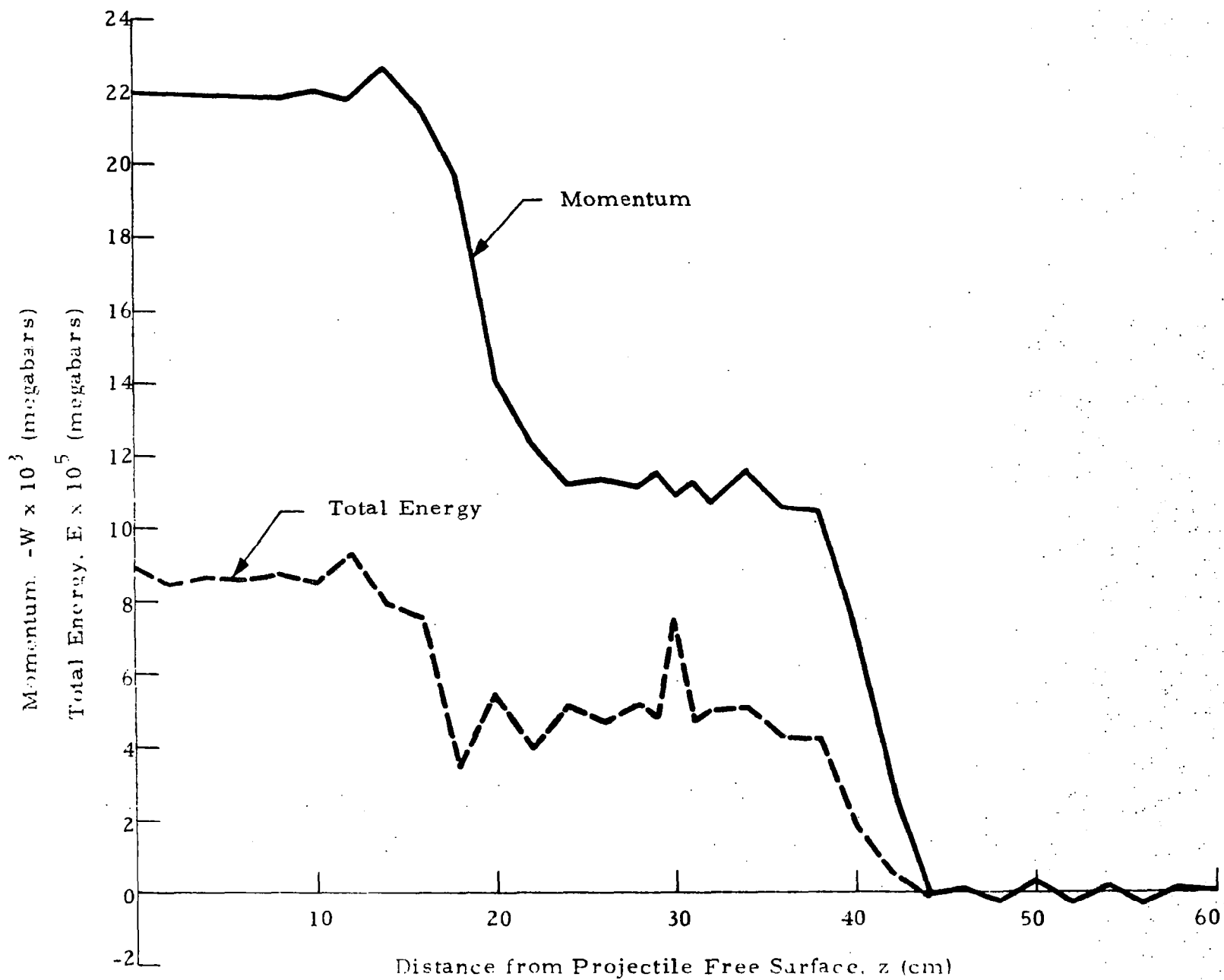


Fig. 6-37 - Momentum and Total Energy Distributions at $t = 30.0 \mu\text{sec}$
(30 Linear Elements; $a = 2.0$, $\alpha = 0.0$)

Fig. b-38 - Momentum and Total Energy Distributions at $t = 20.0 \mu\text{sec}$

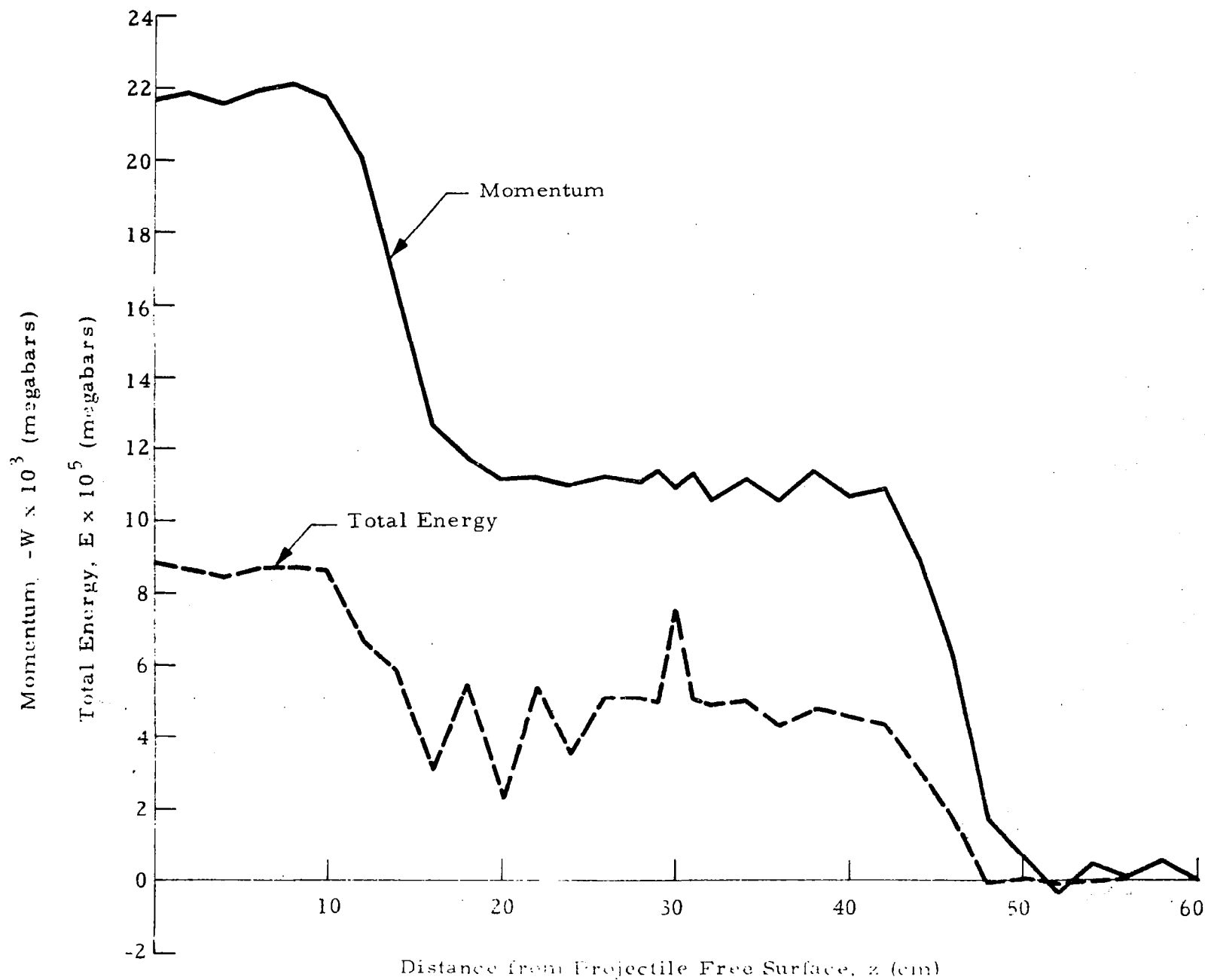
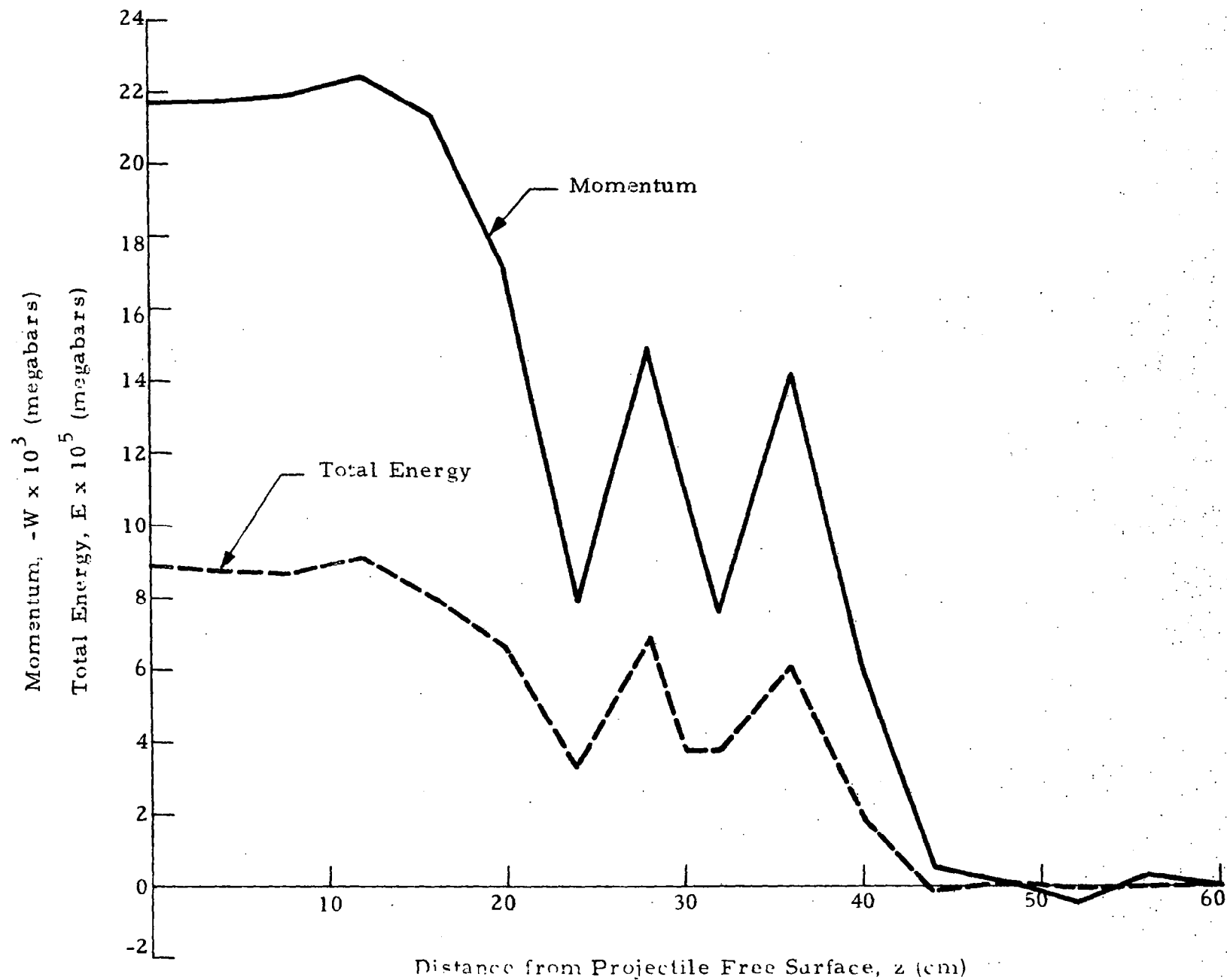


Fig. 6-39 — Momentum and Total Energy Distributions at $t = 50$ psec
(16 Quadratic Elements; $a = 2.0$, $\alpha = 0.0$)



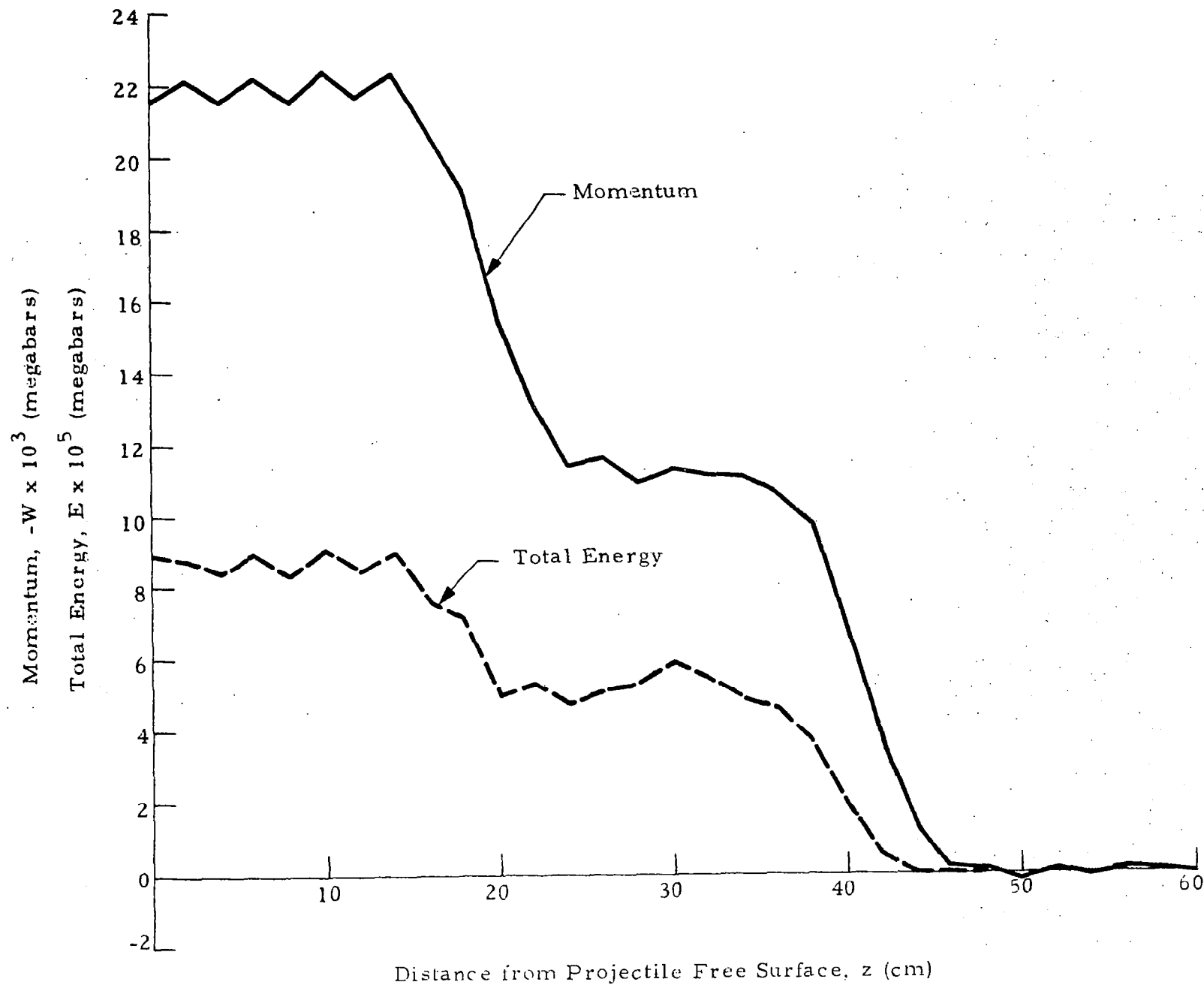
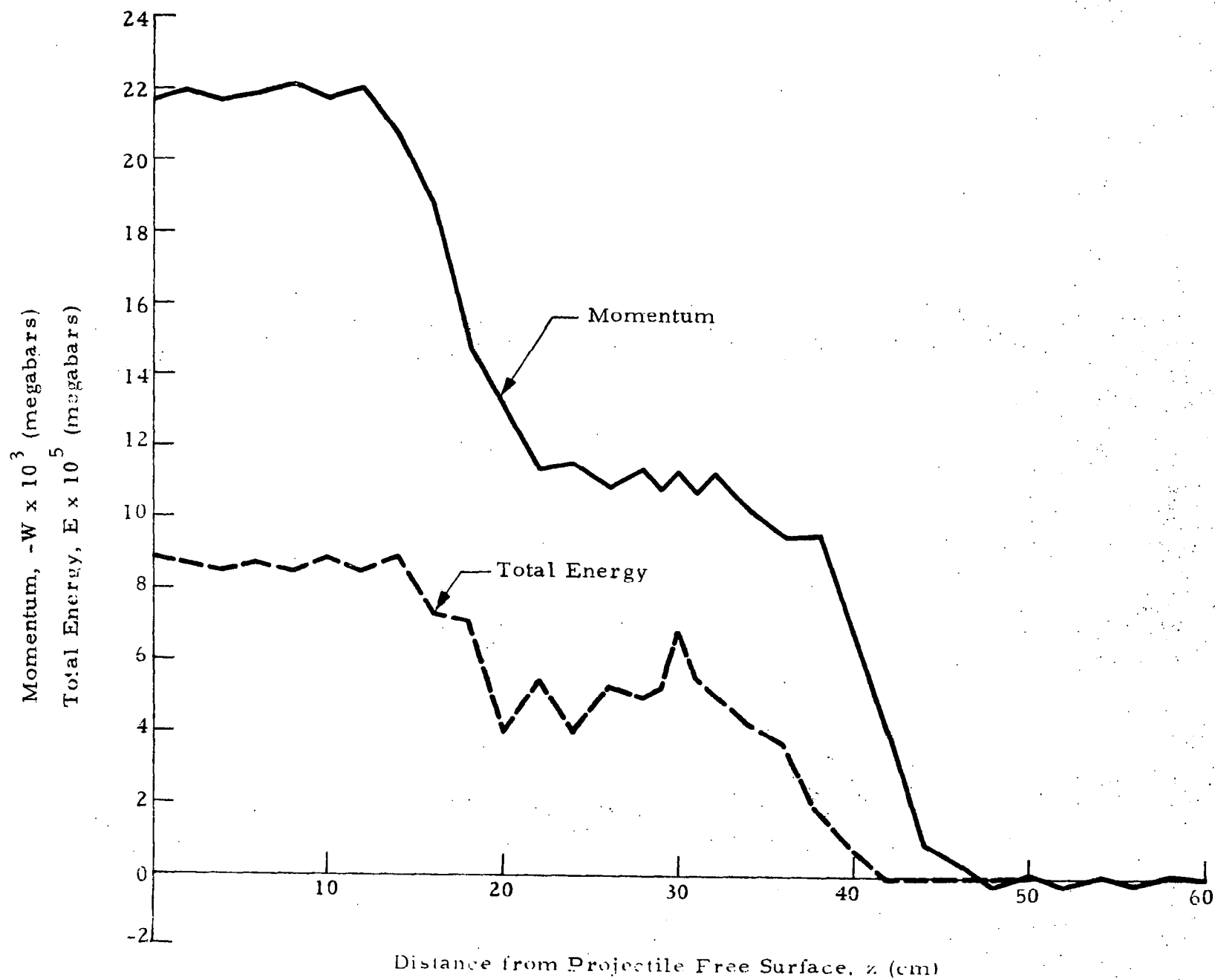


Fig. 6-41 - Momentum and Total Energy Distributions at $t = 20.0 \mu\text{sec}$
 (30 Linear Elements; $a = 4.0$, $\alpha = 0.0$)

09-9



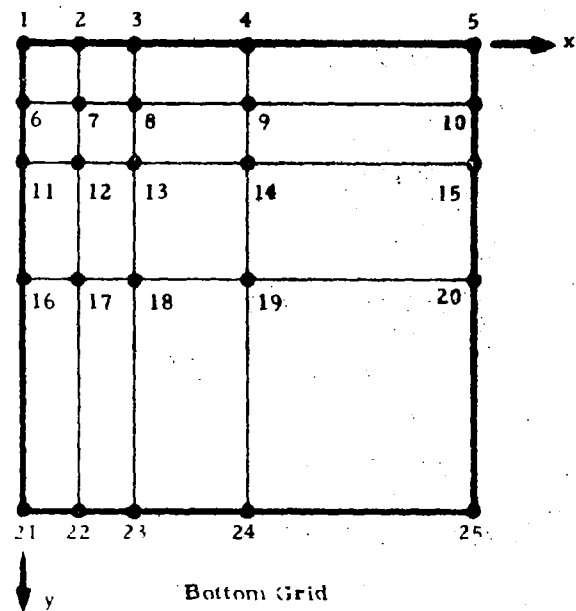
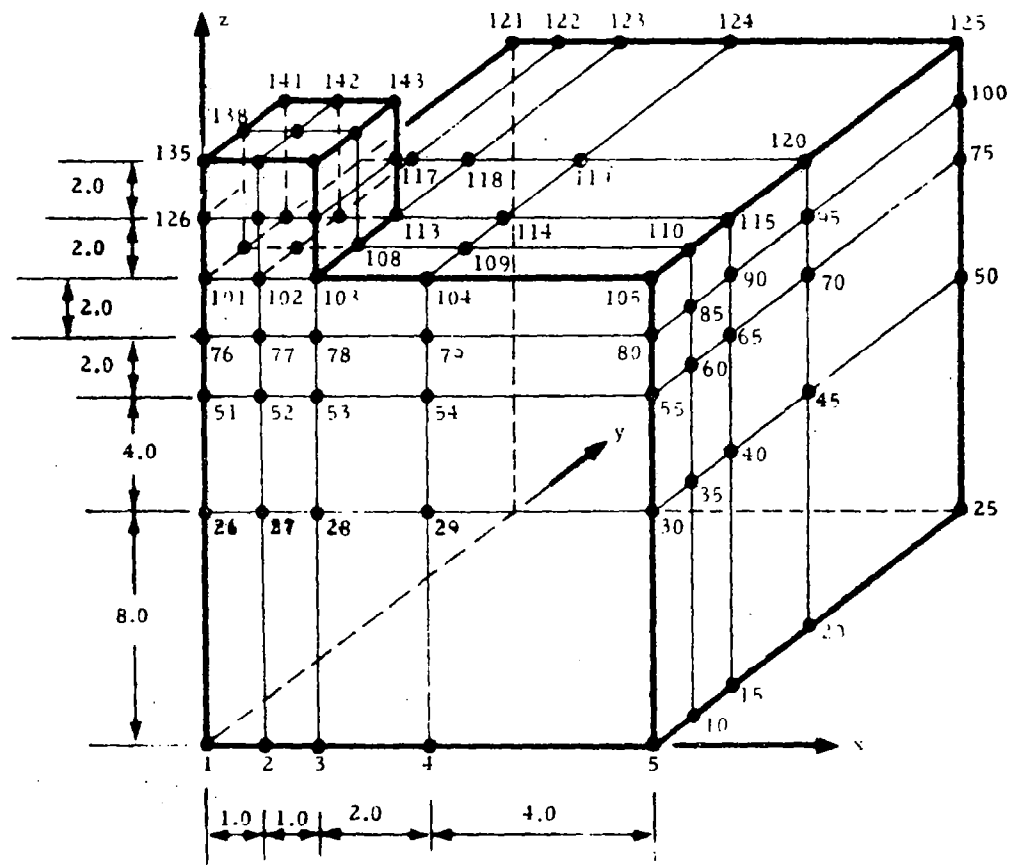
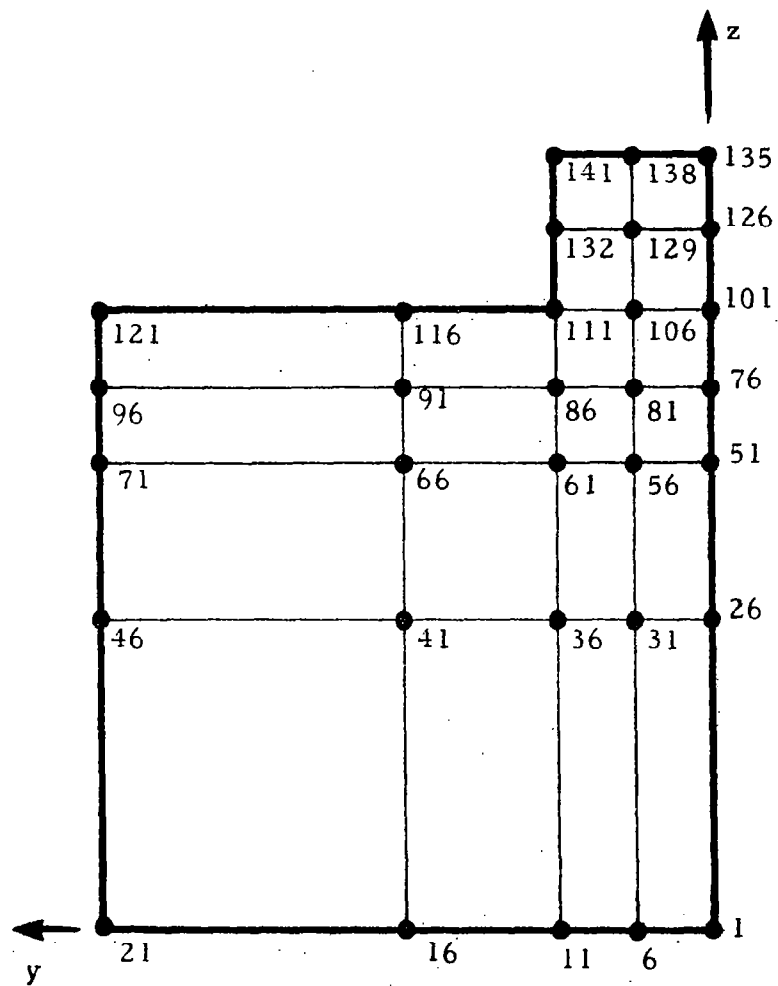
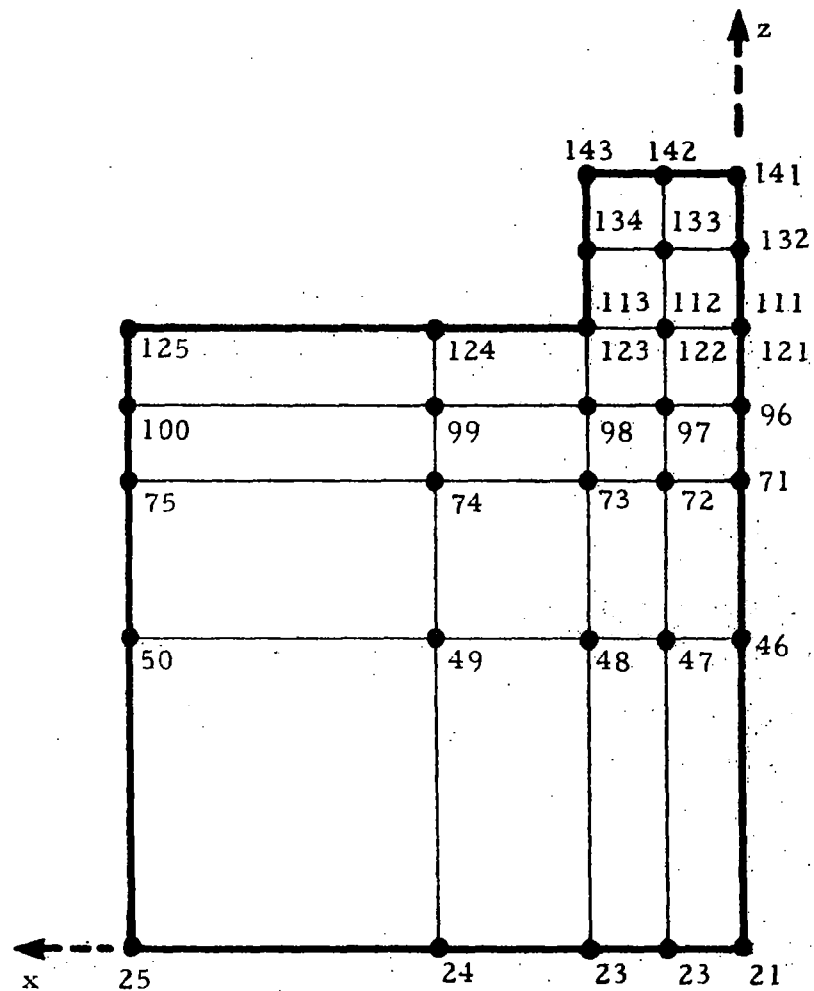


Fig. 6-43 - Numbering of Nodes in the Finite Element Mesh

79-9



Left Side



Back Side

Fig.6-43 (Continued)

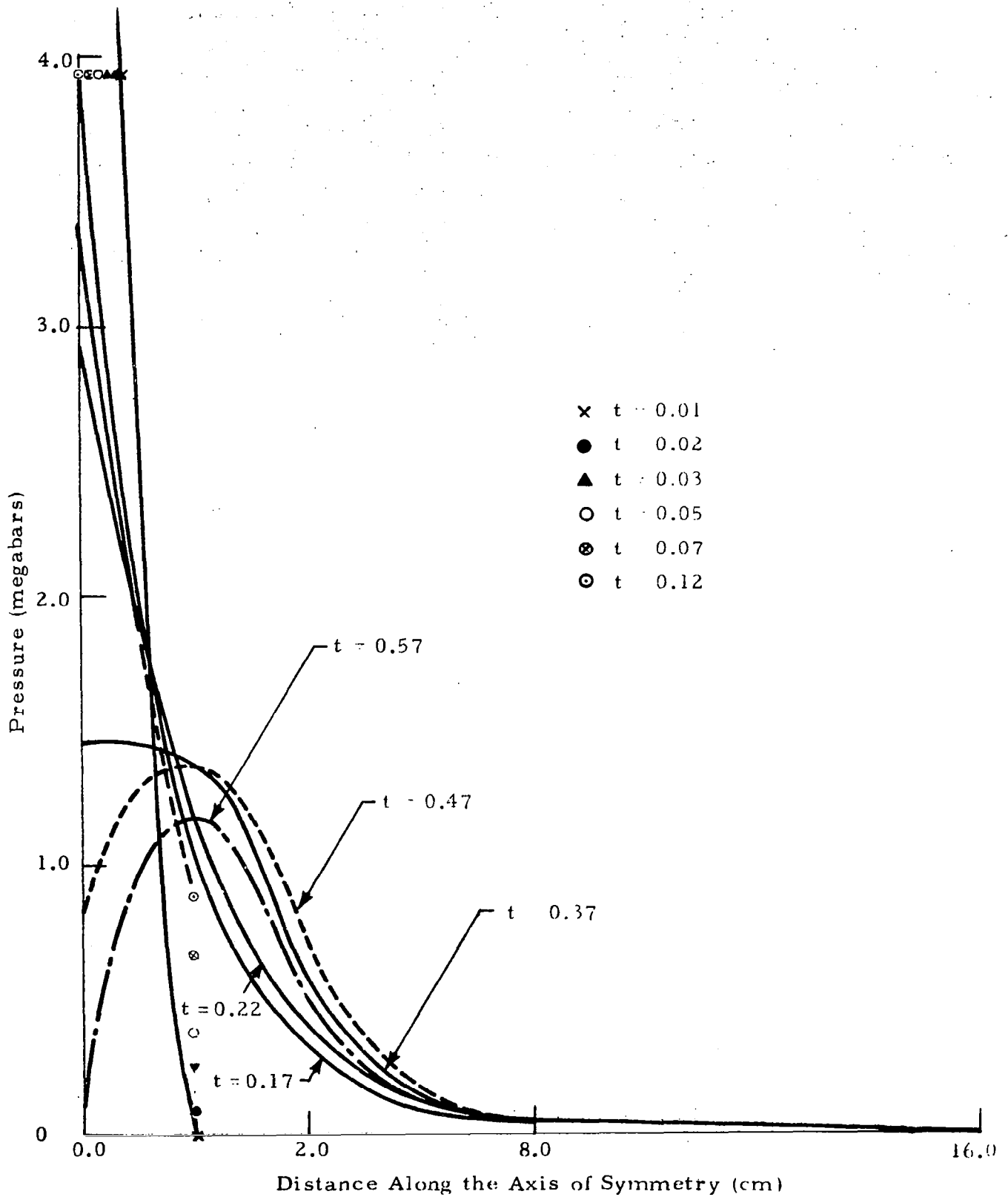


Fig. 6-44 - Pressure vs Distance into the Target ($\rho_0 = 2.702 \text{ gm/cm}^3$, $v_0 = 2.6 \text{ cm}/\mu \text{ sec}$)

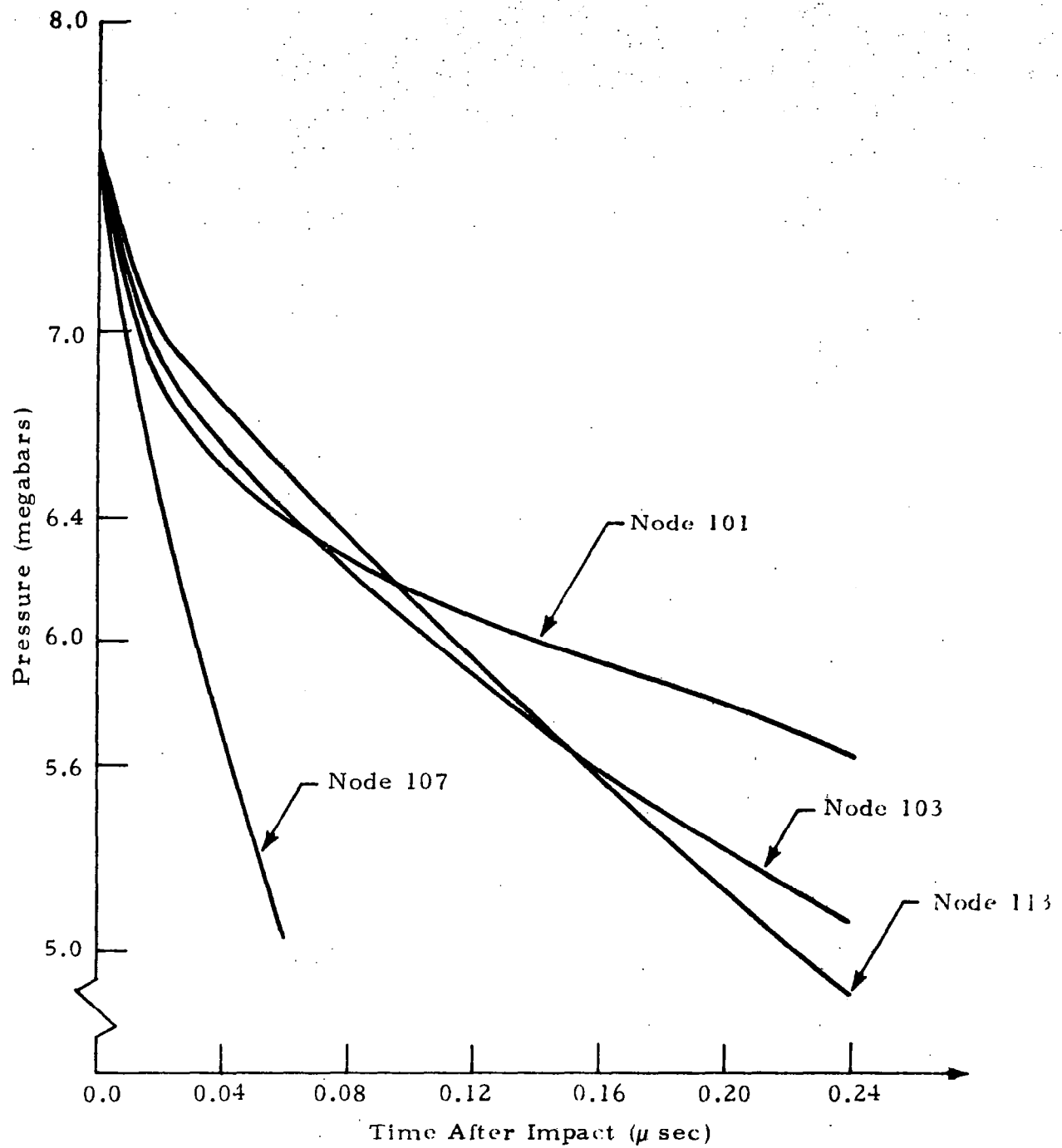


Fig. 6-45 - Pressure vs Time at Various Nodes on the Interface
 $(p_o = 2.702 \text{ gm/cm}^3, v_o = 2.6 \text{ cm}/\mu \text{ sec}, \Delta t = 0.02)$

6.3 IMPACT PROBLEM WITH HYDROELASTO-VISCOPLASTIC MODEL

The governing equations with their finite element analogues are given in Section 5. The computer code will, at the end, be capable of handling large deformations, anisotropic materials, plastic yielding and material fracture.

The one-dimensional impact problem discussed earlier is used also to test the present model. The problem description and the finite element mesh have been shown in Figs. 6-17a and 6-17b. In the computations, the material constants are assumed to be:

$$\text{Initial density, } \rho_0 = 2.77 \text{ gm/cm}^3$$

$$\text{Shear modulus, } \mu = 0.276 \text{ megabar}$$

The impact velocity, $v_0 = 0.008 \text{ cm}/\mu\text{sec}$, and Los Alamos equation of state was also used for the present problem. For the purpose of comparisons, the problem was solved by both the Galerkin method and the weak-solution formulation.

Results Computed by Galerkin's Procedures: Figures 6-46 through 6-48 show the pressure and axial stress histories at the interface, the normal stress, momentum and total energy distributions computed by the Galerkin method. When they are compared to the results computed from the inviscid hydrodynamic code, it is clear that the spurious oscillations behind the shock front are smaller. However, the pressure development at the interface seems again to grow indefinitely, though the results computed up to the time is still finite. The axial stress, on the other hand, is found to be much lower than the Hugoniot pressure, P_s . Moreover, the normal stresses on planes perpendicular to the axis are mostly positive, which imply the materials are under tensile stress in the axial direction. This obviously is not physically correct. These phenomena, therefore, indicate that the numerical results computed by Galerkin's method are totally unacceptable.

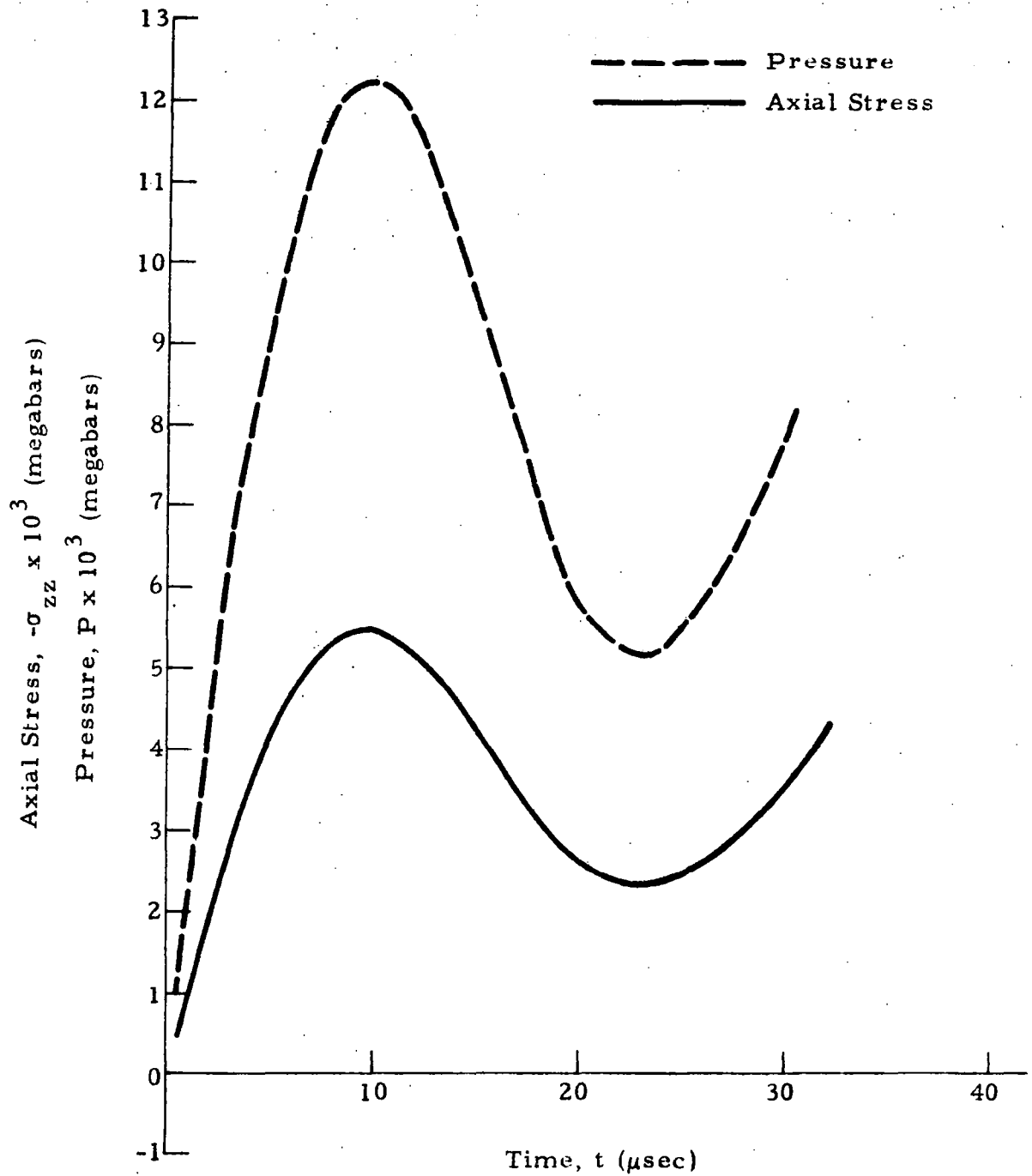


Fig. 6-46 - Axial Stress and Pressure Developments at the Interface Using Galerkin's Method (16 Linear Elements)

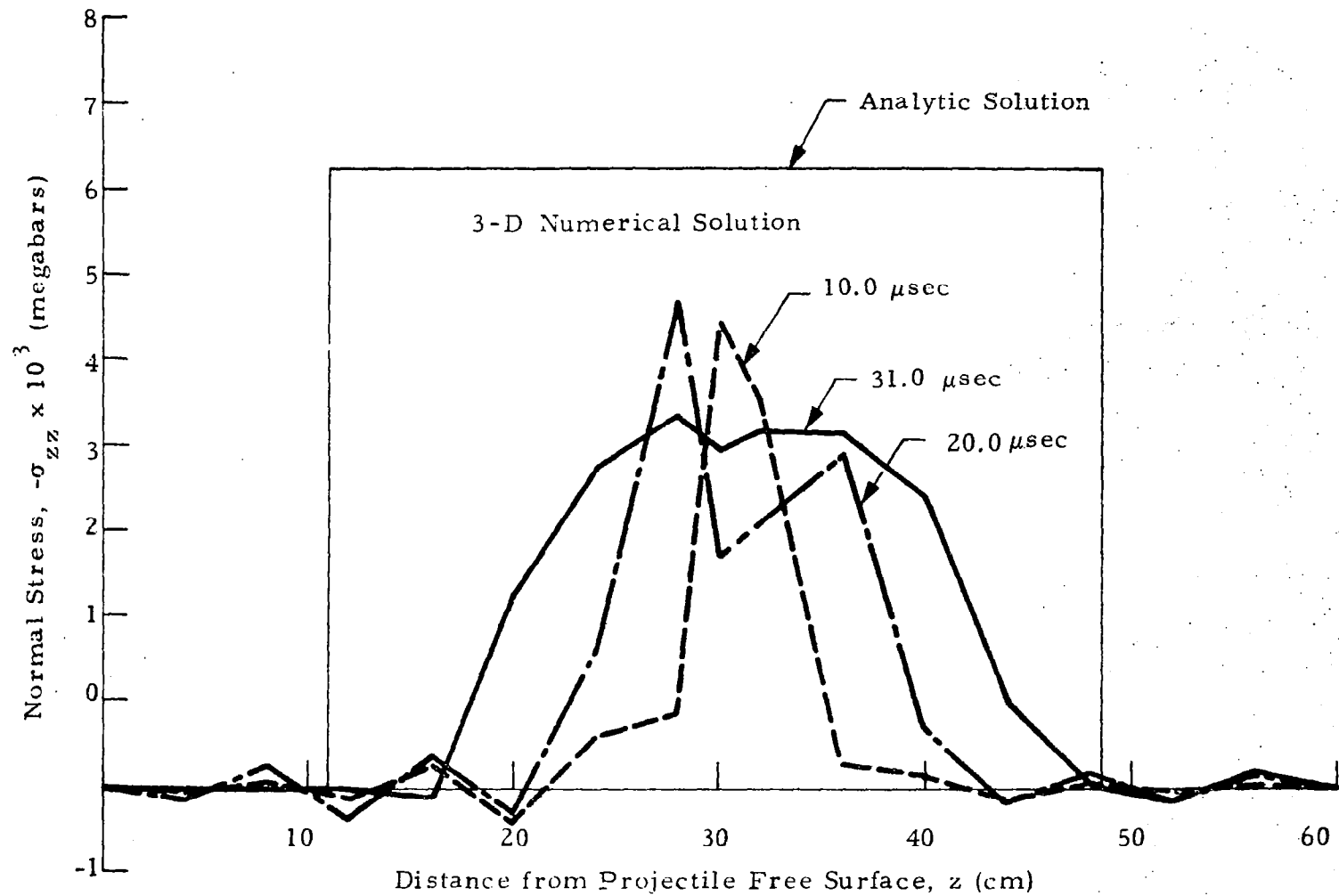
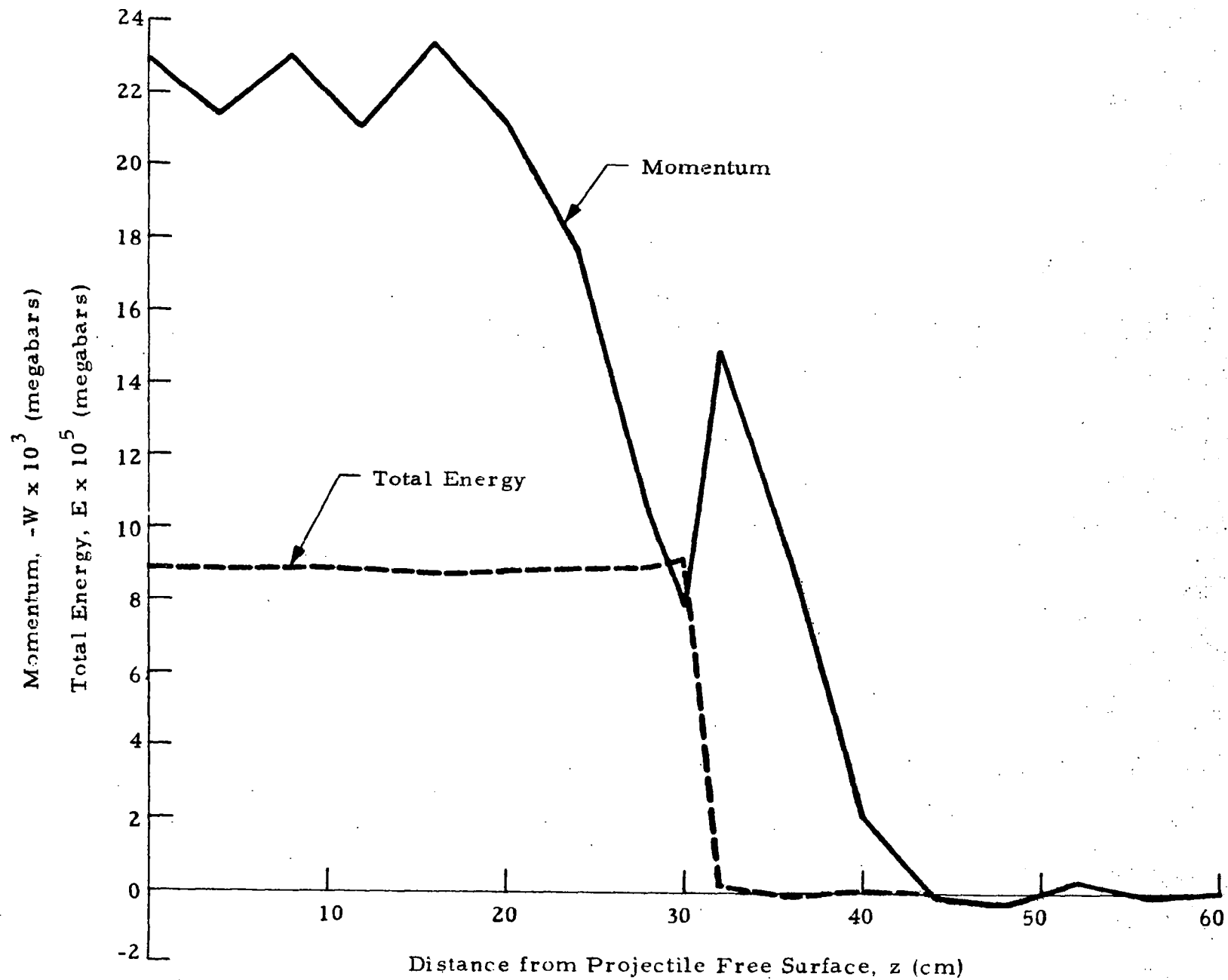


Fig. 6-47 - Normal Stress Distributions at Various Times Using Galerkin's Method (16 Linear Elements)

89-9



Results Computed by Weak Solution Formulation: The numerical solution of the problem is much improved when the technique based on weak solution formulation is used. In Fig. 6-49, the pressure as well as the axial stress history are depicted against time. The parameters used in this computation are $a = 4.0$, $\alpha = 0.0$, and the time step, $\Delta t = 0.2 \mu\text{sec}$. When these results are compared with those in the inviscid case (see Figs. 6-22 and 6-23) some deviation is observed. In the inviscid hydrodynamic model, the pressure history computed using both $a = 2.0$ and $a = 4.0$ is found to be damped out significantly as time increases. Using the present method with $a = 4.0$, however, results seem to suggest that less dissipations are present. The reason for this is not clear at the moment. Further mathematical study of this algorithm is needed to clarify the question.

The distributions of the normal stresses at $t = 10.0$, 20.0 and $34.2 \mu\text{sec}$ are depicted in Figs. 6-50 through 6-52, respectively. As indicated in the plots, the compressive axial stress σ_{zz} has an average value approximately equal to the Hugoniot pressure, P_s , after some time of the impact. This, again, suggests our numerical results are quite reasonable. For this particular example, the impact velocity is moderate, and the viscous effects may come only from the equation of state but not from the constitutive equations, i.e., the shear stresses computed from the constitutive equations are negligibly small compared to the normal stresses. This implies that, the dynamic response of the materials due to impact is in the elastic range, and the stress wave must have an average value approximately equal to P_s .

From Figs. 6-50 through 6-52, we may also find the fact that, even the parameter a used in the computations is set to be 4.0 , the spurious oscillations behind the wave front are still apparent. The lack of numerical dissipative effects in the scheme can also be detected in the interacting region of rarefaction waves as depicted in Fig. 6-53. To smooth out the zig-zag behavior, an increase of a can be employed, so long as the stability criterion of the present time marching scheme is not violated. A better way for reducing these oscillations, however, would be to refine the mesh and/or use higher order elements. Further studies on this aspect are underway and detailed discussions will be presented in the forthcoming final report.

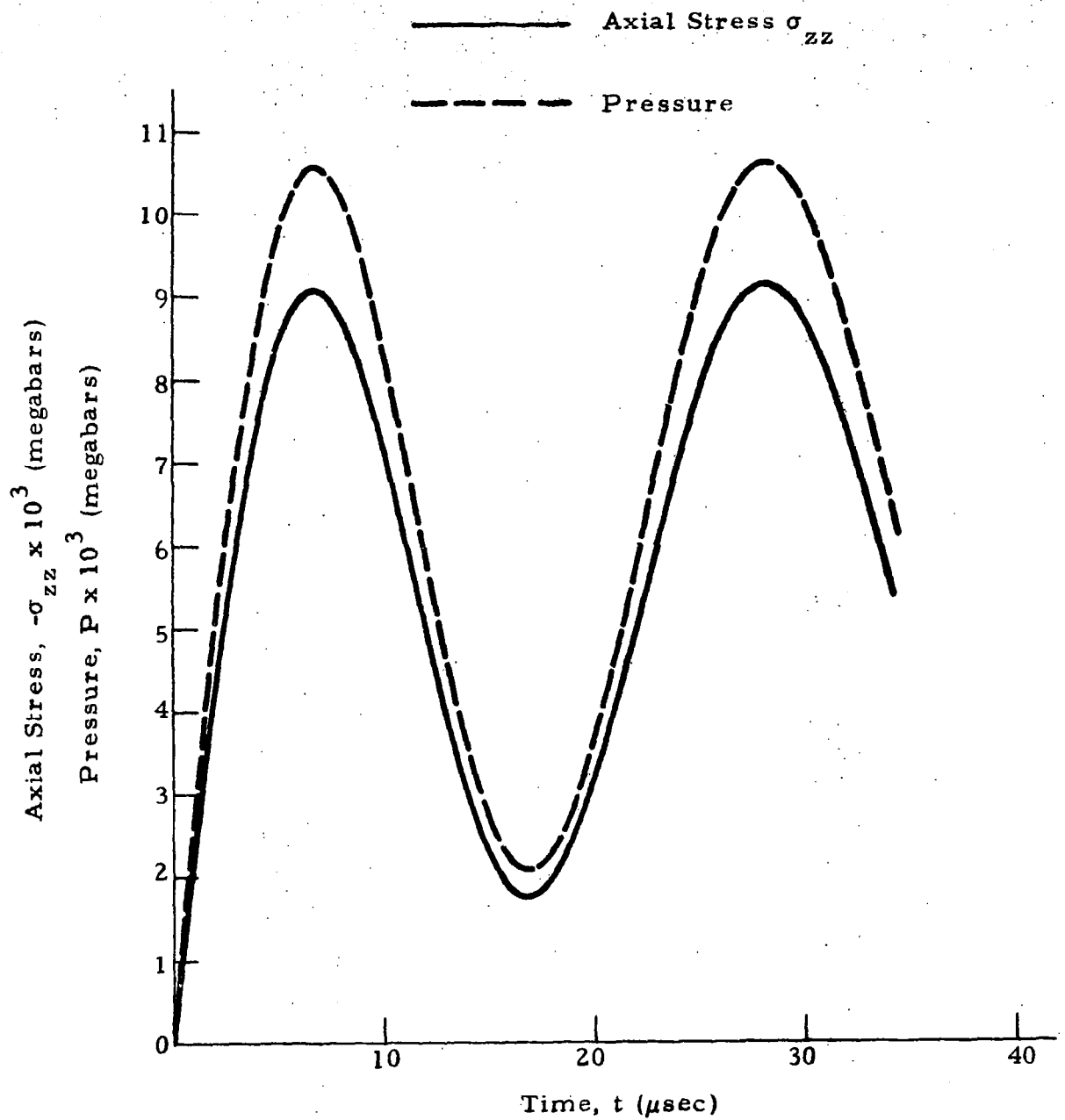


Fig. 6-49 - Axial Stress and Pressure Developments at the Interface (16 Linear Elements; $a = 4.0$, $\alpha = 0.0$)

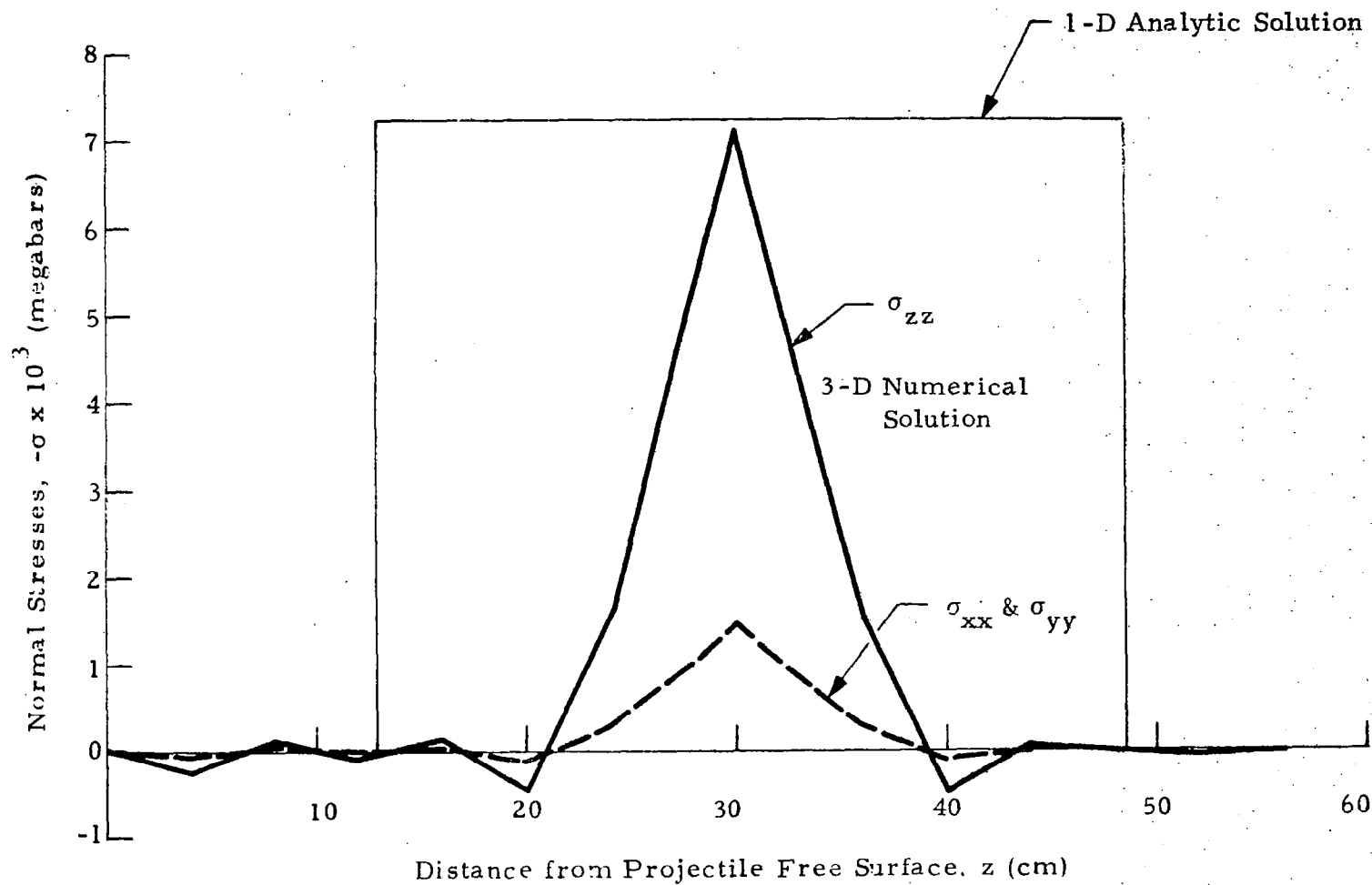


Fig 6-50 - Normal Stresses Distributions at $t = 10.0 \mu\text{sec}$ (16 Linear Elements; $\mu = 4.0$, $\alpha = 0.0$)

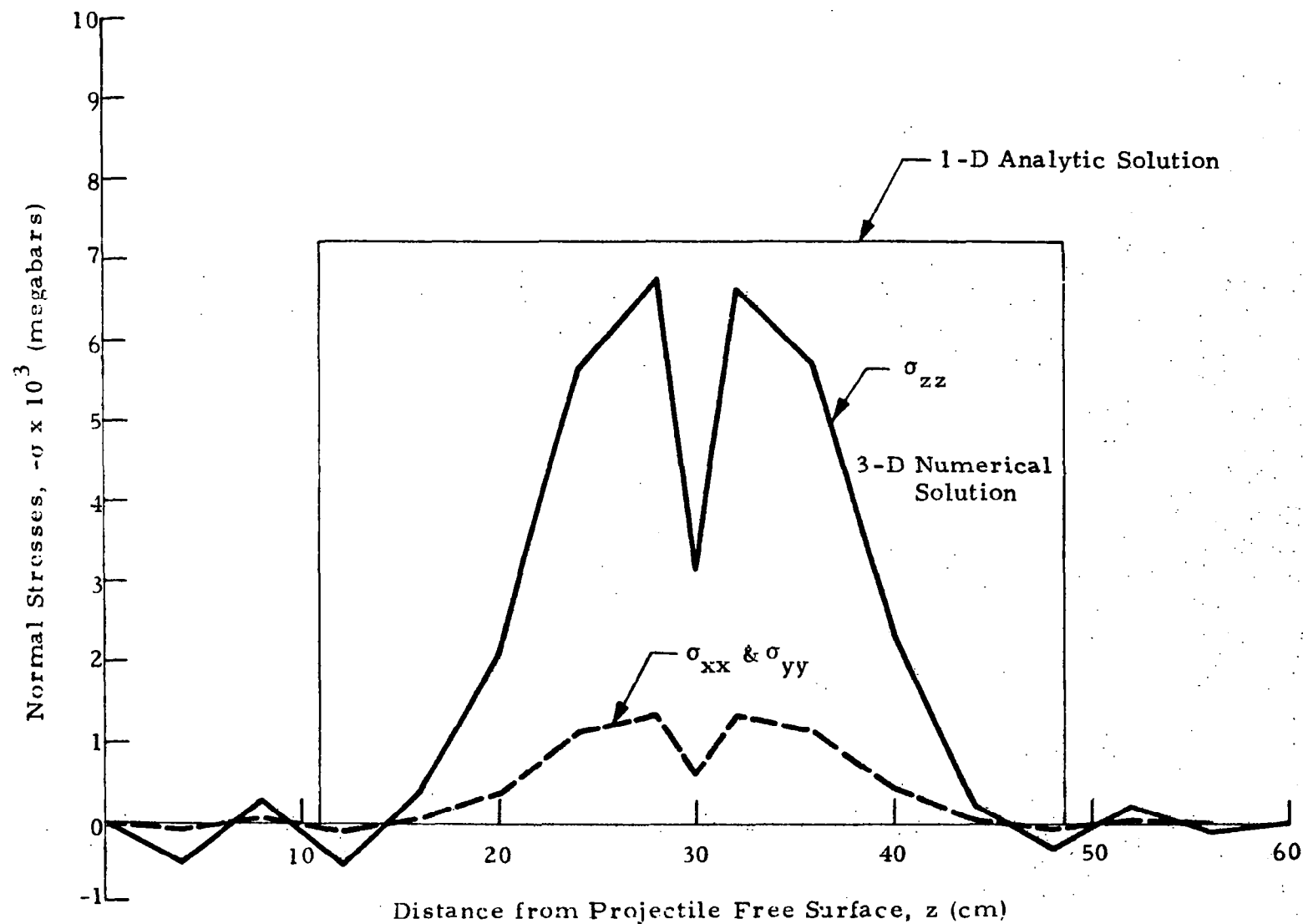


Fig. 6-51 - Normal Stresses Distributions at $t = 20.0 \mu\text{sec}$ (16 Linear Elements;
 $a = 4.0$, $\alpha = 0.0$)

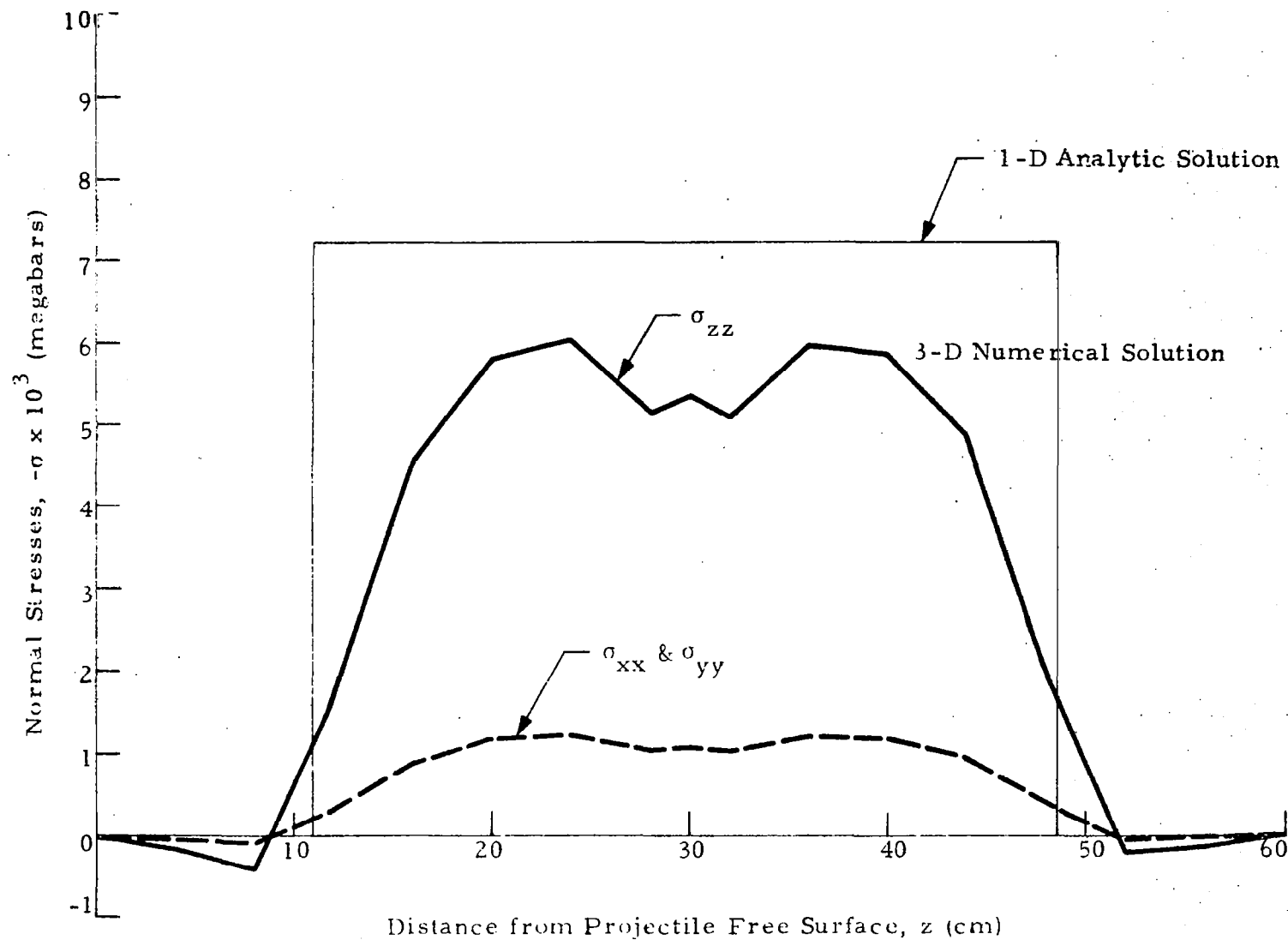
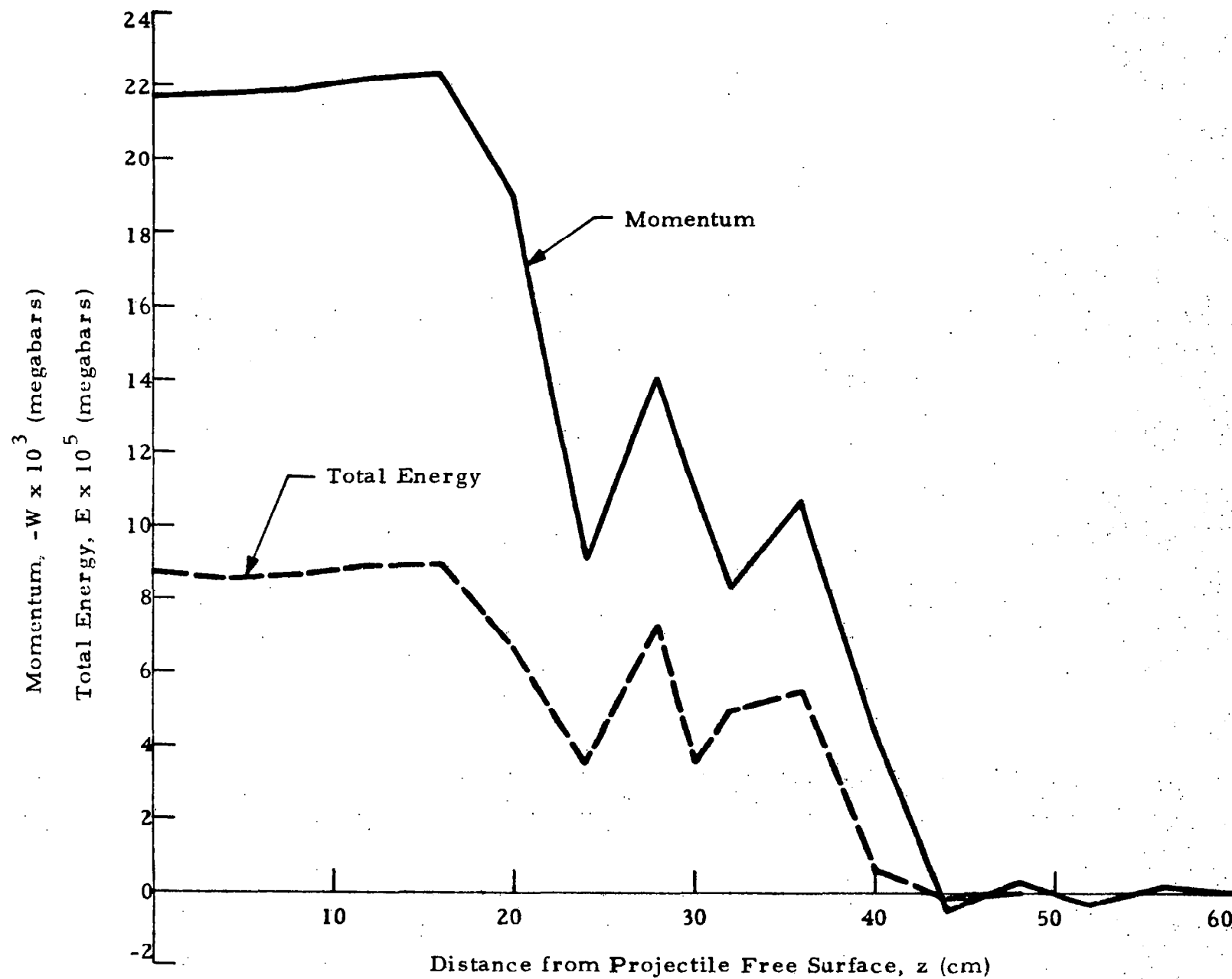


Fig. 6-52 - Normal Stresses Distributions at $t = 34.2 \mu\text{sec}$ (16 Linear Elements;
 $\alpha = 4.0, \alpha = 0.0$)

6-74



7. SUMMARY AND DISCUSSION

The objective of the current study is to develop a finite element computer program for the numerical solution of three-dimensional high velocity impact problems, based on the Eulerian hydroelasto-viscoplastic formulation. Two models, namely, the inviscid hydrodynamic model and the hydroelasto-viscoplastic model were formulated. The theoretical basis and detailed formulations for the subject problem were discussed in the preceding sections. Computer programs based on the methods of weighted residuals and the theorem of weak solution have been coded and debugged by running a number of test problems.

For general impact problems, the conventional methods of weighted residual were found to be unsatisfactory. The main reasons are:

- The formulations, such as in the methods of Galerkin and least squares, do not generally satisfy the jump conditions.
- The finite element analog of the problem always lacks of dissipative terms, and thus causes severe numerical instabilities behind the discontinuity such as shocks, as well as in the interacting region of rarefaction waves.

These difficulties can be overcome by the two-step, time-splitting finite element formulation based on the theorem of weak solutions. The success with this formulation has been demonstrated by a number of numerical experiments. As indicated by the numerical results, though the relaxation factor α is related directly upon the ratio of the time step size to the mesh size, the sensitivity of the solution upon α is rapidly reduced by refining the mesh and by using higher order elements. The value of the parameter a in Eq. (5.15) can also be reduced by similar treatments to acquire the same stability criterion.

It is believed that, an optimal choice for a would be the satisfaction of the following condition:

$$a \frac{\Delta x_k}{\Delta t} = (|v_k| + c_s) n_k, \quad k = 1, 2, 3$$

where c_s is the local sound speed, Δx_k is the mesh size along x_k -direction.

Despite the successfulness of this presently developed technique, its mathematical structure needs to be investigated further. At the present time, the suitable choices of a and α rely mainly on numerical experiments; the stability criterion for the present scheme has not been analyzed. These problems can only be resolved by a thorough mathematical analysis of the present procedure.

In view of the findings up-to-date further work will be continued as follows:

- Investigate the mathematical structure of the two-step, time-splitting, weak-solution formulation developed in this study.
- Incorporate a subroutine to properly account for the free surface movement.
- Incorporate a large system equation solver.
- Include subprograms for plastic yielding and material fracture.
- Develop a code for coupling Eulerian and Lagrangian modes.
- Prepare and run the demonstration problems.

8. REFERENCES

1. Rand Corp., Proceedings of the First Hypervelocity and Impact Effects Symposium, Santa Monica, Calif., March 1955.
2. U.S. Naval Research Laboratory, Proceedings of the Second Hypervelocity and Impact Effects Symposium, Washington, D.C., December 1957.
3. Arnold Research Foundation, Proceedings of the Third Symposium on Hypervelocity Impact, Chicago, February 1959.
4. U.S. Air Force, Proceedings of the Fourth Symposium on Hypervelocity Impact, Air Proving Ground Center, Eglin AFB, Fla., April 1960.
5. Colorado School of Mines, Proceedings of the Fifth Symposium on Hypervelocity Impact, Denver, October 1961.
6. Firestone Tire and Rubber Co., Proceedings of the Sixth Symposium on Hypervelocity Impact, Akron, April 1963.
7. Martin Company, Proceedings of the Seventh Hypervelocity Impact Symposium, Orlando, February 1965.
8. Proceedings of the AIAA Hypervelocity Impact Conference, AIAA, New York City, April 1969.
9. Kinslow, R., High-Velocity Impact Phenomena, Academic Press, New York, 1970.
10. Rosenblatt, M., "Analytical Study of Strain Rate Effects in Hypervelocity Impacts," NASA-CR-61323, 1970.
11. Hanagud, S., and B. Ross, "Large Deformation, Deep Penetration Theory for a Compressible Strain-Hardening Target Material," AIAA J., Vol. 9, pp. 905-911, 1971.
12. Chou, P.C., and A.K. Hopkins, Dynamic Response of Materials to Intense Impulsive Loading, Metals and Ceramics Division, Air Force Materials Laboratory, Wright-Patterson AFB, Ohio, 1973.

13. Fyfe, I. M., "Application of 'Hydrodynamic' Theory to the Low Stress Range of Hypervelocity Impact Problems," Proc. Fifth Symp. Hypervelocity Impact, Colorado School of Mines, 1961, pp. 299-305.
14. Olshaker, A. E., and R. L. Bjork, "Hydrodynamics Applied to Hypervelocity Impact," Proc. Fifth Symp. Hypervelocity Impact, Colorado School of Mines, 1961, pp. 185-239.
15. Walsh, J. M., and J. H. Tillotson, "Hydrodynamics of Hypervelocity Impact," Proc. Sixth Symp. Hypervelocity Impact, Firestone Tire and Rubber Co., Akron, Ohio, April 1963.
16. Ludloff, K. G., "A Hydrodynamic Model for Hypervelocity Impact," Ph.D. Thesis, University of California, Los Angeles, University Microfilms, Ann Arbor, Mich., 1967.
17. Halperson, S. M., "Comparisons Between Hydrodynamic Theory and Impact Experiments," Proc. Seventh Hypervelocity Impact Symposium, Martin Co., Orlando, Fla., February 1965.
18. Prater, R. F., "Hypervelocity Impact - Material Strength Effects on Crater Formation and Shock Propagation in Three Aluminum Alloys," AFML TR-70-295, Wright-Patterson AFB, Ohio, December 1970.
19. Riney, T. D., "Solution of Viscoplastic Equations for Axisymmetric Hypervelocity Impact," Second Summary Report, 3 November 1961 - 2 November 1962, APGC TDR-62-74, AD 294 959 (December 1962).
20. Riney, T. D., "Theoretical Hypervelocity Impact Calculations Using the PICWICK Code," Interim Report, 24 June 1963 - 23 December 1963, ATL-TDR-64-8, AD 434 220 (March 1964).
21. Kraus, H., "Two-Dimensional Analysis of Hypervelocity Impact on Viscoplastic Plate," Proc. Sixth Symp. Hypervelocity Impact, Firestone Tire and Rubber Co., Akron, Ohio, April 1963.
22. Thomson, R. G., "Hypervelocity Perforation of Viscoplastic Solid - Effects of Target Material Yield Strength," NASA-TR-R-221, 1965.
23. Aprahamian, R., and J. Piechocki, "Theoretical Analysis of One-Dimensional Impact Including Elastic/Plastic Effects," LMSC-B130200, Lockheed Missiles & Space Company, Hardening Technology Studies, Vol. V, Final Report, 1966.

24. Leimbach, K. R., and R. J. Prozan, "Study of Hypervelocity Impact on Orbital Space Stations," LMSC-HREC TR D306582, Lockheed Missiles & Space Company, Huntsville, Ala., April 1973.
25. Noh, W. F., "CEL: A Time-Dependent, Two-Space Dimensional, Coupled Eulerian-Lagrange Code," Methods in Computational Physics: Advances in Research and Applications, A. S. Fernbach, and M. Rotenberg (eds.) Vol. 3, Fundamental Methods in Hydrodynamics, pp. 117-179, Academic Press, 1964.
26. Prager, W., "An Elementary Discussion of Definitions of Stress Rate," Q. Appl. Math., Vol. 18, p. 403, 1961.
27. Tillotson, J. H., "Metallic Equations of State for Hypervelocity Impact," General Atomic Report, GA-3216, 1962.
28. Clough, R. W., "Comparison of Three-Dimensional Finite Elements," Symposium of Applied Finite Element Methods in Civil Engineering, Vanderbilt University, Nashville, Tenn., November 1969.
29. Zienkiewicz, O. C., The Finite Element Method in Engineering Science, McGraw-Hill, New York, 1971, p. 121.
30. Conte, S. D., Elementary Numerical Analysis, McGraw-Hill, New York, 1965, pp. 138-143.
31. Richtmyer, R. D., and K. W. Morton, Difference Methods for Initial Value Problems, 2nd ed., Interscience, New York, 1967.
32. Wilson, E. L., and R. E. Nickell, "Application of Finite Element Method to Heat Conduction Analysis," Nuclear Eng. and Design, Vol. 4, 1966, pp. 1-11.
33. Lax, P., "Weak Solutions of Nonlinear Hyperbolic Equations and Their Numerical Computation," Comm. Pure and Appl. Math., Vol. 7, 1954, pp. 159-193.
34. Oleinik, O. A., "Discontinuous Solutions of Nonlinear Differential Equations," Uspekhi Mat. Nauk, Vol. 12, 1957, pp. 3-73.
35. France, P. W., "An Improved Finite Element Technique for the Analysis of Free Surface Flow Problems," International J. of Computers and Fluids, Vol. 3, 1975, pp. 149-153.
36. Wilson, E. L., K. J. Bathe and W. P. Doherty, "Direct Solution of Large System of Linear Equations," Computers & Structures, Vol. 4, 1974, pp. 363-372.
37. Vendhan, C. P., M. P. Kapoor and Y. C. Das, "An Integrated Sequential Solver for Large Matrix Equations," Int. J. Num. Methods in Eng., Vol. 8, 1974, pp. 227-248.

38. Irons, B.M., "A Frontal Solution Program for Finite Element Analysis," Int. J. Num. Methods in Eng., Vol. 2, 1970, pp. 5-32.
39. Carslaw, H.S., and J.C. Jaeger, Conduction of Heat in Solids, 2nd Edition, Oxford University Press, 1959.
40. Rosenblatt, M., "Analytical Study of Strain Rate Effects in Hypervelocity Impact," NASA CR-61323, January 1970.